Manipulation of Vanadium Oxide Characteristics for Applications:

Resistive switching & Reflectance Anisotropy Spectroscopy

THE UNIVERSITY OF DUBLIN
TRINITY COLLEGE

Oisín Murtagh

School of Physics

Trinity College Dublin

A thesis submitted for the degree of
Doctor of Philosophy
July 13, 2022

Declaration

I have read and I understand the plagiarism provisions in the General Regulations of the University Calendar for the current year, found at http://www.tcd.ie/calendar.

I have also completed the Online Tutorial on avoiding plagiarism 'Ready Steady Write', located at http://tcd-ie.libguides.com/plagiarism/ready-steady-write

Oisín Murtagh ________________________________

July 13, 2022

Summary

This thesis deals with the study of vanadium dioxide, vanadium pentoxide and the mixed 4+ and 5+ valence vanadium oxide phases, or Wadsley phases. Thin films (VO_2) and single crystals (V_2O_5) are examined. Vanadium dioxide is of particular interest to novel future electronic applications due to a large and accessible metal-insulator transition (MIT). The aim of this work is to enable the use of vanadium oxides through the physical understanding of their properties, and leveraging this understanding to manipulate the material's properties to enable novel and useful applications. Specifically, manipulation of VO_2 resistive switching is explored via (i) the application of pulsed voltage signals and (ii) through the forming of VO_2 from the reduction of V_2O_5 single crystals.

In this thesis, three main studies are carried out. First, vanadium dioxide thin film devices are fabricated that exhibit a voltage-driven metal insulator transition. It is found that the intrinsic hysteresis of this transition is due to Joule heating in the low resistance phase, and that the hysteresis width can be changed by applying pulsed voltage signals of different lengths. Computer simulation via Python is leveraged to confirm the Joule heating effect through modelling of the sample temperature.

In the second study, it is found that V_2O_5 crystals, when annealed in vacuum, form a surface layer composed of Wadsley phases and VO_2. This layer exhibits a VO_2-like MIT which undergoes an electric-field-driven MIT at a very low field of $425\,\mathrm{V\,m^{-1}}$. This is found to be due to Joule heating in the surface layer, which shows a low resistance. Analysis of crystals annealed at four different temperatures at different time intervals is presented to illustrate how V_2O_5 evolves over continuous vacuum annealing. Vanadium oxide phases V_6O_{13}, V_4O_9 and VO_2(B) are all identified to be present in this evolution. Transmission electron microscopy is used to identify the geometry of the phases present in the surface layer after annealing.

In the third study, the optical anisotropy of pristine and annealed V_2O_5 crystals is studied using reflectance anisotropy spectroscopy (RAS). The RAS spectrum of the V_2O_5(010) surface is presented, along with RAS features of V_6O_{13} and V_4O_9. This is achieved through analysis of four samples annealed at different temperatures. Comparisons of x-ray diffraction, resistance and RAS measurements allows particular

features to be identified and matched to particular phases. The effect of the VO_2 MIT on RAS measurements is characterised. Computational modelling via Python is used to simulate and confirm V_2O_5 and V_6O_{13} RAS measurements.

Acknowledgments

I would like to thank my supervisor, Professor Igor Shvets, for the opportunity to pursue a PhD and for his supervision and guidance over the past 4 years.

I would like to thank the Naughton Fellowship PhD program for funding this PhD and enabling us to pursue this project.

I would like to thank the APRG group, a great group of researchers that have been helpful and made my life much easier in general. I've very much enjoyed being part of the team. I'd particularly like to thank the trio of post-docs I had for the majority of my project: Dr. Daragh Mullarkey, Dr. Brian Walls and Dr. David Caffrey; for always being impressively patient with all my enquiries directed towards them and for training me on the equipment our group has.

I'd like to thank Dr. Brian Walls for assisting with all the experiments I've performed in the last 2 years. All the results in this thesis had Brian's involvement in most aspects. Thank you to Dr. Ainur Zhussupbekova for conducting and fitting XPS measurements. Thank you to Dr. Daragh Mullarkey for performing reciprocal space map measurements. Thank you to Conor Phelan for helping with the V_2O_5 annealing studies. Thank you to Dr. Dmitry Shulyatev of who provided us with V_2O_5 single crystals. Thank you to Chris Smith who performed ellipsometry measurements. Thank you to Dr. Andre Mazilkin for peforming TEM measurements and analysis. Thank you to Dr. Mullarkey, Dr. Walls and Dr. Caffrey for proof-reading parts of this thesis.

I would like to thank Prof. Wolfgang Porod and Prof. Suman Datta for hosting me and assisting me with my work in the University of Notre Dame when I visited in November and December of 2019.

I'd like to thank visiting researchers Dr. Sergey Bozhoko and Dr. Andrey Ionov for the experience and knowledge I've gained from their visits.

I'd like to thank the researchers in CRANN and the School of Physics for all their help over the years, particularly in terms of training or facilitating the use of equipment. I would like to thank the School of Physics and all its staff for all the assistance they've provided me over the years, directly and indirectly, and for all their hard work keeping the place running. I would like to thank Trinity College Dublin for hosting me for this PhD as well as for my undergraduate studies.

I'd like to thank everyone really who has been involved in my scientific studies over the years. It's hard to express how much I've relied on the input of everyone else and how grateful I am.

In terms of personal matters, I have to mention Dan Casey particularly in TCD for suffering through it all with me. I also want to thank my Dublin communities in music and cycling as well as all my other peers. Shout out to 2 Camden Buildings, where I've lived for too long, and thanks to all my poor housemates over the years. Thanks to everyone in South Bend Indiana who made me feel very welcome in my short time over there.

Finally, and most importantly, a huge thanks to my whole family: All the aunts and uncles and cousins; my grandparents: James Murtagh, Richard Noel Boyhan, Margaret Joyce and Mary Boyhan; Sinéad, my sister; and my parents, Philip Murtagh and Gráinne Boyhan.

List of publications

1. ***Controlling the resistive switching hysteresis in VO_2 thin films via application of pulsed voltage***
   Oisín Murtagh, Brian Walls and Igor V. Shvets
   Applied Physics Letters **117(6)**, 063501 (2020)

List of abbreviations

CRANN - the Centre for Research on Adaptive Nanostructures and Nanodevices
CVD - Chemical Vapour Deposition
DFT - Density Functional Theory
DP - Diffraction Pattern
E-MIT - Electronically triggered Metal Insulator Transition
FEI - Field Electron and Ion Company
FFT - Fourier Transform
FIB - Focused Ion Beam
GUI - General User Interface
ICP - Inductively Coupled Plasma
IR - Infrared
LN2 - Liquid Nitrogen
MBE - Molecular Beam Epitaxy
MIT - Metal-Insulator Transition
PEM - Photo Elastic Modulator
PID - Proportional–Integral–Derivative
PLD - Pulsed Laser Deposition
PVD - Physical Vapour Deposition
RA - Reflectance Anisotropy
RAS - Reflectance Anisotropy Spectroscopy
RIE - Reactive Ion Etch
RS - Resistive Switching
RSM - Reciprocal Space Map
RT - Resistance v Temperature
TCD - Trinity College Dublin
TEM - Transmission Electron Microscopy
UHV - Ultra-High Vacuum
UV - Ultraviolet
VASE - Variable Angle Spectroscopic Ellipsometry
VO - Vanadium Oxide
XPS - X-ray Photoelectron Spectroscopy
XRD - X-Ray Diffraction
XRR - X-Ray Reflectometry

Contents

List of Figures

List of Tables

1

Introduction

The vanadium oxide (VO) system is the focus of this work. Vanadium can exist in 4 oxidation states, from V(II) to V(V). In terms of solid compounds, vanadium oxides exist with single oxidation states (*e.g.* VO_2, V_2O_5) but also mixed (*e.g.* V_6O_{13} containing mixed V(V) and V(IV)). The VO system exhibits large internal electron repulsion [1], so the convention in much of solid state physics to ignore Coulomb repulsion cannot be applied much of the time. The structural result of this repulsion is a complex crystal system, where the relaxed structures are often asymmetric and anisotropic. Another result of this "correlated-electron" material manifests in the electronic transport properties as a metal-insulator transition (MIT). At 0 K vanadium oxides are insulating. However, many vanadium oxides will undergo a first order phase transition to a metal when heated above a certain transition temperature [2]. At this temperature, it becomes energetically favorable for valence electrons to become free carriers and conduct. The jump in conductivity is measured in orders of magnitude. As an example, VO_2 single crystals see a conductivity increase of 5 orders [3]. The conductivity transitions are accompanied by structural transitions. The transitions can be triggered and altered by inducing structural or electronic changes to the materials [4–6]. It should be noted that this MIT property is not unique to vanadium oxides, and is seen in other transition metal oxides such as Ti_2O_3, Fe_3O_4 and NbO_2 as well as other condensed-matter systems [7, 8].

Naturally, this unusual MIT property attracts interest in the form of technological applications [1, 9–11]. At its simplest, this transition enables a simple switch. Exploiting it further, oscillators and non-linear circuits can be made. These devices have opportunities in enabling non-conventional computing technologies [12, 13]. Other areas include dynamic window coatings [14, 15].

VO_2 is the most popular VO in terms of research currently. This is due to (i) its relative ease of growth (ii) its accessible MIT temperature. VO_2 transitions at 70 °C [16], a temperature achieved cheaply in any home or laboratory. It also has a sizeable MIT, a change in resistivity of 5 orders for single crystals, generally 3 orders for thin films [17]. VO_2 has been studied in depth as a result, with most experimental VO MIT applications focusing on it currently [1, 9–11]. Due to its importance, this work will look to examine certain properties of this material with the aim of tailoring specific material characteristics (and understanding the physics behind these changes) to facilitate the development of MIT technology.

V_2O_5 is an example of a VO that does not have a MIT. However, it is already used in industry as a catalyst [18] so further characterisation of this material is relevant. V_2O_5 is very easy to fabricate, and can be reduced to more electronically functional phases like VO_2 in vacuum [19, 20]. Between V_2O_5 and VO_2 are the mixed V(V) and V(IV) phases, or Wadsley phases. Of these, only V_6O_{13} exhibits an MIT. These compounds have not been the subject of a large amount of research as many are difficult to isolate. These phases are commonly seen in the reduction processes of V_2O_5 [19, 20]. This work will also aim to study the reduction of V_2O_5 and characterise less studied Wadsley phases.

The structure of this thesis is as follows:

The experimental techniques and methodologies are discussed in Chapter 2. In Chapter 3 a literature review of the vanadium oxide system is presented.

Chapter 4 focuses on the resistive switching (RS), or the electronically triggered MIT, of a VO_2 device. Through the application of pulsed voltage signals, the intrinsic hysteresis of the MIT can be manipulated. A Joule heating theory is used to describe the material behaviour, and simulations of the theory agree with experimental results. This chapter therefore establishes that many characteristic values of a VO_2 device are governed by Joule heating effects.

In Chapter 5 the reduction of a V_2O_5 crystal is examined in respect to its evolving electronic properties. It is found that the reduction results in a large number of VO phases developing in a surface layer. A study of reductions at four different temperatures is presented. Under certain conditions, this layer exhibits a VO_2-type MIT with very low resistance, and the lowest recorded electronic field required to trigger RS behaviour, at $400\,\mathrm{V\,m^{-1}}$. It is found that this is due to increased Joule heating in the surface layer.

In Chapter 6 reflectance anisotropy spectroscopy (RAS) is studied as an *in-situ* method to characterise the VO system. A full reflectance anisotropy (RA) spectrum for $V_2O_5(010)$ is measured and confirmed via ellipsometry measurements. Through comparison of samples under different reduction conditions, RAS contributions for $V_6O_{13}(001)$ and $V_4O_9(001)$ are found. Finally, the effect of the VO_2 MIT on the RAS signal is measured.

Finally Chapter 7 discusses the conclusions and implications of this work and outlines potential studies for further research.

2

Experimental Methods, Equipment & Models

In this section I outline, discuss and explain the various experimental techniques and methods used during the course of my PhD for the content within this thesis. Being an experimental thesis, I'll also include details of the equipment used in this section. Details of how techniques were applied to each experiment will be included in the relevant chapters.

2.1 Growth Techniques

Due to it's popularity VO_2 has been grown via a large variety of PVD and CVD methods. Nag *et al.* provide a comprehensive, if not a little dated, review of many of the growth techniques used to fabricate VO_2 thin films [17]. More recent reviews of growth techniques are also available [21].

For this work, two main types of samples were used: thin film VO_2 and single crystal V_2O_5. Single crystal V_2O_5 was grown at the Materials Modeling and Development Laboratory (NUST MISIS, Leninskiy prosp, 4, 199049 Moscow, Russia) via float zone growth; details of this technique can be found elsewhere [22]. Thin film VO_2 was grown using a wide variety of methods including: molecular beam epitaxy (MBE), spray pyrolysis, magnetron sputtering and pulsed laser deposition (PLD). All thin film growth was performed in TCD. All techniques provided thin films of a high enough quality to see VO_2's signature metal-insulator transition; however the PLD grown films gave the largest and most consistent current induced transition as well as favourable morphology for photolithograpy, and were therefore used in the experiments presented.

2.1.1 Pulsed Laser Deposition of VO_2

PLD is a method of thin film deposition whereby a high energy laser pulse is used to ablate a target material. A plasma plume is generated on the targets surface, and the resulting ejected material is deposited on a substrate. It was first applied by Smith And Turner in 1965 using a Q-switched ruby laser [23]. PLD is a popular method of deposition due to its flexibility in terms of targets and growth conditions while maintaining a high level of precision in growth control. Conductivity of the target is not relevant as it would be in sputtering techniques, and the power density of each laser pulse is high enough to ablate most target material, including oxides and materials unsuitable for electron beam or thermal evaporation [24]. The substrate temperature is easy to control, as well as the composition of the atmosphere within the deposition chamber. Overall, this allows for fine control over growth mode and morphology of thin films, with high quality and reproducibility. However, no technique is without its flaws, and PLD is limited by the complexity of the laser-matter interaction with its resulting plasma plume, and the difficulty in scaling the technique up for large area deposition.

Targets used were pure vanadium; formed by compressing vanadium powder into a 19 mm pellet under a static pressure of 150 bar for 10 minutes. The system used to prepare our samples uses a pulsed KrF laser (248 nm wavelength, 25 ns pulse length), focused into a vacuum chamber and onto the target, with the substrate mounted above the target. Distance from target to substrate is 7cm. The chamber is pumped by a turbo pump with backing pump, and reaches a base pressure of approximately 10^{-5} mbar. The substrate is mounted on a ceramic stage with internal thermocouple and is heated using an electric element positioned behind the stage. Oxygen can be leaked into the chamber via a leak valve to achieve a desired pressure. Laser power and pulse rate can be adjusted electronically.

2.2 X-ray Diffraction

X-rays typically have a wavelength in the order of Ångstroms, which is comparable to inter-atomic distances in most materials. If the materials has a regular periodic crystal structure, the crystal will act as a three dimensional diffraction grating to the incoming x-rays. This can be used to great advantage to probe inter-atomic distances within the crystal [26]. Bragg's Law can give us the angles for coherent elastic scattering of waves from the crystal lattice:

$$n\lambda = 2d \sin\theta \tag{2.1}$$

The formulation of this law can be seen in figure 2.1, where coherent interference

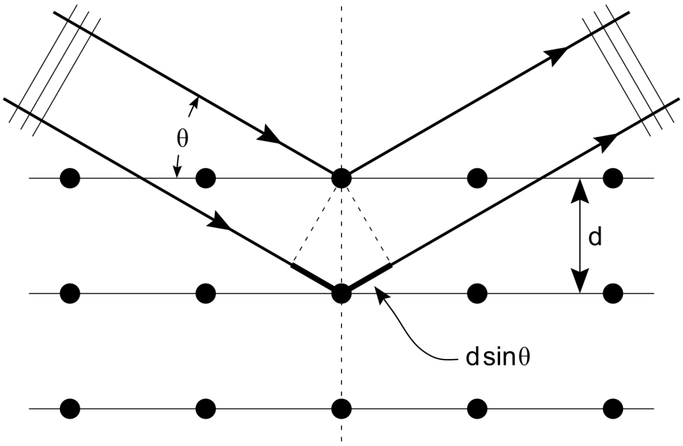

Figure 2.1: Bragg Diffraction: Two waves of identical wavelength (λ) scatter from adjacent lattice planes with a spacing of d. In order to constructively interfere, the difference in path length (d$\sin\theta \times 2$) must be some multiple of the wavelength, leading to the Bragg condition (eq. 2.1). Image downloaded from Wikipedia [25].

of two incoming waves only occurs when the path difference between each wave is some multiple of the wavelength.

Diffractometers take advantage of this law by emitting a constant wavelength λ and varying θ. Using a moving x-ray source and detector as in figure 2.2, points of constructive interference can be measured as a function of θ in the direction normal the surface of the sample stage, thereby measuring the inter-atomic distances parallel to the surface normal, present in the sample. However, the geometry of the diffractometer can be manipulated to measure inter-atomic spacings in any direction of the crystal. The sample stage of the diffractometer can rotate in 2 axes; χ & ϕ; allowing the source and detector to move symmetrically around a wide range of normal vectors, probing inter-atomic spacings in these directions. Scans around many of these variables can provide useful compositional information about a material's

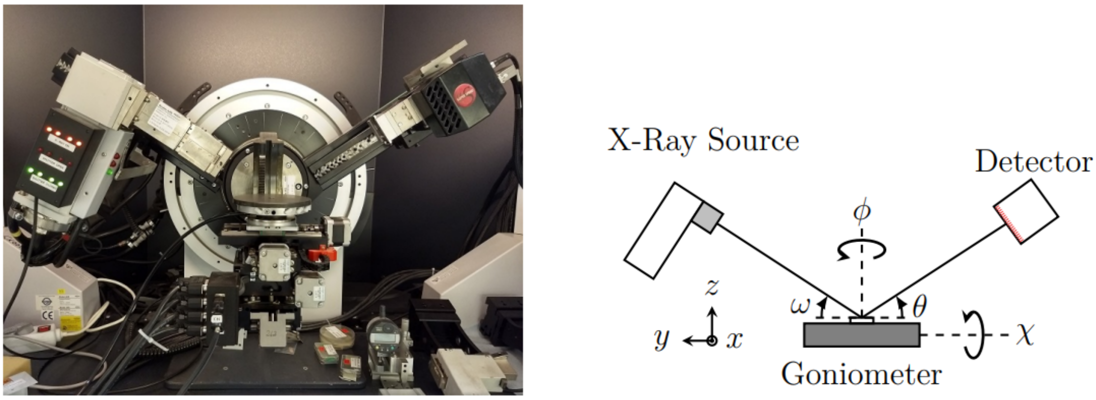

Figure 2.2: A photograph and schematic of the Brukder D8 Advance diffractometer. The sample is placed in the center of the circular goniometer. This system allows precise control of the rotation axes (ϕ, χ), the translation axes (x, y, z) as well as the source and detector angles (ω, θ). Image used with permission [27].

crystals structure. In this work we will focus on identifying crystal phases, out of plane crystal surfaces and in-plane crystal orientations.

The x-ray diffractometer used is a Bruker D8 Advance with a Cu anode. All measurements use an accelerating voltage of 40 kV with a 40 mA emission current. A Göbel mirror is used to create a parallel beam, and a 2-bounce monochromator isolates the K_α emission line from the Cu emission spectrum (wavelength of 1.54 Å). The detector uses a 192 one dimensional linear solid state detecting elements, 0.075mm in width allowing simultaneous measurement along 2.6° . The sample stage allows 360° rotation about the sample normal (ϕ), 90° rotation about the perpendicular axis (χ) and has three dimensional linear translation. The diffractometer and detailed schematic is shown in figure 2.2.

2.2.1 X-ray Reflectometry

Glancing x-rays can be used to measure the thickness and roughness of thin film layers. Essentially, x-rays reflected from the surface and material interfaces will interfere. This gives a low angle symmetric 2θ scan an oscillatory output from which material properties can be extracted. We refer to this technique as X-ray reflectometry (XRR). The theory is comprehensively covered elsewhere [28]; in practice, analysis software is used to simulate and match the output signal, thereby extracting film thickness and roughness. XRR's useful range of thickness measurement is approximately 1–250 nm with < 1 nm resolution typical.

The same Bruker D8 diffractometer is used for XRR, but the detector is rotated 90° so the incident beam is incident on all detecting elements, increasing counts and preventing detector saturation. A 0.1 mm slit is placed in front of the detector to improve resolution, and a knife edge collimator assures the beam does not spill over the sample.

2.3 Electronic Measurements

Resistance measurements have been taken using a 4-point probe and a Keithley 2400 sourcemeter, allowing for sheet resistance measurements and therefore resistivity extraction if the film thickness is less than half the probe spacing. Possessing a heated sample stage, and a bell-jar with a pumping system and gas inlets; this apparatus allows for resistance vs temperature (RT) measurements to be performed, and for measurements to be taken in a variety of atmospheres. Unless highlighted, all resistivity measurements are taken at room temperature in ambient atmosphere on this apparatus.

In Chapter 4, high-frequency pulsed measurements are used to characterise the switching properties of a device. The circuit will be examined in that chapter, but the equipment will be highlighted here. A JANIS probe station is used to house and contact the sample. This apparatus allows needle like probes to be lowered onto a sample. A magnified view and high precision articulation allows accurate and delicate placement. The apparatus also has a heated stage, although the puck is very large and takes some time to change temperature. Although not used in this experiment, the entire apparatus is encased in a vacuum ready environment and can be pumped down, allowing LN2 enabled cryogenic measurements. Different atmospheres can also be pumped into the chamber. To generate input signals, a LeCroy ArbStudio 1102 arbitrary signal generator is used. This powerful tool uses a relatively straightforward general user interface (GUI) that allows programming of incredibly complex waveforms through mathematics, envelopes, manual input etc. However, the standout piece of equipment is the Digilent Analog Discovery 2. This relatively inexpensive piece of equipment possesses signal generation capabilities too, but only the oscilloscope was used in this experiment. Functioning again through a desktop GUI, this device allows automated measurement and storage of oscilloscope data with high resolution at the output rate of the LeCroy signal generator. This allows thousands of measurements to be taken extremely quickly in a format easily processed using scripting languages, ensuring high accuracy of the experiment. I would highly recommend this tool to anyone looking to automate circuit output measurement, due to its low cost and ease of use.

2.3.1 Joule Heating Model

In Chapter 4, a simple Joule heating model is used to describe the temperature of a electronic device as a function of electronic power applied over time. The derivation of this model is presented here. This model is used by Fursina *et al.* in previous work [29].

The rate of return to equilibrium temperature (T_{eq}) is described by relaxation time τ defined as [30]

$$\frac{\partial T}{\partial t} = -\frac{T - T_{eq}}{\tau} \tag{2.2}$$

where τ is dependent on the thermal conductivity of the device and substrate. The heat flux into the sample is given by $dQ_{in}/dt = V \times I$. We further assume that the heat dissipation can be described as:

$$\frac{dQ_{out}}{dt} = -C_v \frac{T - T_{eq}}{\tau} \tag{2.3}$$

Note this model assumes heat capacity C_v and τ are independent of temperature

[31]. The temperature variation with respect to time t considering total heat flux (heating and cooling) of the system is given by:

$$C_v \frac{\partial T}{\partial t} = \frac{\partial}{\partial t}(Q_{in} + Q_{out}) = V \times I - C_v \frac{T - T_{set}}{\tau} \tag{2.4}$$

Solving Eq. 2.4, an expression for temperature is given by:

$$\begin{aligned} T(t+dt) = T_{set} + \frac{V \times I \times \tau}{C_v} &\left[1 - exp\left(-\frac{dt}{\tau}\right)\right] \\ &+ \left[T(t) - T_{set}\right] exp\left(-\frac{dt}{\tau}\right) \end{aligned} \tag{2.5}$$

In Chaper 4, Eq. 2.5 will be used with python to predict channel temperature with data measured for I and V, and fitting parameters C_v and τ.

This model assumes the switching volume is constant and that C_v is a function of volume. Also, this model assumes that C_v and τ are not functions of temperature, which is not a good assumption over larger temperature ranges. This does not impede our experiment in Chapter 4. The implications of these assumptions are discussed there.

2.4 Photolithography

Traditional lithography, invented in 1796 by Alois Senefelder, is a method of print whereby a pattern is deposited onto a surface via oil, polymer, or some other hydrophobic coating [32]. When a suitable ink:water mixture is introduced to the surface, the ink will adhere to the hydrophobic layer while the water will occupy the negative image. Pressing, for example, paper onto the plate will transfer the ink to the paper transferring the pattern or image [33, 34].

Photolithography was introduced in the 1850s, whereby instead of directly painting the coating onto the lithographic surface, the image would be transferred via photography; whether a photograph was used to transfer the image via lithography itself (offset printing), or via other optical methods. Indeed, this is the principal of modern photolithography: the transfer of an image to a surface via optical exposure of some substance on the surface. Here is where the similarities end, as no medium is pressed upon our surface to receive the image i.e. printing. Instead the surface itself is treated and manipulated.

Photolithography is now an widely used technique for patterning micro-scale and even nano-scale designs [35]. Generally, integrated electronic circuits are made from silicon treated with thousands of patterning steps. The basic principals used to make micron scaled devices in this thesis are the same. A photoresist is applied to the sample. Selected parts of the resist are exposed optically in a pattern via a mask. The resist is treated (developed), removing either the exposed or unexposed sections from the sample. Some technique (eg. etching or deposition) is applied to the sample/resist surface. The remaining resist is removed. These steps are illustrated in figure 2.3.

In our laboratories in CRANN, resist is spun onto the sample at a specific spin rate (3000 – 5000 RPM typically) to achieve a the necessary thickness for the specific patterning process. Then, it is soft baked to adhere the resist to the sample. The sample is placed into a UV lithography machine, and pressed against the patterning mask. The patterning mask in our case is a glass plate with the desired pattern printed onto it with metal. The resist is exposed to UV radiation through the mask.

The exposed sections of the resist chemically react when exposed to UV radiation. If the resist is positive, the resist becomes more soluble to a specific chemical or developer, and is therefore removed easily by this solvent. Alternatively, the resist may be negative, and become resistant to the developing chemical upon UV exposure. Depending on the desired device, either may be more suitable. For example, positive photoresists favour patterning close features that cannot touch, as overexposure will only further separate these features. On the other hand, very thin features favour a negative resist, as overexposure will grow the features instead of removing them. Both of these recommendations are context dependent. I want to note that I feel overexposure is riskier than underexposure, as samples can always be re-exposed or left to develop for longer. Features with slight errors are preferable to totally absent or overlapping features.

Now the sample is developed and contains the desired pattern, in our experiments, we treat the sample with either metal deposition or etching. To etch, the sample is exposed to some chemical that the photoresist does not react with, removing material that the resist does not protect. For metals, this is usually an acid. The resist is then chemically removed leaving an etched surface. Metal deposition involves a metal being evaporated evenly onto the sample. Here, lift off is an important step. As the resist lifts from the sample surface, it takes away the metal on top of it. The metal left on the surface should be in the desired pattern. This is also illustrated in figure 2.3.

For most devices, multiple steps of the above methods need to be completed. Each layer needs to be precisely aligned to all the layers below it. Mask design must take this into account, with clear and readable alignment marks put in each mask layer. Two other important features of mask design is density and redundancy. As many devices as possible should be patterned onto every sample, first allowing multiple experiments to be performed, second reducing dependence on a single device, and finally enabling statistical analysis and experimental verification. Due to high levels of random variation (dirt on the sample, condition of resist, output of UV lamp), particular areas of a design may not develop well and single devices should not be relied on.

Chapter 4 relies on a particular device patterned via photolithography; the method is presented here. The samples used consist of 30 nm VO_2 thin films deposited via PLD as outlined in 2.1.1. The sample is cleaned via sonication in acetone and IPA before being hard baked to remove contaminants at 150 °C. Microposit S1813 photoresist is spun onto the sample at 5000 rpm for 50 s and then soft baked at 115 °C for 1 minute. The sample is inserted into an OAI mask aligner, aligned with the mask, put into contact vacuum and exposed. The time of exposure varies between 5–10 s depending on the quality of the resist and the fluorescence of the UV lamp. It is reccomended practise to examine the relevant logbook to clarify how recent exposures have been conducted. The sample is then developed in microposit MF-321 developer. A specific time of development cannot be given, instead, the method is to develop (with continuous agitation) until the exposed sections visibly lift away from the surface, and then wait an additional 15 s. This usually takes under 120 s. The sample should then be immediately transferred to a good volume of DI water, dried, and examined under a microscope to screen for quality.

The first step in this device preparation was an etch step. An Oxford Instruments

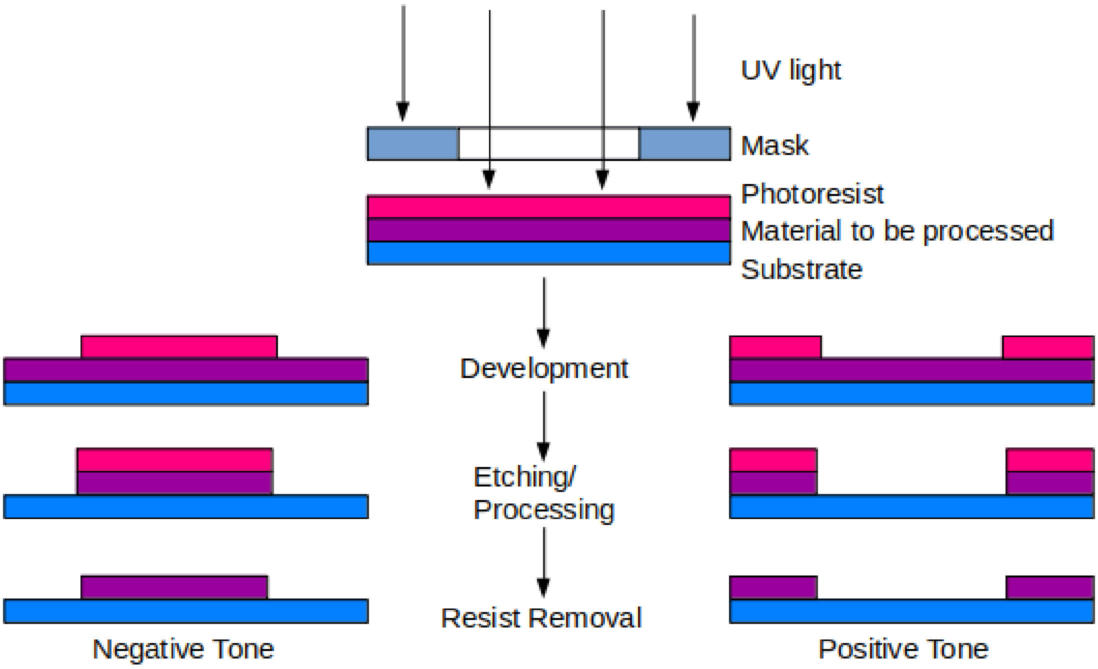

Figure 2.3: This figure depicts the basics of the photolithography process. A shadow mask allows UV light to expose certain areas of a photoresist (pink). This allows the exposed resist to be selectively preserved (negative) or removed (positive) in the development step. In the processing step, the material to be processed (purple) can be selectively affected (etched, doped, layers added). Finally the resist is removed.

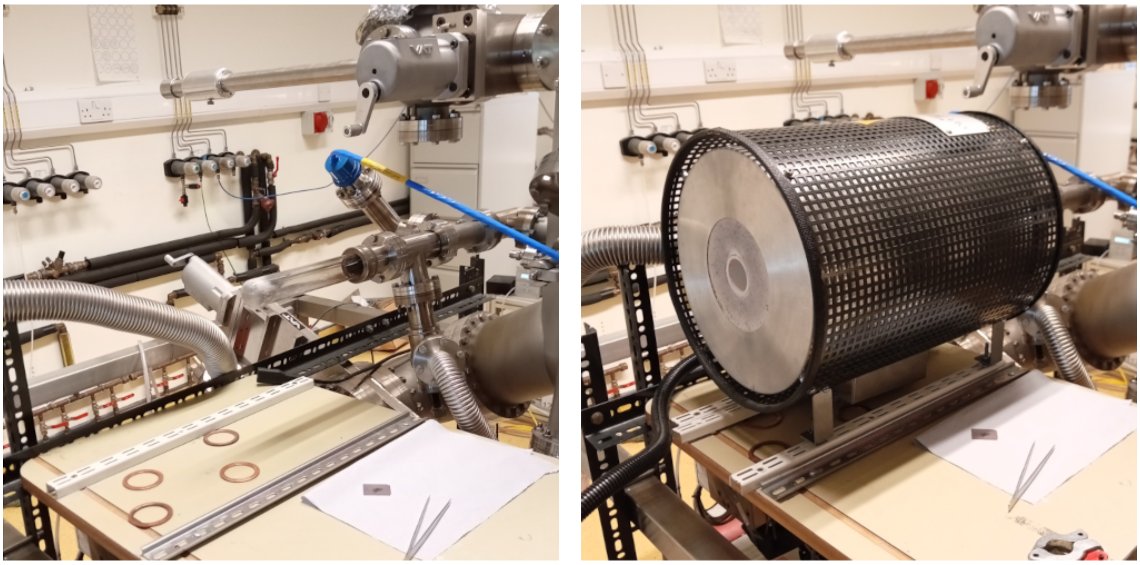

Figure 2.4: Photographs depicitng the low pressure annealing apparatus. Samples are placed in the sealed tube (depicted on the left) and pumped to 10^{-4} Torr. The heated furnace is then slid over tube (right).

inductively coupled plasma (ICP) etcher is used. ICP etching is a reactive ion etching (RIE) technique, where the active etching gas is turned into a plasma as it enters the etching chamber via magnetic fields. The plasma is then accelerated into the sample via an electric field. CF_4 is used to etch VO_2 in this case. The exposed VO_2 is etched all the way to the Al_2O_3 substrate. Acetone was used to clean the remaining resist away after the etch.

The second step was a metal deposition. Metal is deposited via a Temescal e-beam evaporator. Contacts deposited are 5 nm/30 nm Ti/Au contacts, the Ti used for better adhesion, and the Au used for its superior transport properties.

The mask was designed in CleWin software as part of this project, and was fabricated in CRANN's cleanroom facility by Chris Murray using the Heidelberg mask writer and a wet acid etch.

2.5 Low Pressure Annealing

Chapters 5 & 6 use V_2O_5 single crystals annealed in vacuum to reduce the crystal surfaces and provoke a change in properties. The apparatus used for annealing is straightforward. The sample is placed in a glass tube, sealed at one end. A larger vacuum system has a fitting applied to it, allowing the glass tube to be inserted and pumped down using the system turbo pump. A photograph is presented in figure 2.4. A tube furnace fits is slid over the tube, such that the glass tube enters the furnace hotzone, allowing annealing. Pressure in the tube reaches $\sim 1 \times 10^{-4}$ Torr.

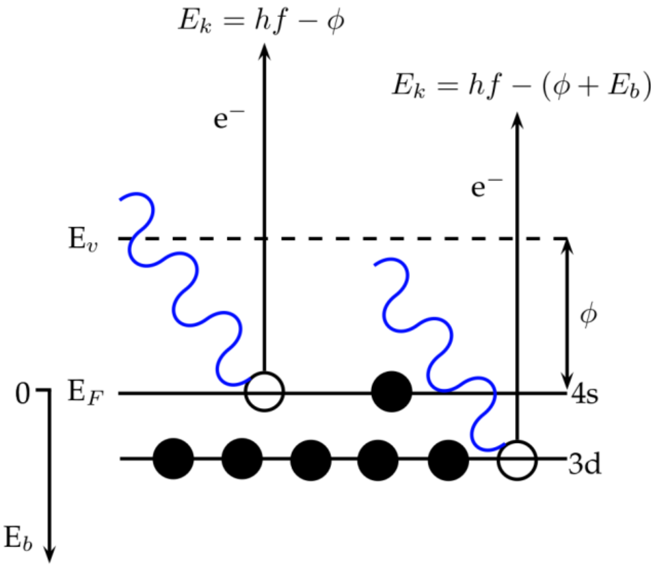

Figure 2.5: Schematic of the photoelectron effect (using Iron in this example). The kinetic energy of any emitted electron is the difference between the absorbed photon energy (hf), and the work function (ϕ) and binding energy (E_b) of the electron prior to excitation. Figure used with permission [36].

2.6 X-ray Photoelectron Spectroscopy

X-ray photoelectron spectroscopy (XPS) relies on the photoelectric effect. The photoelectric effect describes how electrons are emitted from a surface when electromagnetic radiation is incident on the material. Photons of discrete energy are absorbed by electrons. If the photon energy (hf) is greater than the material work function (ϕ) plus the electrons own binding energy (E$_B$), electron emission occurs. The electron uses the remaining energy as kinetic energy (E$_k$) expressed as follows:

$$E_k = hf - (\phi + E_B)$$

This interaction is also described in figure 2.5.

XPS takes advantage of this relation by directing a beam of x-rays of known energy onto a samples surface. If an emitted electron's kinetic energy is measured, its binding energy can be calculated. An electron energy analyser allows for the flux of photoemitted electrons at specific kinetic energies to be measured. As binding energies are somewhat unique for each element, this allows XPS to identify elements. As electron binding energies are altered in bound states, XPS can also identify an element's valence state [37].

Due to the short inelastic mean free path of electrons within solids, XPS is a surface sensitive technique. Depth profiling is material, electron energy and x-ray wavelength dependent.

The depth and specific uses of XPS and other photoemission are vast, and beyond the scope of what needs to be covered here. In this work, XPS is used to identify the valence states present in vanadium oxide samples. The XPS system used in this work is a Omicron Multi-Probe XPS system using monochromated Al K-α X-rays ($hv = 1486.7eV$) and a hemispherical analyser (Omicron EA 125) with a set of seven channeltron detectors.

2.7 Reflectance Anisotropy Spectroscopy

Reflectance anisotropy spectroscopy (RAS) is a non-destructive optical probe which put simply, measures the difference in reflectance (Δr) along two orthogonal axes of a surface plane (x, y). The RAS unit ($\Delta r/r$) used is normalised to the mean reflectance (r):

$$\frac{\Delta r}{r} = 2\frac{(r_x - r_y)}{(r_x + r_y)} \tag{2.6}$$

where reflectances r are complex Fresnel reflection amplitudes. This measurement reveals surface anisotropies of the sample being analysed, and generally speaking, this is due to the anisotropic electron states or bond structures of the surface in question in the region of the Fermi level [38].

The main downside of RAS is the limited materials it can measure. Samples must have an anisotropic surface, therefore isotropic and amorphous materials will not give a reflectance anisotropy (RA) signal. Anisotropic surfaces with randomly orientated domains and anisotropic surfaces with orthogonal domains in the bulk (for example <110> cubic crystals) will not give a RA signal due to signals interfering. However the advantages of RAS include a normal incidence measurement geometry, enabling *in situ* characterisation, and its sensitivity to surface reconstructions, as anisotropic terminations on isotropic surfaces can be measured effectively. Interpretation of RA spectra is non-trivial since the response of the surface depends on the complex dielectric function of the surface, of the bulk and if any other species present in the sample. Comparing the measured RA signals to those calculated via other methods, such as DFT or experimentally measured dielectric functions, RA spectra can be better understood, enabling the practical application of the technique.

The majority of RAS studies to date have been on semiconducting surfaces, investigating surface reconstructions and monitoring their growth. RAS studies of metal oxides include studies on ZnO, Magnetite and superconducting cuprates [39–41].

2.7.1 Experimental Setup

The original RA spectrometer designed by Aspnes [42] is impressive in its simplicity. Reflecting linearly polarised light on a sample rotating with frequency ω gives a time dependent intensity relation.

$$I \propto R - \frac{\Delta R}{2} \cos 2\omega t \tag{2.7}$$

where R and ΔR represent the average and the difference in reflected intensities respectively.

$$R = |r|^2 = \frac{|r_x|^2 + |r_y|^2}{2}, \quad \Delta R = |r_x|^2 - |r_y|^2 \tag{2.8}$$

The ratio of the oscillating component of intensity and time-independent intensity is a direct measure of, $\Delta R/R$:

$$\frac{I_{2\omega}}{I_0} = \frac{1}{2\sqrt{2}} \frac{\Delta R}{R} \tag{2.9}$$

Despite this wonderful implementation, a rotating sample is impractical for most experimental setups, especially when you consider RAS as an *in situ* characterisation technique. None the less, the technique of applying a time dependent modulation to the reflected beam works to give the RAS unit proportional as the ratio of time dependent and independent intensity contributions, a straightforward measurement.

The more commonly employed setup abandons the rotating sample, and uses a static sample and a photoelastic modulator (PEM). A PEM modulates the refractive index of a piezoelectric crystal along a single axis, the orthogonal direction remaining constant. Therefore a single polarisation of incident light is retarded by Γ (with retardation amplitude Γ_0), while the orthogonal component is unaffected. Assuming an oscillation frequency of ω:

$$\Gamma = \Gamma_0 \sin \omega t$$

Using two polarisers, the modulation can be exploited with a simple apparatus. Choosing two arbitrary axes, x and y¸ our incident light will be polarised along $x + y$ initially before reflecting from the surface to be characterised. The reflected light passes through the PEM, which has its modulation axes along $x + y$ also. The light finally passes through an analysis polariser, with its transmission axis aligned to x. The resulting amplitude can be expressed as a function of Jones matrices [38].

$$A \propto \begin{pmatrix} 1 & 0 \\ 0 & 0 \end{pmatrix} \begin{pmatrix} \cos(\frac{\Gamma}{2}) & i \sin(\frac{\Gamma}{2}) \\ i \sin(\frac{\Gamma}{2}) & \cos(\frac{\Gamma}{2}) \end{pmatrix} \begin{pmatrix} r_x & 0 \\ 0 & r_y \end{pmatrix} \begin{pmatrix} 1 \\ 1 \end{pmatrix} \tag{2.10}$$

This relationship can be solved for intensity using harmonic series and Bessel

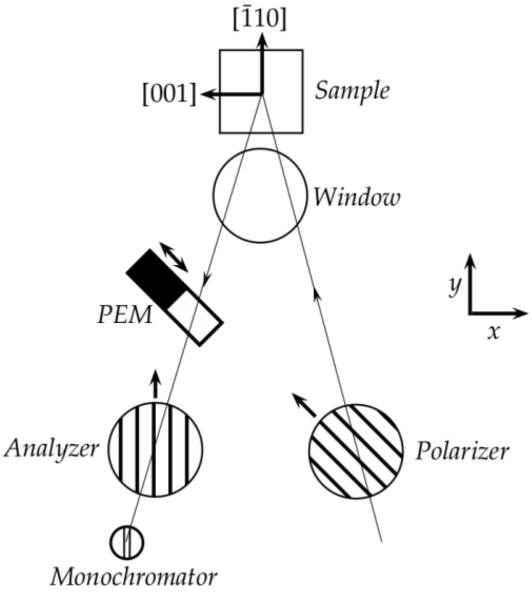

Figure 2.6: The RAS apparatus used in this work. Light from a UV lamp is polarised, reflects off the sample, passes throgh the PEM, passes through an analyser polariser and finally thorugh the monochormator and on to the detector. The PEM and the first polariser have their axes allgined. Sample axes depicted are abritrary. Figure used with permission [36].

functions (J_n). Defining Γ_0 as 2.405 radians gives the result

$$\frac{I_{n\omega}}{I_0} \approx 2J_n(\Gamma_0)\,\mathrm{Im}\left[\frac{\Delta r}{r}\right] \tag{2.11}$$

where n is an odd integer and

$$\frac{I_{n\omega}}{I_0} \approx 2J_n(\Gamma_0)\,\mathrm{Re}\left[\frac{\Delta r}{r}\right] \tag{2.12}$$

where n is even. The RAS unit is directly proportional to the intensity ratios and trivial to convert within software. This technique proves advantageous over the previous apparatus, as the complex quantity $\Delta r/r$ is calculated.

The experimental apparatus is depicted in figure 2.6. The apparatus used is as described above with two polarisers and a PEM, however, our incident light is provided by a xenon lamp due to its suitable spectral range. Using a monochromator and two detectors, the RAS signal is measured in the range 0.8–5.5 eV with high resolution. To extract the intensity harmonics a lock in amplifier is used, synchronised to the PEM.

2.7.2 Two Phase RAS Model

A method of relating the dielectric function to the RA spectrum is essential to this work. We have chosen a simple two phase model published by Aspnes [43] to use in Chapter 6. Aspnes directly relates the complex dielectric function (ϵ) to the RAS unit:

$$\frac{\Delta r}{r} = \frac{1}{\sqrt{\epsilon}} \frac{\Delta \epsilon}{\epsilon - 1} \tag{2.13}$$

where $\epsilon = \frac{1}{2}(\epsilon_x + \epsilon_y)$ and $\Delta\epsilon = \epsilon_x - \epsilon_y$.

This equation is used to model RAS spectra using data either measured directly using ellipsometry or extracted from literature.

2.7.3 Temperature Dependent RAS

This work features materials that exhibit temperature dependent electronic and structural changes. In order to ascertain the effect these transitions have on RA spectra, temperature dependent RAS is employed. Two apparatus are used, one for temperatures above room temperature, and one for cryogenic measurements. Both employ the RAS apparatus described in section 2.7.1 with temperature controlled sample holders.

For above room temperature measurements, samples are stuck to a heating plate in atmosphere. Copper tape is used, and masking tape is used to mask any reflective surfaces other than the sample. The temperature is controlled via a Lakeshore PID heater controller, and temperature is measured using a K-type thermocouple, also taped to the heating plate. The hotplate is clamped in an appropriate position to allow near normal incident reflection from the sample.

For cryogenic measurements an Oxford Instruments optical cryostat is used (figure 2.7). The sample is placed in a measurement chamber with windows, and the whole instrument is pumped. Liquid nitrogen is used to cool the system to 77K, and the system uses a heater with PID controller to heat the system to the desired temperature. The instrument is positioned so the RAS apparatus can reflect light from the sample through the instrument window near normal incidence.

2.8 Ellipsometry

All ellipsometry in this work was performed by Chris Smith in TCD. Ellipsometry is used to extract the real and complex parts of the dielectric function of materials [44]. The method used is variable angle spectroscopic ellipsometry (VASE) [45]. The VASE system used was a SOPRA GESP5, which uses a rotating polariser configuration.

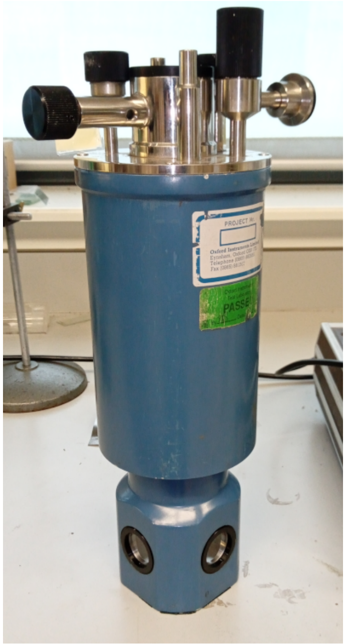

Figure 2.7: Pictured is the optical cryostat. The cryostat is removed from the blue casing, allowing the sample to be mounted. When the casing is reinstalled, the sample is visible through the windows at the bottom. The system is pumped by an *ex situ* pump before LN2 is loaded through the top of the apparatus. A PID controlled heater allows the temperature to be controlled between 77K and upwards of 300K (no LN2 is required for temperatures above room temperature). Optical measurements can be made through the strain free windows.

This system is able to extract axially resolved dielectric components showing the sample optical anisotropy if any exists, making it a useful technique to pair with RAS measurements, as RAS spectra can be directly calculated.

2.9 Transmission Electron Microscopy

Transmission electron microscopy (TEM) results are presented in Chapter 5. Experimental details are presented there. All TEM was performed at the Institute of Solid State Physics, Russian Academy of Sciences, Chernogolovka, Russia by Dr. Andre Mazilkin.

The working principle of TEM is the irradiation of a sample with a focused electron beam, and then measurement of the transmitted electrons. Two principle basic operating modes can be used (i) direct imaging of the sample (ii) fourier transform (through electron diffraction) of the sample. Each method requires different focusing arrangements of the system's lenses. This allows precise sample imaging and resolved crystallographic characterisation. Due to the specific small wavelength of the high energy electrons generated, atomic resolution of the image is possible. Electrons have a small mean free path in solid media, so TEM requires extremely thin samples to allow transmission. These samples or "lamela" are usually prepared via focused ion beam (FIB) etching. Further details of TEM can be found elsewhere [46].

2.10 Computational Methods and Python

Python is an interpreted high-level general-purpose programming language. It a very popular language amongst the scientific computing community [47]. The language itself is very forgiving and functional. With the addition of internet access and a huge community giving support and advice, complex scientific function modelling and programming capabilities are readily available. Python enables very fast and advanced scientific computing in a very accessible format.

Data processing via GUI programs such as Origin or Microsoft Excel is limiting and cumbersome. The volume of data that can be processed is also very small. These programs also require licensing to be used. Python has a "permissive free software licence" which for our purposes is essentially free to use. Python environments such as Spyder are free also.

Generally, I run Python on a system running the Ubuntu operating system, and Python scripts are executed in the shell script or terminal. This facilitates speed and directory manipulation when compared to running scripts a Windows system or through a specific Python environment program.

Almost all data in this work has been processed through python at some level. It allows conversion of file types, consolidation of data, simple and complex calculations, statistical analysis, graphing and much more. Data was generally stored in .csv or spreadsheet file formats. Simulations of mathematical models are presented in Chapters 4 & 6 and were performed through Python. Python allows high volumes of measurement files to be processed and interpreted extremely quickly, and meaningful data generated. Libraries used in this work include: SciPy, Numpy, Pandas, and MatPlotLib.

3

Vanadium Oxides

3.1 Vanadium

Vanadium (V) is an element with atomic number 23, and electronic configuration [Ar] $3d^34s^2$. Although discovered in 1801 in Mexico by a Spanish professor of mineralogy, Andrés Manuel del Rio, it was not identified as a new element until 1830, when Swedish chemist Nil Gabriel Selfström extracted it from cast iron. He named it after Vanadís, the Norse god of beauty and fertility (as well as war and gold). The pure metal is soft and blue in hue, and readily forms an outer oxide layer in ambient conditions. It is the fifth most abundant transition metal in the earth's crust, but is not found naturally in its metallic state. Vanadium is found in about 65 different minerals. In 2019, 90% of vanadium was recovered from magnetite and titanomagnetite ores, with 71% of global supply derived from iron processed for steel production. The main countries producing vanadium are China, Russia and South Africa, with China producing the most in 2019 at 59%. 92% of vanadium is used by the steel industry [48–52].

When vanadium is added to steel, it has a strong affinity with carbon, nitrogen, and oxygen and can generate stable compounds with these elements. Vanadium mainly exists as its carbide in steel, where its main role is to refine the structure and grains of the steel, which reduces the steel sensitivity to overheating, and increases its strength and toughness. During the heat treatment of steel, the compounds produced by vanadium, carbon, and nitrogen in the steel can strongly prevent the grains from growing, resulting in hot-processed steel with a fine structure at room temperature, high strength, and good plasticity and toughness [53]. This use of vanadium in steel would be familiar to users of hand-tools, such as spanners, but vanadium is used in much higher quantities to strengthen steel used in construction, such as rebar. High strength rebar standards introduced by the Chinese government in November 2018 have lead to a notable increase in demand for vanadium. 73 million metric tonnes of vanadium metal was produced in 2019. For context, 1.8 billion metric tonnes of steel was produced in 2019.

The vanadium electronic configuration gives it a number of accessible oxidation states, +2 – +5, giving rise to its reactive chemistry, and the wide range of compounds and minerals formed with the element. Vanadium redox batteries employ vanadium ions in different oxidation states to store chemical potential energy [54].

3.2 Vanadium Oxides

The four accessible oxidation states of vanadium leads to four single valence binary oxide compounds. (i) VO (V^{+2}); this metallic oxide adopts a distorted cubic NaCl structure. Extensive studies on the electronic structure and emission spectra of this substance have been carried out mainly due to its astrophysical importance; VO is found in the atmospheres of cool M-type stars [55–57]. (ii) V_2O_3 (V^{+3}); above 168K V_2O_3 has a metallic corundum structure but transitions to a semi-conducting monoclinic phase at lower temperatures. Its referred to as a canonical "Mott-Hubbard" system, the mechanism enabling the metal-insulator transition [58]. Potential applications of V_2O_3 mainly center around battery technologies [59–61]. (iii) & (iv) VO_2 (V^{+4}) and V_2O_5 (V^{+5}) are central to this work and will be discussed in depth in later sections.

The ability of vanadium atoms to possess multiple stable oxidation states results in the easy conversion between oxides of different stoichiometry by oxidation or reduction. Due to π-bonding between extended V d-orbitals and neighbouring O p-orbitals, the vanadium ions shift from the centers of octahedra, giving rise to internal polarisation, screening of cation-cation repulsion and allowing shorter metal-metal spacing. Removal of oxygen ions from the lattice generates ordered arrays of vacancies followed by rearrangement of metal-oxygen polyhedra and the formation of shear planes. In the case of the $+3 \rightarrow +5$ vanadium oxide system, the result is a large range of mixed valence phases, called Magnéli (V_nO_{2n-1}) or Wadsley (V_nO_{2n+1}) phases [18, 62]. Vanadium oxides have been described as "strongly-correlated electron systems" due to the internal polarisation and dense cation spacing. It is this property that results in the unusual electronic characteristic of metal insulator-transitions seen in many of the vanadium oxide phases.

Vanadium oxides are all classed as toxic and carcinogenic if swallowed or inhaled, so care should be taken when working with these compounds [63, 64].

3.3 VO_2

In 1959, FJ Morin observed a sharp change in conductivity with temperature of a number of metal oxides, including V_2O_3, Ti_2O_3, and vanadium dioxide (VO_2) [2]. Of these materials, VO_2 had the highest switching temperature. VO_2 exhibits a metal-insulator transition (MIT) at roughly 340 K, its resistance dropping by up to five orders of magnitude in single crystals [3]. From a low temperature semiconducting state, the material becomes metallic across a narrow temperature range of ~1 K. Due to the potential applications of this transition, and the accessibility of the switching temperature (compared to the cryogenic or high temperature switching temperatures of many other materials), VO_2 has proven popular and has been widely studied over the last six decades.

Vanadium dioxide has a number of phases including VO_2(M), VO_2(R), VO_2(A), VO_2(B), VO_2(M2) and VO_2(T). All share common coordinations, vanadium existing in an octahedron with a coordination number of 6, oxygen having a coordination number of 3. The M, R and B phases are relevant to this study and described below.

The two primary stable phases of VO_2 take part in the MIT mentioned above. VO_2(R) is the high temperature state. The structure is rutile, space group P42/mnm, with lattice parameters $a_r = 5.7529\,\text{Å}$, $b_r = 4.5378\,\text{Å}$, $c_r = 5.3825\,\text{Å}$ (figure 3.1(a)). VO_2(M) is the low temperature monoclinic semiconducting phase. The space group is P21/c and it has lattice parameters: $a_m = 5.7529\,\text{Å}$, $b_m = 4.5378\,\text{Å}$, $c_m = 5.3825\,\text{Å}$, $\beta = 122.6°$ (figure 3.1(b)) [16]. The structural relationship between these phases is displayed in figure 3.1, where $a_m \parallel c_r$ and $b_m = -b_r$. Cooling through the transition, the vanadium ions form alternating dimer pairs along the $a_m \parallel c_r$ axis, shifting closer together and tilting slightly around the same axis. The resulting V-V alternating spacings are 2.62 Å and 3.16 Å. The oxygen lattice changes very little, the result being two distinct oxygen coordinations O1 and O2 as the metal ions shift around them. The band structures are effectively described via orbital interactions [65–67] and are shown in figure 3.1 (c) and (d). Beginning with VO_2(R), the cation is octahedrally coordinated. Crystal field splitting forms the five orbitals of the 3d electrons. $d_{3z^2-r^2}$ and d_{xy} orbitals point to the oxygen atoms and form direct σ bonds. The remaining 3 orbitals hybridise to form V-O π bonds and a remaining non-bonding $d_{\parallel}$ orbital along the c_r axis. The Fermi level sits in the $d_{\parallel}$ and π anti-bonding bands so the (R) phase is metallic. These combined orbitals are directed along all axes, and conduction is found to be isotropic in this phase. In the (M) phase, vanadium ions along the c_r axis bond together, splitting the $d_{\parallel}$ state into bonding and anti-bonding bands. The shifted V ions results in distorted V-O bond lengths, pushing the $\pi*$ band to a higher energy. The resulting Fermi level is in a band gap. The reported bandgap is 0.7 eV for the semiconducting phase [68],

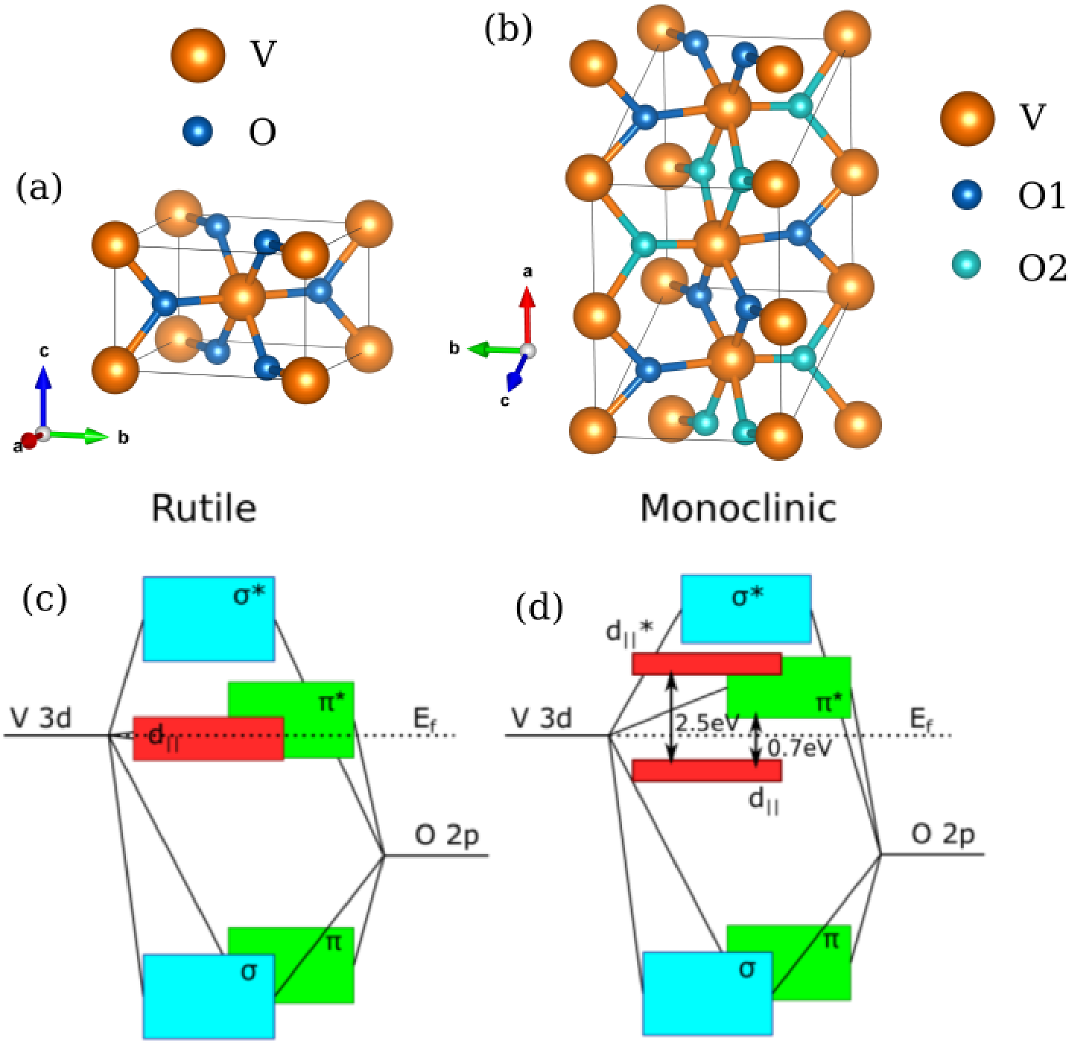

Figure 3.1: The (a) VO_2(R) and (b) VO_2(M) crystal structures. (c) and (d) illustrate the band structures of VO_2(R) and (M) respectively.

between the bonding $d_{||}$ band and anti-bonding π band. The two main models (Peierls and Mott-Hubbard) describing the theory behind the transition are examined in section 3.3.1. Applications of VO_2(R) and (M) phases are mostly linked to this MIT property. Most current research centres on electronic device applications. Simple relaxation oscillators are enabled via the circuit dynamics of the MIT, and these devices have been coupled together [69]. Applications of this technology include Ising machines and other "neural" type problem solving systems including image matching and voice recognition [70–72]. Transistor and switching type devices are also being engineered [9, 10]. Exploitation of the optical absorption over the transition in the infrared is also exploited by technologies such as "smart-windows" [14, 15].

The applications stated above would all benefit from high quality large area deposition of VO_2(M/R) phase films. A large range of techniques have been employed, CVD and PVD methods of all kinds included [17]. Quality of the films is important for all applications as MIT properties degrade quickly as film quality decreases. Larger scale growth of high quality uniform films is still under investigation [73, 74], with MIT property variation across a sample still representing a problem for electronic applications. Tunability of electronic characteristics, such as MIT switching voltage, device hysteresis and power consumption are all desirable features. The modification and physical understanding of these properties is a focus of this work in Chapter 4 and Chapter 5.

VO_2(B) is a metastable structure which undergoes an irreversible transformation to VO_2(R)/(M) with heating [75]. It has a monoclinic layered structure (figure 3.2) closely related to V_2O_5 and V_6O_{13} structures (section 3.6). It shows a type of MIT too, but it is unusual compared to the other vanadium oxides, occurring gradually between 180 K and 300 K [76]. The change in resistance is large, recorded at 5 orders of magnitude. The structural transition again shows V-V bonding along the c-axis, however the structure distorts very little and is described as small contraction of the c-axis and expansion of the a- and b-axes. The structure given here is the high temperature phase, which is monoclinic with space group C2/m and lattice constants $a = 12.03\,\text{Å},\ b = 3.693\,\text{Å},\ c = 6.42\,\text{Å},\ \beta = 106.6°$ [76–79]. Similar to V_2O_3, current interest in VO_2(B) applications centers on battery technologies [80].

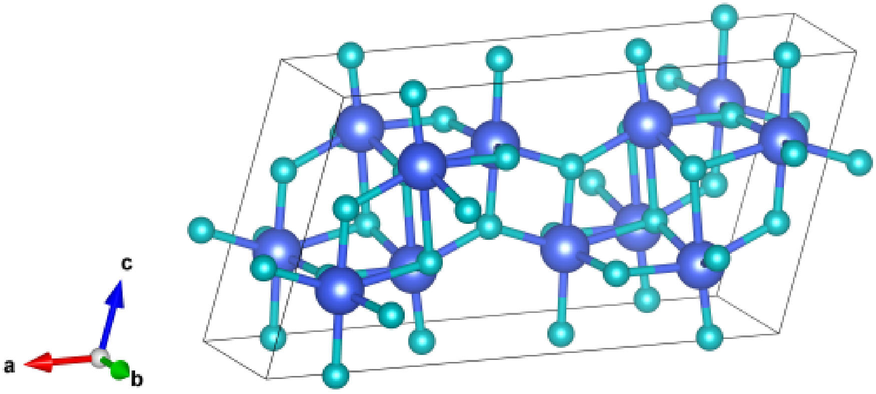

Figure 3.2: Crystal structure of VO_2(B).

3.3.1 Metal-Insulator Transition of VO_2

As stated, VO_2(M) goes through a MIT at 340 K and structurally transforms to VO_2(R). The metal-insulator transition (MIT) is a topic of long standing interest in condensed matter physics and materials sciences [2, 7, 81]. This transition deals with the increase in conductivity of a material with external stimulus such as heat (figure 3.3) [2], light [82], strain [83] or electric field [84]. Systems exhibiting MIT behaviour include organic compounds [85] and transition metal oxides [86, 87]. Along with the resistivity, optical [88] and magnetic properties [89] can also undergo a sharp change through these transitions. Generally, the control parameters for the MIT can be classified into three categories: temperature control; bandwidth control [83] (*e.g.* strain); and band-filling control [90] (*e.g.* doping or applied fields), although more specific classifications can be found in an article by Imada *et al* [7].

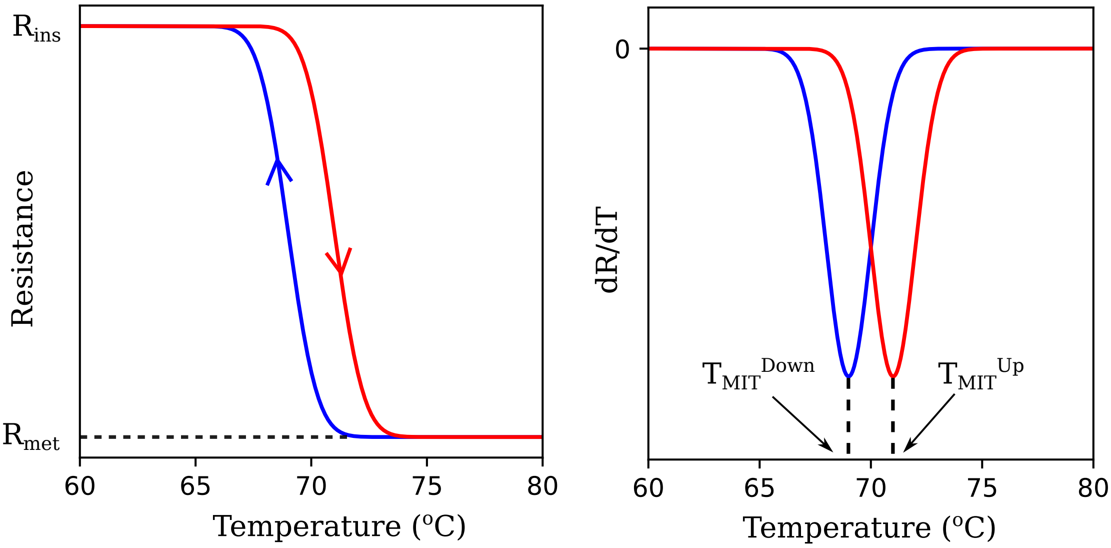

Figure 3.3: Typical heat triggered MIT of VO_2, with resistance vs temperature shown on the left, and the first derivative shown on the right. Resistivity change is expressed as the ratio of low to high resistance (R_{met}/R_{ins}). MIT transition temperature is taken as the temperature at the minimum of the first derivative, due to hysteresis (T_{MIT}^{Up} - T_{MIT}^{Down}), the transition temperature is taken as the average between these values: (T_{MIT}^{Up} + T_{MIT}^{Down})/2

This resistivity change in VO_2 has been shown to be as high as a factor of 10^5 in single crystals, and to take place over 1 K [3, 16]. The transition has a hysteresis of about 1 K [91]. As well as temperature, applied voltage, mechanical strain and optical excitation can trigger the MIT [4–6]. Two different theories attempt to describe the MIT in VO_2, Mott-Hubbard and Peierls.

Mott-Hubbard is a purely electronic description, based on Nevill Mott's "Mott insulator" theory, which he published in 1949 [92]. Mott argues that in certain lattices with free electrons, repulsion between electrons within the lattice will prevent adjacent bonding and conduction from occurring. Any energy applied to the system, for example heat, will serve to create a bound pair of carriers. However, Mott suggests that if there is a high enough electron density of free electrons or carriers, the electron repulsion between ions will be screened. Mott's theory equates the binding energy of a bound carrier pair to the screening potential generated by free electrons to estimate the electron density necessary to screen repulsion and cause an abrupt shift to a conducting state [81]. Although certainly a clever description, it is usually more practical to visualise this transition in the context of band structures.

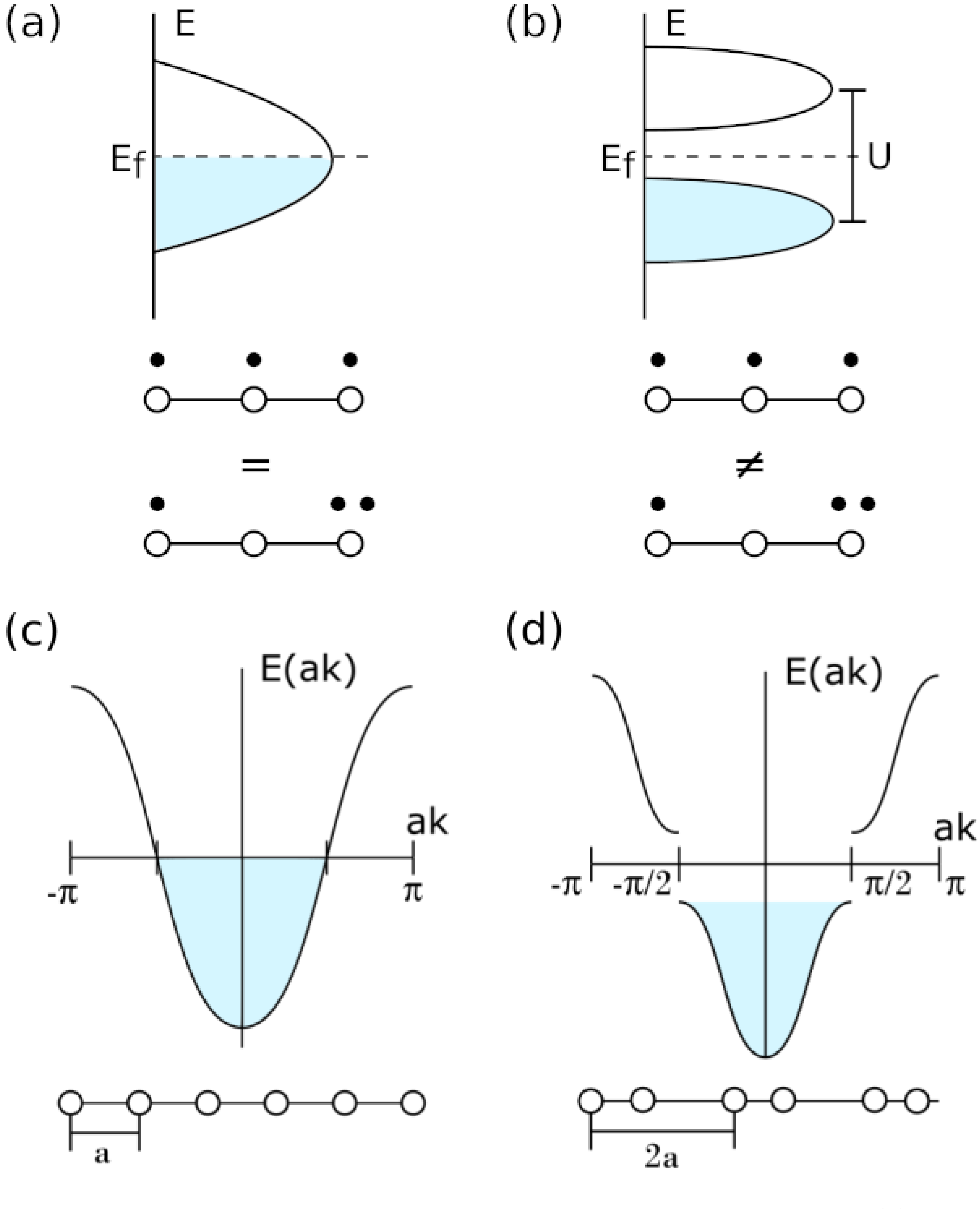

Figure 3.4: Illustrations of the Mott-Hubarrd and Peierls theories. (a) and (b) depict the Mott-Hubbard transition. (a) illustrates a system where an electron on a singley and doubly occupied state has the same energy (no repulsion). This results in a single half occupied band. (b) demonstrates that if the electrons repel with repulsion U, single and double occupied states will have different energies and will therefore create two bands seperated by this energy. (c) and (d) depect the Peierls transition. A chain of atoms with a single electron will generate a single band if evenly spaced (c) but will become two bands if every second atom shifts (d). This results in a net energy saving in this example.

Mott-Hubbard theory does just this [93]. This theory describes singly occupied electron bands that split when the appropriate conditions are met. The argument is that moving electrons from their singly occupied site to an adjacent site will cost an energy U, the repulsive energy between electrons on a doubly occupied site. This cost is represented as a bandgap. An illustration of this an be seen in figure 3.4 (a) and (b). In the context of VO_2, this theory is applied to the $d_{||}$ band along the c_r axis. The band is split due to repulsion between electrons in the V-V dimers, blocking conduction in this axis. This theory also accounts for the size of the bandgap observed [16]. However, this theory does not account for why the vanadium ions form dimers in the first place. In fact, Mott's theory requires the π^* orbitals to screen the electronic repulsion to enable the metallic state, but without the crystal distortion, the π^* orbitals would not shift upwards in the insulating state even as the $d_{||}$ band splits, leaving the material metallic. An effective "pure" Mott transition would require the crystal structure to remain undistorted throughout.

Peierls theory is conceptually clearer [94]. An infinite one dimensional chain of ions with a single outer electron will form a parabolic half filled band structure. However, if each second ion binds with every other ion and shifts towards it, the lattice spacing effectively doubles. This halves the Brillion zone of the band structure, creating a full lower valence band, and an upper empty conduction band. This is illustrated in figure 3.4 (c) and (d). In doing this the total energy of the system is lowered. Applying heat, electrons are excited to the conduction band. When a critical number of electrons reaches the upper band, the added entropy of these electrons leads to a disappearance of the distortion and hence the energy gap. This theory fully accounts for the ion movement in the $d_{||}$ band of VO_2, and effectively describes the π^* band shift due to the distortion. The limiting factor of this theory is the band gap created between the upper and lower $d_{||}$ bands, as the expected energy from this theory ($\sim$0.3 eV) comes up short of the experimental value (0.7 eV) [16,68].

The clearest outcome is that the fully described MIT from VO_2(M) to VO_2(R) is some combination of both theories. However, work has been done to isolate the driving mechanisms, particularly the Mott transition, with the intention of driving a resistive switch without a structural distortion, a metallic monoclinic phase. Recent studies suggest this phase is not attainable [95,96].

The VO_2 transition is also greatly affected by structural and morphological manipulations. The stability of the MIT is strongly correlated to the crystallinity: while single crystal VO_2 exhibits the largest and sharpest transition, the inability to accommodate strain results in cracking [97]. Domain boundaries provide an effective way to accommodate strain. However, relaxation at the boundaries can modify the transition [98] and inhomogeneity at the boundaries widens the transition. Ion mobility, thermally or electrically induced, can modify the material and the MIT characteristics. It is less pronounced in crystalline VO_2 in which the barrier for ion mobility is greater.

Although single crystals have shown a 5 order of magnitude change in conductivity, this is reduced in thin films to 4 orders at most [73], but more commonly about 3 orders of magnitude. Grain size contributes to the transition size, higher grain boundary concentrations reducing switching magnitude [99, 100]. Thinner films usually result in inferior switching properties [100], but this is likely due to film quality and grain size improving with thickness, as high precision systems have developed films as thin as 3 nm with good switching characteristics [101, 102]. Doping, mechanical strain and oxygen content can change the transition temperature by changing the internal electron concentration in the crystal [103–105]. Hysteresis and width in the temperature driven transition is generally due to some variation in the crystal (stochiometry or strain gradient), as domains with different transition temperatures give a gradual "percolative" change [106]. The control and understanding of these morphological features and effects is of great importance to the application of VO_2 in future applications.

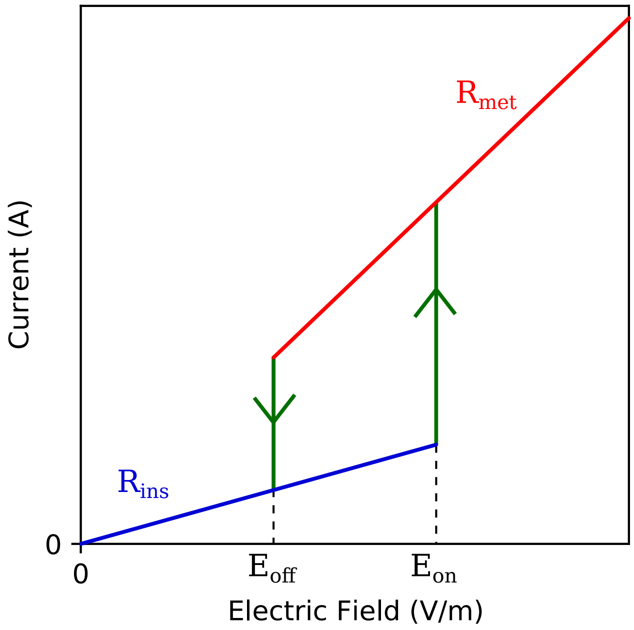

Figure 3.5: Typical e-MIT of VO_2, illustrating characteristic values such as the switching fields (E_{on}, E_{off}) and e-MIT hysteresis (E_{on} - E_{off})

VO_2 has also been shown to exhibit an MIT when subjected to external electric fields (figure 3.5). When the MIT is triggered via electric current, this is referred to as resistive switching (RS). However, the origin of the RS may be due to both the electronic field applied (carrier injection), and the Joule heating effects of the electricity [107]. The pure electric field induced transition requires fields of the order of 10^7 V/m [4], while in Joule heating dominated RS, the electric field is a few orders of magnitude smaller [108–112]. Experiments have isolated both mechanisms [113, 114], but in general both mechanisms contribute to RS in micron scale devices and channels simultaneously. VO_2 RS takes place at either voltage polarity with well-pronounced hysteresis [115]. In many examples, the power required to trigger the MIT in the insulating state is equal to the power required to maintain the metallic state before it returns to the insulating phase [116]. Electronic applications of VO_2 exploit the RS [9]. To enable facile implementation of many applications, control over the RS parameters: such as required power, switching voltages, switching magnitude and hysteresis; is desirable. The modification and physical understanding of these parameters is a focus of this work in chapter 4 and chapter 5.

3.4 V_2O_5

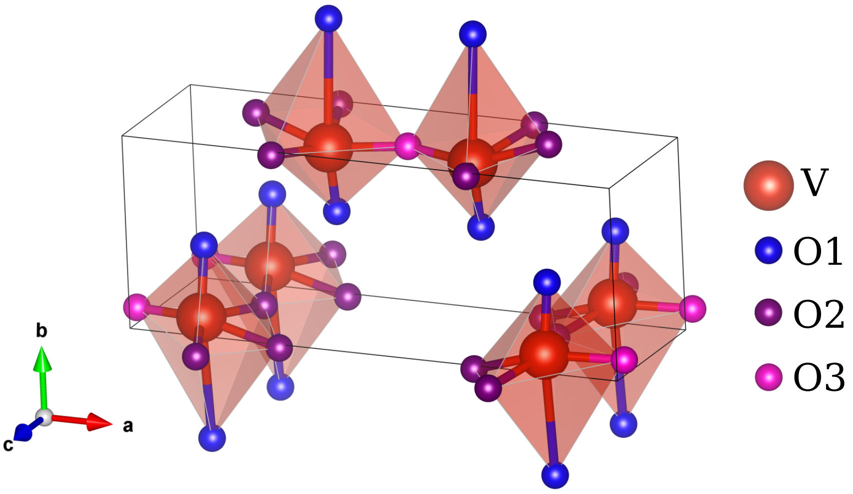

Figure 3.6: Crystal structure of V_2O_5.

Vanadium finds itself in its highest oxidation state, +5, in V_2O_5. V_2O_5 is a semiconductor. It has a layered orthorhombic structure (figure 3.6), space group Pmmn, and lattice constants $a = 11.512\,\text{Å}$, $b = 3.564\,\text{Å}$, $c = 4.368\,\text{Å}$ [117]. V_2O_5 polyhedra can be considered to be distorted tetragonal pyramid (five V-O bond lengths of 1.58-2.02 Å or distorted octahedron (with a sixth V-O bond of length 2.79 Å). The tetragonal pyramids form sheets in the (010) plane by sharing edges with adjacent pyramids, but are weakly bonded to the sheets above and below due to the long V-O bond in that axis. These weak V-O bonds give rise to easy cleavage between sheets, giving rise to a (010) surface [18].

There are three types of oxygen co-ordinations. O1 ions connect adjacent sheets in the y-axis, with bond lengths of 1.576 Å and 2.793 Å. O2 bridge V ions in the y axis and have bond lengths of 1.778 Å. O3 are bonded to 3 vanadium ions, two 1.877 Å bonds in the z axis, and one 2.017 Å bond in the x axis. It should be clear that V_2O_5 possesses clear structural anisotropy. The V_2O_5 structure contains large cavities in all axes, so oxygen lattice mobility is high.

It should be no surprise the band structure of V_2O_5 reflects this anisotropy. V_2O_5 shows an indirect bandgap of 2.3 eV at the Γ point and a direct bandgap of 1.9 eV [118]. The (010) surface has an indirect bandgap of 2.1 eV [118]. The conduction band is split into and upper band, and a lower band referred to as a split-off band. The gap between the VB to upper CB band is 3.3 eV [119]. The origin of this narrow split off band is due to bridging V-V $3d_{xy}$ orbital interactions via intermediary O2 $2p_y$ orbitals in the same lattice sheet. Absorption has been shown to be weak at low energies in the $\langle 001 \rangle$ direction as a result of these directional lower conduction bands, leading to clear optical anisotropies [118, 119].

In terms of applications, V_2O_5 is used as a catalyst, such as in the production of sulphuric acid for example [120], has applications in gas sensing [121] and battery technology [122, 123]

3.5 Mixed Valence Vanadium Oxides

The ability of vanadium ions to possess multiple stable oxidation states results in conversion between oxides of different stoichiometry. Between each single valence state, there is a range of mixed valence phases. Focusing on the phases between V_2O_3 and V_2O_5, we have two distinct ranges of mixed oxide systems with separate structural relationships. The Magnéli phases, possessing mixes of +3 and +4 vanadium valences, with general formula:

$$V_nO_{2n-1} \quad 3 \leq n \leq 9$$

and Wadsley phases, mixes of +4 and +5 with formula:

$$V_nO_{2n+1} \quad 3 \leq n \leq 6$$

Apart from V_7O_{13} which is metallic, all Magnéli phases go through a first order MIT, accompanied by structural transformations. Structurally, these phases are a mixture of vanadium dioxide like rutile and vanadium sesquioxide corundum type structures. The phases gradually transition between these two structures by shear reconstructions as a result of oxygen vacancies. Magnéli phase MITs arise as a result of both electron lattice interaction within the dioxide-like and electronic correlations within the sesquioxide-like regions of the crystal [62, 124].

A Magnéli phase of particular note is V_3O_5, the only phase with a MIT temperature to VO_2 at 430 K. Despite the technological potential of this property, difficulty in isolating this phases prevent its further study. In fact, generally speaking, isolating mixed vanadium oxide phases, especially in thin film form, is difficult due to their facile reformation into adjacent phases in ambient conditions.

3.5.1 V_3O_7, V_4O_9 and V_6O_{13}

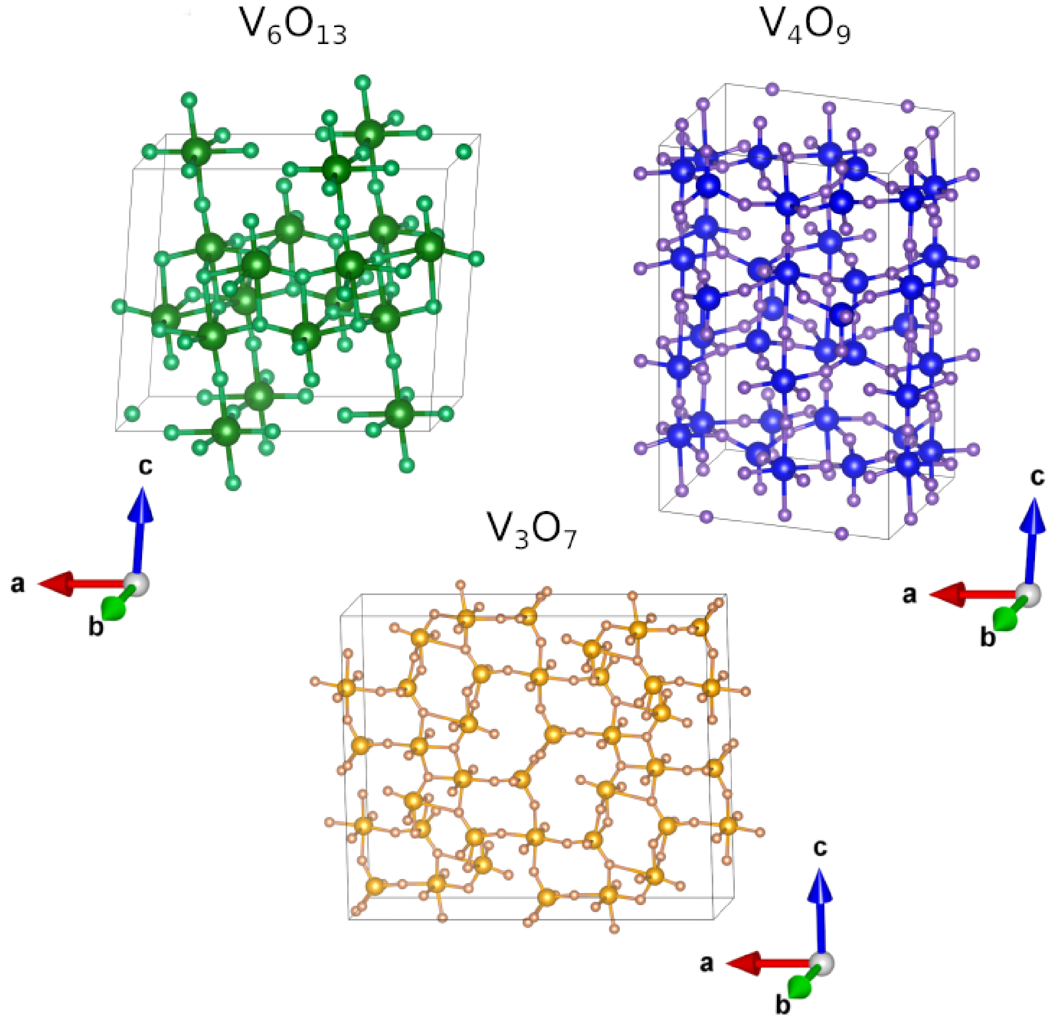

Figure 3.7: Crystal structures of V_6O_{13}, V_4O_9 and V_3O_7. Structures are not to relative scale.

The family of Wadsley phases is smaller, the studied phases consisting of V_6O_{13}, V_3O_7 and V_4O_9. Of these phases only V_6O_{13} has a MIT. The other two phases are semi-conductors. Wadsley phases have structures derived from the V_2O_5 structure with VO like polyhedra.

V_6O_{13} has a MIT at 150 K. V_6O_{13} has a similar monoclinic structure above and below the transition with lattice parameters above of: $a = 11.92\,\text{Å}$, $b = 3.68\,\text{Å}$, $c = 10.14\,\text{Å}$, $\beta = 100.87°$ (figure 3.7) [125]; and below of: $a = 11.96\,\text{Å}$, $b = 3.71\,\text{Å}$, $c = 10.06\,\text{Å}$, $\beta = 100.93°$ [126]. Clear structural anisotropies are evident with different bond structures in each axis, which are expected to manifest in optical and electronic anisotropies. Anisotropic conductance has been recorded in the high temperature state, with resistivity along the b-axis 10^2 times lower than the c-axis [127]. The MIT mechanism of V_6O_{13} is not understood or studied as well as the transition of some of the more popular phases *e.g.*, VO_2. It has been proposed, that instead of a correlation driven transition occurring, as in VO_2, a charge reordering occurs. At low temperatures, the valance of vanadium ions is strictly +4 or +5, referred to as "spin-paired behaviour". As the transition is crossed, the charge redistributes more evenly across ions, referred to as "strongly correlated narrow band behaviour" accompanied by a structural change [128]. The primary suggested application for V_6O_{13} has been as a cathode material for Li-ion batteries [129].

V_4O_9 and V_3O_7 are both semi-conducting Wadsley phases. Due to their lack of MIT properties, these phases have not been researched as much as many of the other vanadium oxide phases. They are mainly discussed in terms of V_2O_5 reduction pathways, and will be discussed in this context in section 3.6. V_4O_9 is orthorhombic (figure 3.7) with parameters: $a = 10.36\,\text{Å}$, $b = 8.17\,\text{Å}$, $c = 16.56\,\text{Å}$ [130]. V_3O_7 is monoclinic (figure 3.7) with parameters: $a = 21.92\,\text{Å}$, $b = 3.67\,\text{Å}$, $c = 18.34\,\text{Å}$, $\beta = 95.61°$ [131].

These Wadsley phases generally are not grown in isolated crystal or thin film forms, but rather studied in the reduction pathways of V_2O_5 crystals and films (Section 3.6), and are present in with a mixture of phases in this context. Some studies of V_6O_{13} thin films have been claimed, but these do not show the V_6O_{13} characteristic MIT transition and are generally discussed in terms of Li battery applications [132, 133]. This outlook is not particularly relevant to this work. V_3O_7, V_4O_9 and V_6O_{13} have been prepared via mixtures of V_2O_3 (or sulfur in the case of V_4O_9) and V_2O_5 annealed together and processed to create polycrystaline powders and select small single crystal samples [130, 131].

3.6 Structural Relationships and the Reduction of V_2O_5

It is well documented that vanadium oxide phases structurally transform to alternative phases due to variations in composition. In the vanadium oxide the reconstructions can be described in terms of two families of structures. V_2O_3 (corundum) to VO_2(R) are structures derived from a $P6_3/mcm$ space group. Intermediate Magnelli phases are combinations of these corundum and rutile structures, and gradually transform between these two parent structures via shear reconstruction after the formation of vacancies [62]. VO_2(B) to V_2O_5 phases are derived from the VO rock-salt structure,

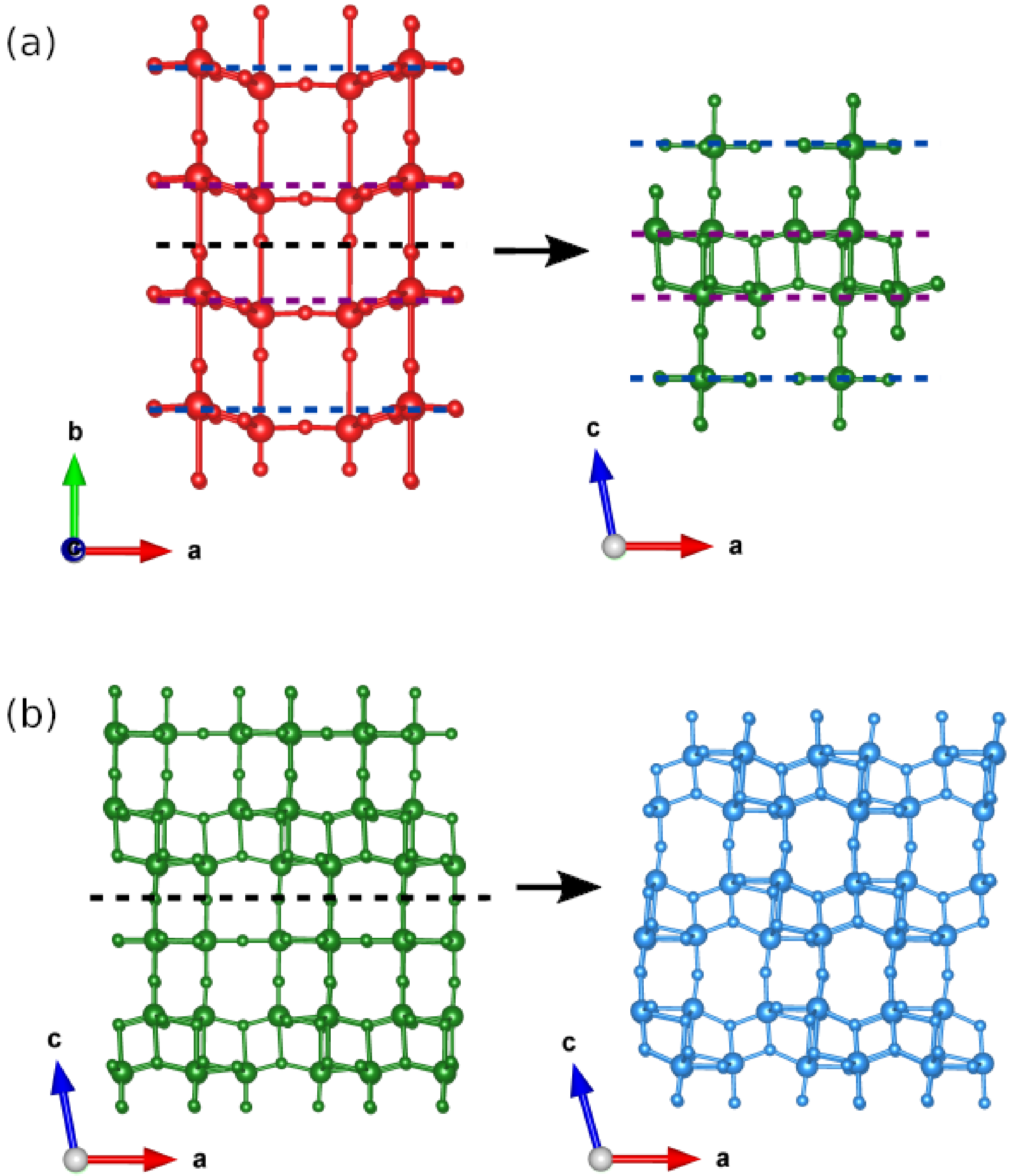

Figure 3.8: Illustration of the reduction of (a) V_2O_5 to V_6O_{13} and (b) V_6O_{13} to VO_2(B) via the removal of oxygen layers. Removed layers indicated by the dashed black like. Epitaxial relationships are maintained during reduction.

$Fm\bar{3}m$ space group. Similarly, intermediate Wadsley phases structures are a result of shear transformations between these parent structures as oxygen vacancies form [124].

Experimentally, this distinction between the V_2O_3 – VO_2(R) system and the VO_2(B) – V_2O_5 system becomes relevant in reduction or transformation studies. As we move within a structural system, the surfaces and phases formed will form epitaxially, or in direct relation to the previous phase, and certain surfaces can be expected in measurements such as XRD. However, the transformation between these systems, from VO_2(B) to VO_2(R), bears less of a relationship and therefore will have a less predictable orientation and morphology.

Thermal reduction of V_2O_5 is a well documented process, and the oxide phases produced depend on reducing conditions [19, 134–137]. The V_2O_5 structure enables facile transport of oxygen and oxygen vacancies throughout its structure [18]. The reduction and transformation of V_2O_5 is therefore governed by two processes, diffusion of oxygen through the bulk, and absorption/adsorption of oxygen at the crystal surface. Above 530 °C, reaction kinetics are limited by surface chemistry, as bulk diffusion is substantially faster than surface exchange [136]. It has been recorded that V_2O_5 does not decompose above 530 °C in UHV ($10^{-8}-10^{-10}$ Torr) due to this, and any decomposition in this environment is due to surface contaminants. When reduction does occur at higher temperatures, V_2O_5 typically reduces to V_6O_{13} [19, 125], skipping V_3O_7 and V_4O_9 phases, which are present in reductions at lower temperatures [138, 139]. If reduction is continued, VO_2(B) follows both V_4O_9 and V_6O_{13} [130] before an irreversible transformation to VO_2(R) [75]. Reduction beyond this will continue to Magnéli phases and V_2O_3 [135]. Multiple phases can coexist during, and are stable after, the reduction process.

V_2O_5, V_6O_{13} and VO_2(B) have the most straightforward structural relationship. Removal of every 3rd layer of oxygen atoms in the <010> direction in V_2O_5 and a small shear reconstruction leads to the V_6O_{13} structure. A removing further oxygen with a similar reconstruction results in VO_2(B). This process is shown in figure 3.8. In this reduction the phases will remain epitaxial and retain the same crystal orientation [18]. The transformation of V_2O_5 to V_4O_9 and V_3O_7 is more subtle, but is based on ordered vacancy formation. V_4O_9 has been described as a superstructure of the V_2O_5 crystal in a paper by Grymonprez et al [140]. This paper also describes the possible V_2O_5 oxygen vacancies that will lead to the V_4O_9 structure. Less is written in regards to the transformation of V_2O_5 to V_3O_7.

In terms of symmetry retained during reduction literature and my own work shows: V_2O_5\{010\} // V_6O_{13}\{001\} // VO_2(B)\{001\} // V_4O_9\{001\} // V_3O_7\{010\}

And: V_2O_5<100> // V_6O_{13}<100> // VO_2(B)<100>

A matching in-plane direction for V_4O_9 and V_3O_7 is unclear.

Reduction from VO_2(B) to VO_2(R) is a transformation between the two crystallographic systems. For the VO_2 stoichiometry, rutile is thermodynamically favourable, and the transformation is irreversible [75]. As VO_2(B) has been shown to evolve through an intermediate phase of higher symmetry before a reconstructive transformation to VO_2(R) [141]. Therefore, the retention of symmetry to the previous V_2O_5 system is not maintained, and literature points towards a polycrystaline VO_2(R) structure.

3.7 Tables of Material Characteristics

Tables of material characteristics for the relevant vanadium oxide phases are presented here. Table 3.1 gives the known resistivities, densities and oxygen:vanadium (O/V) ratio of each phase. Table 3.2 includes the phases with MITs, and shows both transition temperature (T_T) and switching magnitude. Switching magnitude (R_{ins}/R_{met}) is defined as the insulating state resistance (R_{ins}) divided by the metallic state resistance (R_{met}). Table 3.3 gives the structural properties of the vanadium oxide phases.

Phase	Resistivity (Ω.m)	Density (g.cm^{-3})	O/V ratio
V_2O_5	1-100 @ 300K [142]	3.36 [143]	2.5
V_3O_7	Higher than V_6O_{13} insulating phase [131]	3.62 [131]	2.33
V_4O_9	Unknown. Mixed V_2O_5 and V_4O_9 films: 0.01 [139]	3.25 [140]	2.25
V_6O_{13}	10^{-3} - 10^{-5} @ 300K [127]	3.89 [144]	2.17
VO_2(B)	10^{-4} @ 300K [145]	4.03 [75]	2
VO_2(R)	10^{-6} [146]	4.65 [143]	2
VO_2(M)	0.076 @ 300K [146]	4.57 [143]	2

Table 3.1: Resistivity, density and oxygen:vanadium ratio of VO phases.

Phase	T_T (K)	R_{ins}/R_{met}
V_6O_{13} [126]	150	10^4
VO_2(B) [76]	180-300	10^5
VO_2(R)/(M) [147]	340	$10^3 - 10^5$

Table 3.2: Transition temperatures and switching magnitudes of metal-insulator transitions in VO phases.

Phase	System	Space Group	a (Å)	b (Å)	c (Å)	β (°)
V_2O_5 [117]	O	Pmmn	11.512	3.564	4.368	90
V_3O_7 [131]	M	C2/c	21.92	3.67	18.34	95.61
V_4O_9 [130]	O	Cmcm	10.36	8.17	16.56	90
V_6O_{13} (above T_T) [125]	M	C2/m	11.92	3.68	10.14	100.87
VO_2(B) [77]	M	C2/m	12.03	3.69	6.42	106.6
VO_2(R) [16]	O	P42/mnm	4.55	4.55	2.85	90
VO_2(M) [16]	M	P21/c	5.75	4.53	5.38	122.6

Table 3.3: Structural properties of VO phases.

4

Controlling the Resistive Switching Hysteresis in VO_2 Thin Films via Application of Pulsed Voltage

As discussed in 3.3.1, VO_2 exhibits a MIT, which can be triggered via an applied electric field. The use of an electric field to induce a change in resistivity is referred to as resistive switching (RS), and has attracted much attention due to the potential applications in electronics such as oscillators, neuromorphic devices and memory [9, 148]. For many RS systems, the I-V curve shows some level of hysteresis, i.e. the current does not retrace itself in voltage sweeps up and down (figure 3.5) [85, 149].

VO_2 exhibits RS when external electric fields of $6.5 \times 10^7\,\mathrm{V\,m^{-1}}$ are applied across it [4]. VO_2 RS takes place at either voltage polarity with well-pronounced hysteresis [115]. In many examples, the power required to trigger the MIT in the insulating state is equal to the power required to maintain the metallic state before it returns to the insulating phase [116].

The mechanism for the VO_2 RS is debated, with arguments made for temperature control via Joule heating, and band-filling control via carrier injection [107]. Experiments using different methodologies have isolated these mechanisms [113, 114], but in most cases both simultaneously contribute to the RS. Understanding the relative contributions of the mechanism in any given system is important. Furthermore, understanding the dynamics of each mechanism - for example temperature change induced by Joule heating - can provide insight into morphology, structure and phase changes, which is vital for device optimisation. Ideally, in electronic applications, heat fluctuations and power dissipation should be kept to a minimum to reduce energy consumption and mitigate adverse heating effects, while the ideal profile of the hysteresis varies between applications [148]. For example, a switch or relaxation oscillator may benefit from no hysteresis, while memory applications would benefit from a large hysteresis. The ability to tune this I-V profile is therefore an important consideration in RS devices.

In this chapter, we determine the origin of hysteresis in RS of VO_2 thin films. The influence of pulsing on hysteretic behaviour and the temperature profile is discussed. Through both continuous and pulsed voltage measurements we show that the hysteretic behavior originates from local Joule heating of the channel once the system is switched to the low-resistance state. We further demonstrate how pulsing - in particular the time between pulses - can change the hysteresis. A thermal model, predicting channel temperature using only Joule heating and environmental cooling, agrees with the data and predicts substantial temperature fluctuations between the metallic and insulating states. The model demonstrates that one needs to consider heating and thermal conductivity beyond the VO_2 material itself.

4.1 Experimental Procedure

All procedures outlined in this Chapter were performed by myself. Prof. Igor Shvets and Dr. Brian Walls assisted in exprimental design and discussion.

Textured VO_2 thin films were grown on c-plane sapphire substrates via pulsed laser deposition to 30 nm thickness as described in section 2.1.1. During growth the substrate was held at 600 °C, base pressure was approximately 1×10^{-5} mbar, O_2 pressure was held at 15×10^{-3} mbar. Laser fluence used was $170\,\mathrm{mJcm^{-2}}$, pulsed at 10 Hz with a 25 ns pulse length. The films were characterised by x-ray diffraction and resistance measurements, showing the VO_2<010> family of reflections (figure 4.1) [150,151], and an approximately 3 order of magnitude resistance change across the MIT (figure 4.2). Films grown by this method have been shown to be granular [152]. Sheet resistance measurements were performed using a 4 point probe and a ceramic heating stage. The sheet resistance was measured to be 120 kΩ at 330 K, 16 kΩ at 342 K and 150 Ω at 360 K. Due to hysteresis, upward and downward switching temperatures were 350 K (T^{on}_{MIT}) and 345 K (T^{off}_{MIT}), characteristic of thin film VO_2 [153]. The wider hysteresis is evidence of a granular film of slightly mixed phase causing a percolative effect, while the high switching temperature suggests a slight oxygen excess as compared to single crystal VO_2 (figure 4.2) [106,154].

Devices for two-terminal measurements were prepared using photolithography as described in section 2.4. VO_2 channels of length 4 µm and width 8 µm were fabricated using a CF_4 reactive ion etch followed by deposition of layered Ti/Au contacts of thickness 5 nm/30 nm via electron beam evaporation. An image of the device can be seen in figure 4.3. Different devices displayed variations in threshold switching voltages and resistance due to variations in local film structure and lithography accuracy.

Contacting the samples was performed using a JANIS probe station with a heated stage. All measurements were made in the local ambient Dublin atmosphere. For electrical characterisation, input waveforms were created using the LeCroy ArbStudio 1102 arbitrary signal generator. A resistor (560 Ω) was placed in series with the selected VO_2 device and the Digilent Analog Discovery 2 oscilloscope was used to collect voltage data from the signal generator and across the resistor. The circuit is described in figure 4.3. This arrangement allowed a statistically relevant number of measurement to be taken quickly. Two different measurements were performed: first, a continuous sweep of the voltage up and down; and second, a pulsed sweep implemented with controlled pulse parameters, which will be explained in section 4.3. These measurements were performed on different devices.

4.2 Switching Voltage Change with Temperature

At stage temperatures below the transition temperature, the upward continuous sweeping I-V curve of the VO_2 device shows a discontinuity at a critical voltage (V_{sw}^{on}) as the material enters the metallic state and the current jumps. The closer the stage temperature is to the transition temperature, the less voltage is required (figure 4.4). As the voltage is lowered, the device will return to an insulating state at some V_{sw}^{off}. For a continuous voltage sweep, V_{sw}^{off} is always lower than V_{sw}^{on} resulting in a well-defined hysteresis.

This example shows that devices at higher temperatures require a lower electric-field before undergoing a MIT.

4.3 Switching Voltage Change with Pulsed Signals

In the pulsed experiments, voltage pulses 10 µs in length were applied with varying gaps between pulses ranging in time from 100 µs to 32 ns, at 0 V. The input waveform was generated by multiplying this pulsed wave with a triangular wave. The beginning of each pulse occurs at voltage intervals of 0.01 V (figure 4.5). The high and low resistance states of the VO_2 device were found to be between 10–15 kΩ and 60–260 kΩ respectively measured via the I-V curves. This variance is believed to be due to conduction filaments [155] within the VO_2 channels changing or rerouting as the experiment progressed.

Two measured quantities from the experiment are (i) the total voltage dropped

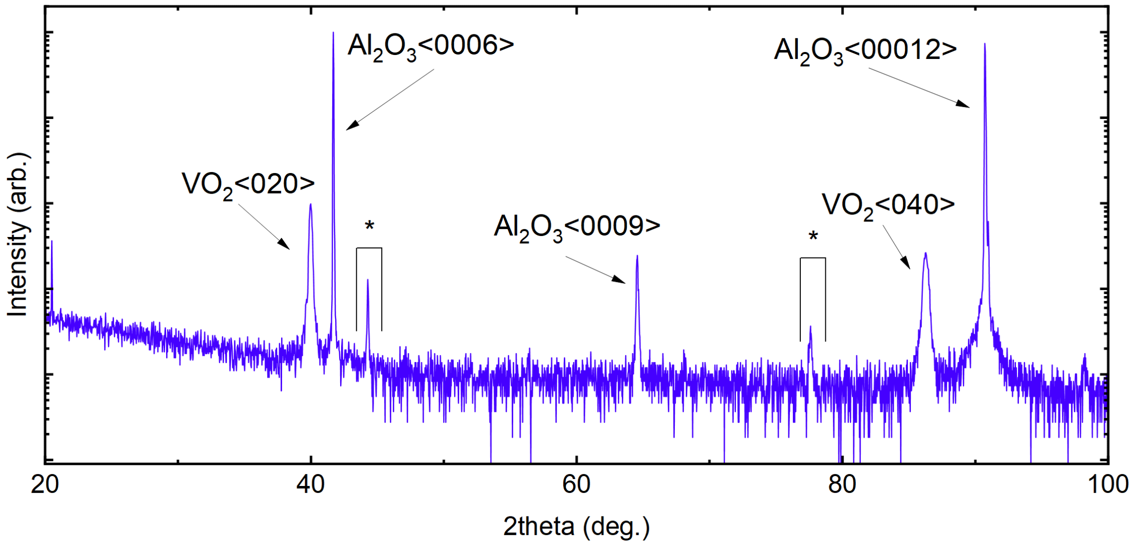

Figure 4.1: XRD measurement of the VO_2 sample showing the VO_2(010) and Al_2O_3(0001) refelections. The measurement points towards a textured VO_2 film. Background peaks generated by the diffractometer stage are depicted with (*).

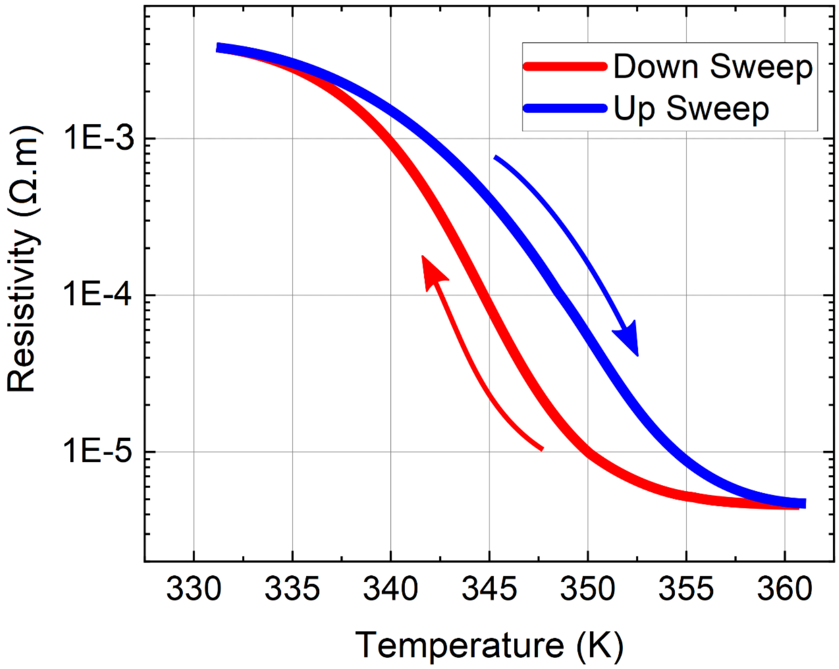

Figure 4.2: The temperature driven MIT of the VO_2 sample used. The slope, width and hysteresis of the transtion suggest a granular film of mixed stoichiometry. The slightly elevated switching temperature (point of maximum slope at 345 K and 350 K) suggests an oxygen excess in the film. Ideal switching temperature would be between 340–345 K

.

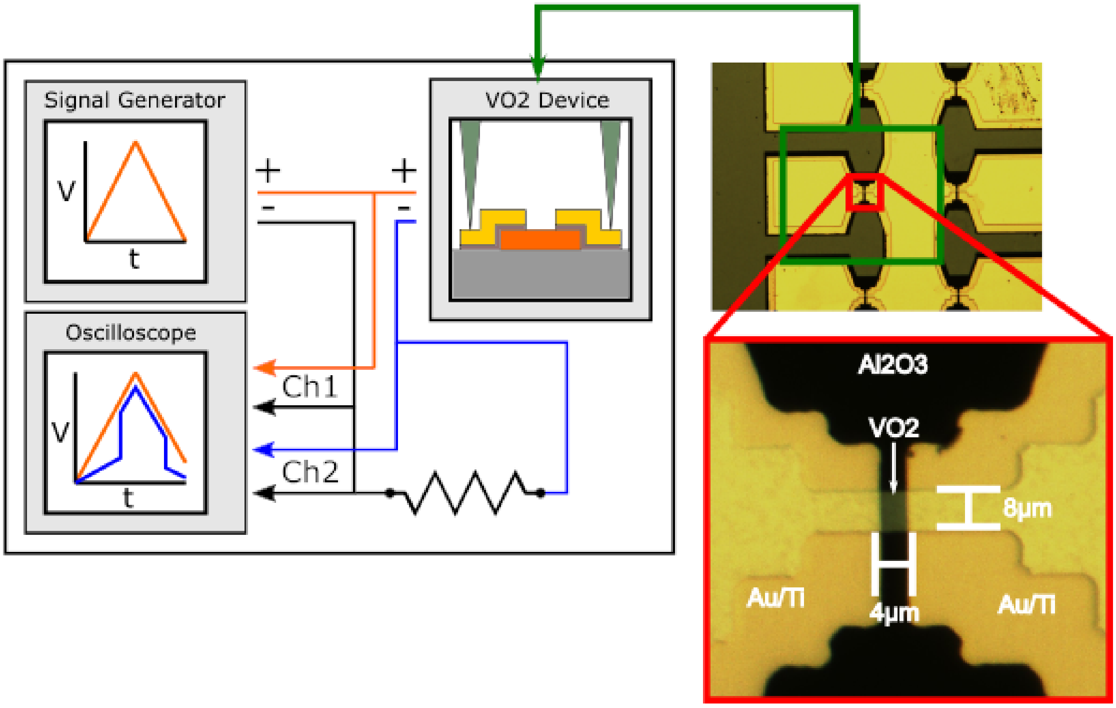

Figure 4.3: Schematic of the circuit used in this experiment. Inset on the right are images of the device used.

over the circuit (the source voltage, V_s) and (ii) the voltage drop over the resistor (V_R). The current through the circuit is calculated via $I = \frac{V_R}{R}$ where R is the resistance of the resistor, while the voltage drop across the device is defined as: $V_D = V_s - V_R$.

Figure 4.6 shows individual I-V measurements of the VO_2 device using V_D. This data is used to calculate the potential and power dissipated across the isolated VO_2 device. Figure 4.7 shows the relationship between the time gap, V_{sw}^{off} and V_{sw}^{on} for the VO_2 device (using V_D). 100 measurements were taken for each gap length. Each data point represents the average and standard deviation of these measurements. Measurements were taken with a stage temperature of 342 K. Two trends are clear from figure 4.7. First, V_{sw}^{on} slightly increases with increasing gap time. Second, V_{sw}^{off} increases, with increasing gap time. More importantly, ΔV (= $V_{sw}^{on} - V_{sw}^{off}$) decreases as the gap time increases.

In this system, it is demonstrated that both V_{sw}^{on} and V_{sw}^{off} are dictated by the self heating and cooling of the VO_2 channel device. This will be demonstrated qualitatively before a quantitative description using a simple model of channel temperature.

The sample begins at the set temperature (T_{set}: the stage temperature). In the continuously applied voltage regime, power I × V is applied to the channel, heating it. Any heat added will be conducted away by the channel, contacts and the highly

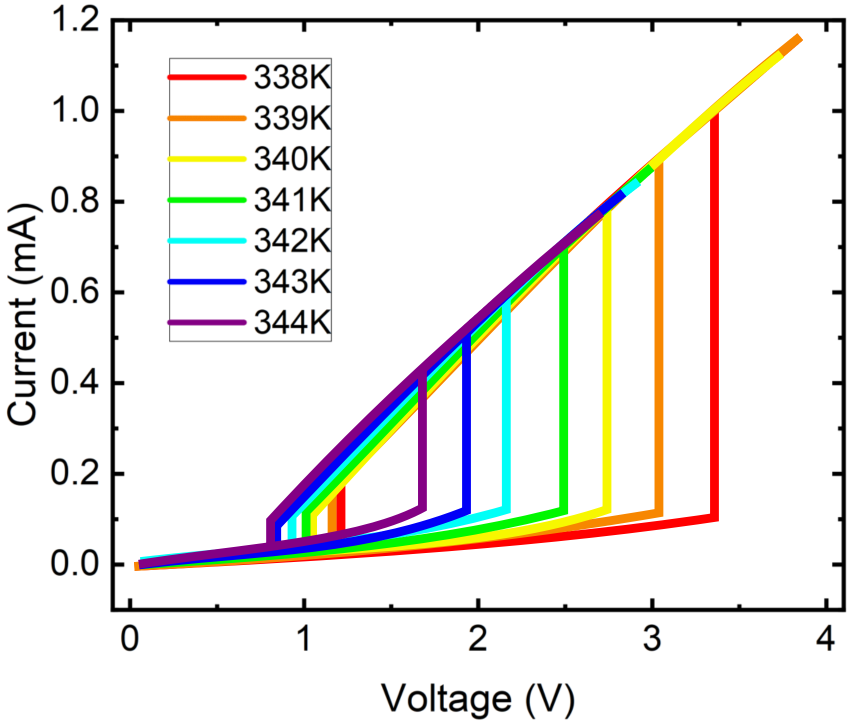

Figure 4.4: The IV curves of the VO_2 device at different temperatures under continuous voltage sweeping conditions. Voltage here is the drop across the entire circuit (V_s). It it clear that the switching voltage (V_{sw}^{on}) reduces with increasing temperature as expected for the Joule heating picture.

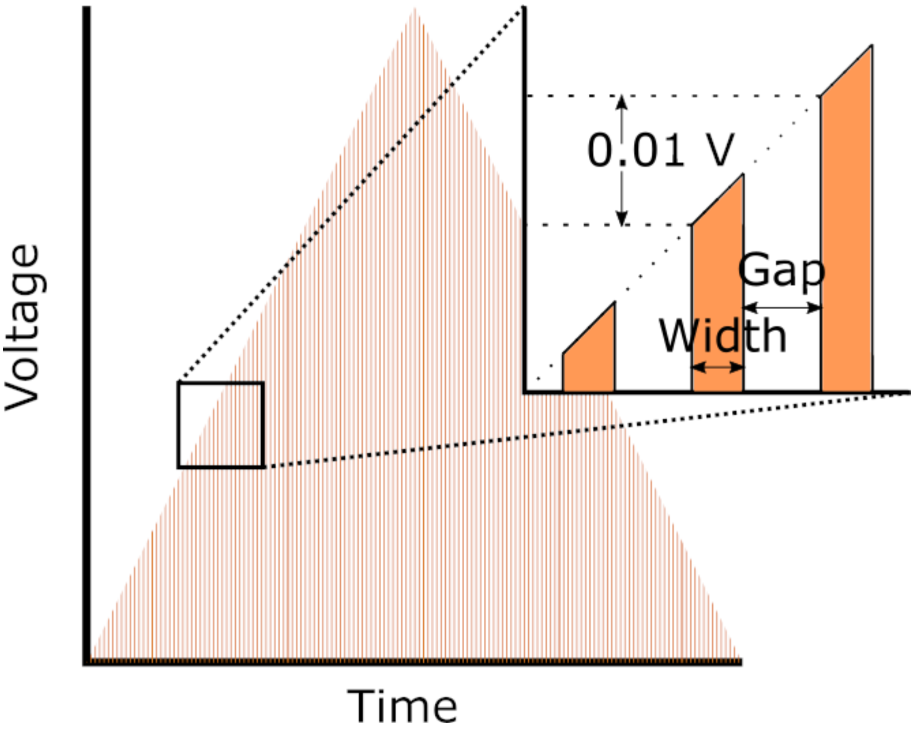

Figure 4.5: Diagram of input voltage signal for pulsed experiments. The voltage waveform is made up of pulses of increasing magnitude. Variations in the pulse time (time voltage is on) and gap time (time voltage is off) is variable.

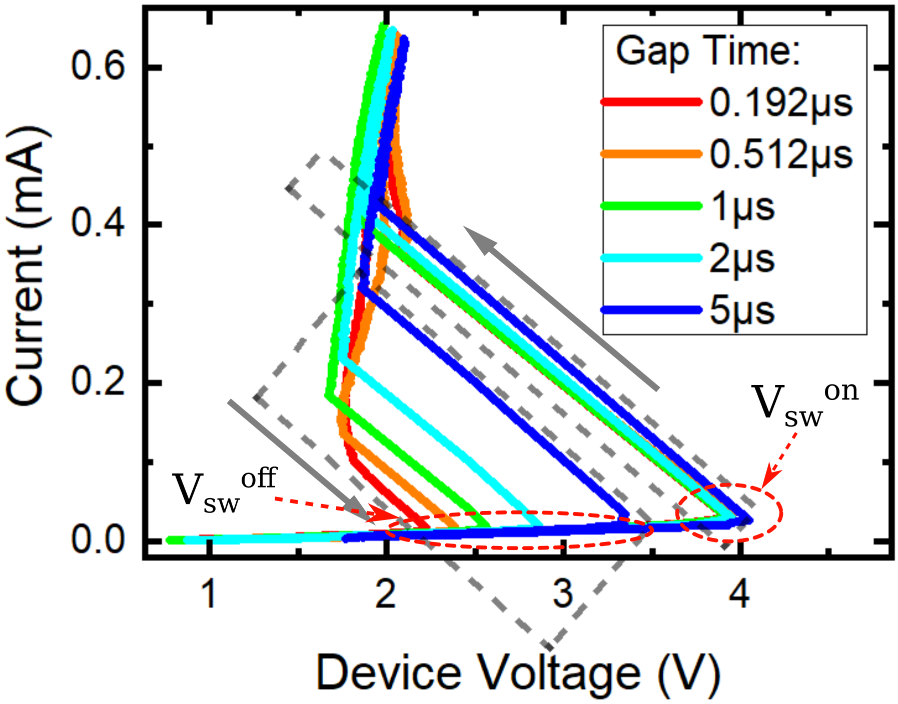

Figure 4.6: The IV curves of selected pulsed measurements using device voltage (V_D). Dashed boxes represent regions of V_{sw}^{On} and V_{sw}^{Off} for varying gap time. Values of V_{sw}^{On} and V_{sw}^{Off} taken at the bottom of the e-MIT switch. As gap time increases, V_{sw}^{On} slightly increases while V_{sw}^{Off} increases faster, reducing the hysteresis.

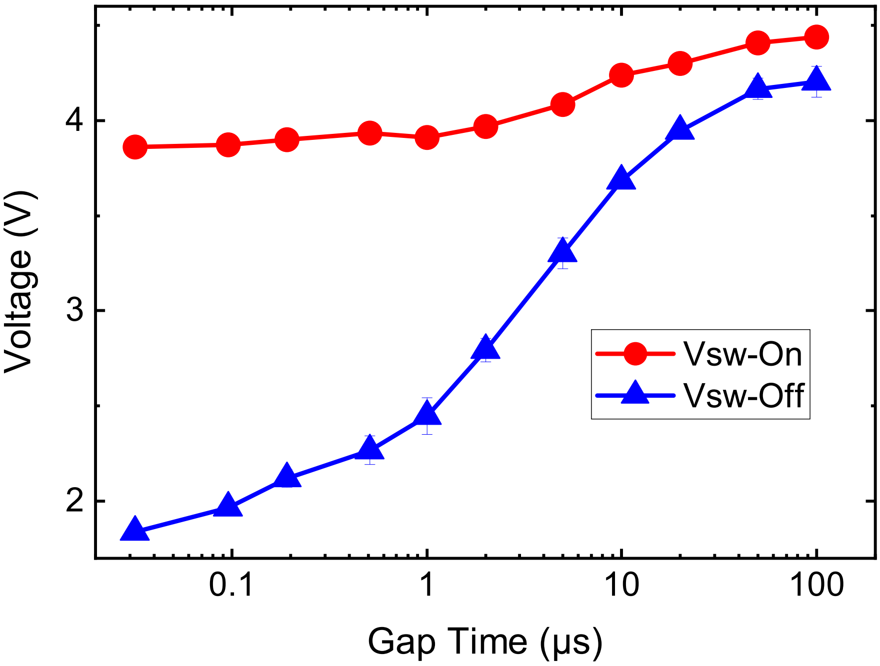

Figure 4.7: This graph illustrates the dependence of V_{sw}^{on} and V_{sw}^{off} on the gap time. The hysteresis of the device switching increases when the gap time is reduced.

thermally conductive sapphire substrate. [156] At V_{sw}^{on}, input power will be enough to bring the channel temperature (T_{ch}) to T_{MIT}^{on} (power = P_{on}). The resistance of the channel will drop and the current will increase. In this state the power applied is much higher, heating the channel. The channel will now stay in a metallic state until the applied power is low enough (P_{off}) to allow the channel to cool to T_{MIT}^{off}. Because the device is in a low resistance state, this will be at a much lower voltage (V_{sw}^{off}). Note, in this case $P_{on} \approx P_{off}$.

However, if a pulsed voltage is used, the channel is able to cool between consecutive pulses. Therefore, more power will be required to heat the channel to T_{MIT}^{on}, and for longer gaps the V_{sw}^{on} will increase as observed. Similarly, the device will switch back to an insulating state once T_{ch} reaches T_{MIT}^{off}. For a very large gap between pulses, this would occur at a voltage very close to V_{sw}^{on} as no heat would be retained in the channel between pulses. However as the gap decreases, ΔV will grow as heat is retained in the device, lowering the voltage required for T_{ch} to reach T_{MIT}^{off}. This will be the trend until the gap disappears and the system is in the continuous voltage regime again. Thus, the experimentally observed changes in switching voltage in relation to the gap between pulses (figure 4.7) is consistent with the heating picture.

4.4 Computational Modelling of Joule Heating Theory

As qualitatively described above, V_{sw}^{on} and V_{sw}^{off} are related to the current local temperature of the switching channel. To describe the movement of V_{sw}^{off} position in sweeps with different pulse parameters, a model is used to estimate the effective channel temperature as a function of applied electrical power. This model is used in a similar experiment by Fursina *et al* [29]. Detailed thermal modeling is very challenging due to the highly local character of the heating and difficulty of capturing all relevant heat transfer processes in these nano-structures. Instead a simple model where return to equilibrium is described by a relaxation time is used. This model is derived in section 2.3.1.

$$\begin{aligned} T(t+dt) = T_{set} + \frac{V \times I \times \tau}{C_v}\left[1 - exp\left(-\frac{dt}{\tau}\right)\right] \\ + \left[T(t) - T_{set}\right] exp\left(-\frac{dt}{\tau}\right) \end{aligned} \tag{4.1}$$

There are two fitting parameters in this model that predict the temperature; heat capacity C_v and relaxation time τ. Equation 4.1 was used in a python script to

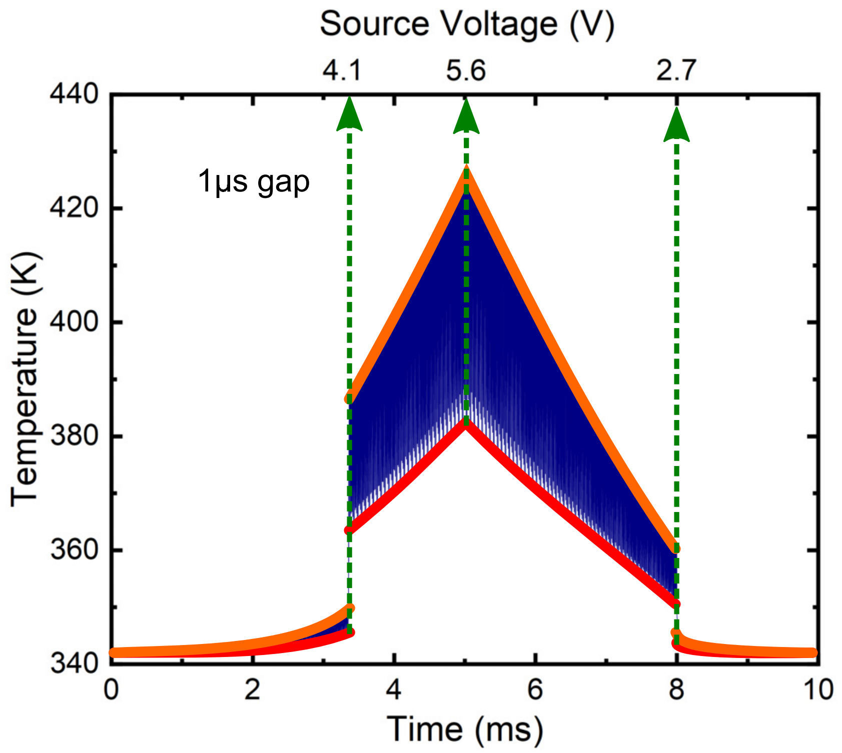

Figure 4.8: The heat simulation of the device with an input waveform from 0-5.6V, a pulse width of 10μs and a 1μs gap time. The dark blue area is the fluctuating temperature data. The orange and red line represent the temperature envelope, orange being the upper temperature profile, and red being the lower. Switching on occurs when the orange line hits T^{On}_{MIT} and off when the red line reaches T^{Off}_{MIT}.

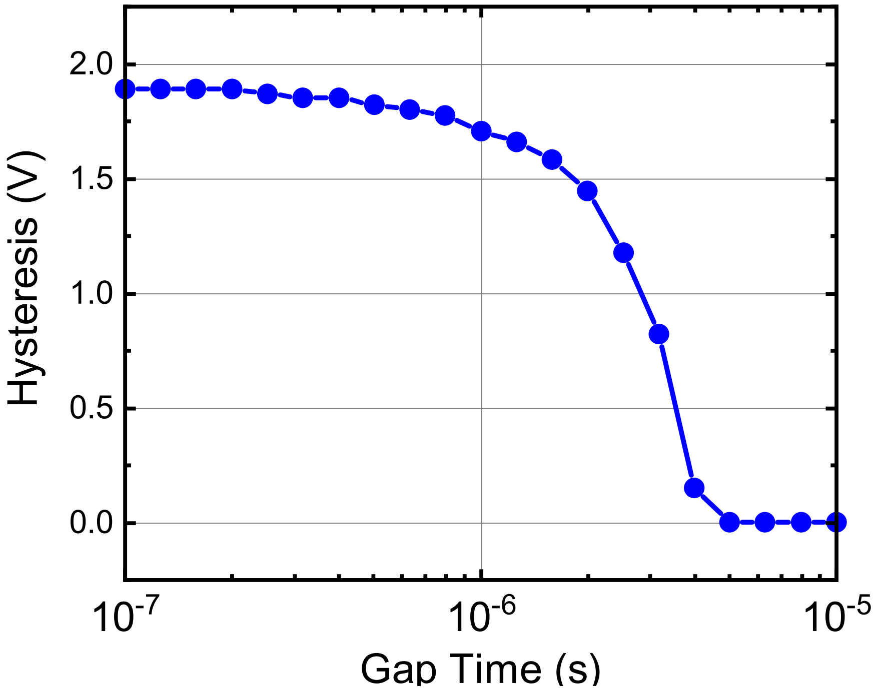

Figure 4.9: A simulation of hysteresis using the model above and a simplified input dataset.

model the channel temperature and calculate the fitting parameter values. V_D and I values for each time step were taken from the measured data. The fitting parameters were adjusted so that the temperatures reached at V_{sw}^{on} and V_{sw}^{off} corresponded to T_{MIT}^{on} and T_{MIT}^{off} respectively.

An example of the temperature calculated by eq. 4.1 is shown in figure 4.8. The orange line traces the maximum temperatures reached during pulses (voltage on), while the red line traces the minimum temperatures reached between pulses (voltage off). At V_{sw}^{on} the power jumps as the device becomes metallic and this leads to an increase in the temperature. The opposite occurs at V_{sw}^{off}. It is worth noting from figure 4.8 how erratically the channel temperature changes between pulses, rapidly heating and cooling while reaching a maximum temperature of 430 K. This is similar but lower in magnitude to temperatures calculated in similar experiments [157], with difference attributed to the lower powers used here. The adjusted optimum values of C_v and τ are $3.6 \times 10^{-11}\,\mathrm{J\,K^{-1}}$ and $1.8 \times 10^{-6}\,\mathrm{s}$ respectively. All pulse measurement simulations match V_{sw}^{on} and V_{sw}^{off} with respective temperatures T_{MIT}^{on} and T_{MIT}^{off} within 1 K.

Using the eq. 4.1 the voltage hysteresis was simulated as a function of gap length, and is depicted in figure 4.9. The dependence of the hysteresis magnitude on the gap time is reproduced, further illustrating the Joule heating mechanism and the role of the gap time in facilitating cooling and controlling the hysteresis magnitude. The change in the hysteresis is mostly due to the change in V_{sw}^{off}, in agreement with experiment.

This value of C_v can ideally be used to approximate the size of an isolated channel. The specific heat capacity C_v^s of VO_2 is 530–600 $\mathrm{J\,K^{-1}\,kg^{-1}}$. [158] Using the equation;

$$C_v^s = \frac{C_v}{m} = \frac{C_v}{\rho V} \tag{4.2}$$

and using the estimated heat capacity, a switching volume of $1.5 \times 10^{-17}\,\mathrm{m^3}$ is calculated. Given that the volume of the VO_2 channel is $9.6 \times 10^{-19}\,\mathrm{m^3}$, about 16 times smaller, it can be assumed that the substrate plays a substantial role in absorbing heat in this experiment, an expected result due to the high thermal conductivity of the Al_2O_3 substrate.

It should be noted that the entire volume of the VO_2 channel is assumed to switch in this model. This has been shown not to be the case in other experiments [111,159]. Due to this, the estimated heat capacity should be taken just as that, an estimate. That said, reducing the switching volume only increases the estimated heat capacity which maintains that there is some external heat absorption ongoing. Another assumption of this model is that C_v is independent of temperature which is not the case over large temperature ranges. Due to this, the higher temperatures calculated may not be accurate.

Despite these two assumptions, the model still works well in predicting the switching temperature and hysteresis magnitudes due to the fact that our stage temperature T_{set} (342 K) was held close to the MIT ($T^{off}_{MIT} = 345\,\mathrm{K}$). This environment allows for a reasonable expectation for the entire volume to switch and the temperature prediction to be accurate around the important values, the T^{on}_{MIT} and T^{off}_{MIT}.

Values in this section are given as absolute values with no error as these are the values that provided the closest fit to the data using this model. The nature of the calculation meant there was negligible error with the significant figures given. It is also noted that the values derived from these calculations are presented as estimates.

4.5 Discussion and Conclusion

In this experiment the applied field over the device never exceeds $1 \times 10^7\,\mathrm{V\,m^{-1}}$, lower than the field of $6.5 \times 10^7\,\mathrm{V\,m^{-1}}$ required to cause a purely electronically driven switch [4]. Because of this, it can be assumed that the dominant mechanism for the MIT is self-heating. Further evidence is seen by the shift to higher V^{on}_{sw} with increasing gap time (figure 4.7), as a higher power is required to heat the channel to T^{on}_{MIT}. A purely field driven switch (such as those seen in experiments with nanoscale channels [4]) would see a constant V^{on}_{sw} at the critical field. Despite this, it is maintained that even in channels which solely switch via electric field, this self-heating effect is still the mechanism behind their substantial hysteresis. For this reason, the temperature of VO_2 in the on state needs to be considered in the use of VO_2 electronics, and cooling methods to prevent the material from reaching unstable temperatures or use of voltage pulsing should be implemented to reduce final operating temperatures.

We have shown that the hysteretic behaviour seen in resistive switching of VO_2 thin films can be altered via pulsing. Increasing the gap time, or allowed cooling between pulses, raises the V^{off}_{sw} value, reducing hysteresis. This effect is shown to be thermal, agreeing with the work of Lee *et al* [157]. We have also shown that V^{on}_{sw} increases with increasing gap time, with the cooling adding to the power requirement. Increasing the period of the applied waveform, or the pulse width, would allow more heating at low voltages, decreasing V^{on}_{sw}. This agrees with the results of Lee *et al.* That work has also shown that by decreasing the resistive load in series with the device, V^{off}_{sw} and V^{on}_{sw} can be lowered without changing the hysteresis. From our model, this can be attributed to increasing the power applied to the channel, reducing the required voltage.

With this information a picture of tuning the RS curve of VO_2 can be built. V^{on}_{sw} may be raised or lowered by the period of applied voltage waveforms. The hysteresis of the device may be altered via pulsing of this waveform, and the magnitude of the switching voltages can be altered by changing the power applied to the channel.

Of course, this does not take into account the cooling effects of substrates or the intrinsic material properties of the VO_2 film itself. Our model shows the effect of substrate heat capacity plays a substantial role, while the effect of structural properties will change how the film reacts to changing temperatures and electric fields. Strict environmental temperature control will also be a requirement. However, this is proposed as a useful framework for engineering electronic devices using VO_2 films.

Finally the general applicability of our model may not be accurate outside the context of this experiment. Both assumptions made in this experiment, that the entire channel switches and that the heat capacity remains constant, rely on the fact that the sample is heated to close to it's MIT temperature. In this sense, I believe that we have done our best within this experiment to enable an environment where the model is accurate. Moving away from these conditions may require additional elements to be added to the model (a changing heat capacity for example), as our stated asumptions begin to break down. It should also be noted that we have not investigated the effect of pulsing in relation to devices with varying thickness or thermal environments due to experimental constraints. We also have not examined if different pulse shapes may be used to prolong the metallic MIT state using less power. It has been pointed out that these may be particularly interesting routes of future experimentation in relation to this work.

5

Low Electric Field VO_2 Type Resistive Switching Resulting from Reduced V_2O_5 Single Crystals

As discussed in Section 3.3.1 and Chapter 4, VO_2 exhibits a MIT, which can be triggered via electric field, referred to as resistive switching (RS), and is highly relevant for potential applications [9, 148]. VO_2 exhibits a purely electronically triggered RS when external electric fields of around $6.5 \times 10^7\,\mathrm{V\,m^{-1}}$ are applied across it [4]. VO_2 RS takes place at either voltage polarity [115]. Ideally, in electronic applications, heat fluctuations and power dissipation should be kept to a minimum to reduce energy consumption and mitigate adverse heating effects [148]. Reducing the necessary voltage to trigger RS and reducing power consumption of RS devices are two features attractive to application development. Other advantages include reducing the power surge at the transition point limiting additional heating, and therefore improving switching speed, and the low field can facilitate resistive switching at low temperatures.

As reviewed in Chapter 3 the vanadium-oxygen system is complex, consisting of several single valence phases (2+ to 5+) and mixed valence Magnéli (3+ and 4+) and Wadsley (4+ and 5+) phases. The VO phases produced by the thermal reduction of V_2O_5 depends on the reducing conditions [19, 134–137]. It is clear that reduction can proceed through a sequence of phases as outlined in section 3.6. The prominent phases reported are V_2O_3, VO_2(M)/(R), VO_2(B), V_6O_{13} and V_4O_9. Multiple phases can coexist during, and are stable after, the reduction process. These mixed phase compounds present opportunities for materials with combinations of potentially complementary properties from an application point of view.

This chapter presents annealing and reduction experiments on V_2O_5 single crystals resulting in a low resistance thin film with a MIT characteristic of VO_2 forming on the crystal surface. This film has an anomalously low electric field switching for a VO_2 type transition. First, an in depth study of V_2O_5 crystals annealed at different temperatures examines the changing composition of the switching layer, and how it relates to the MIT behaviour in this novel system. Second, a voltage-driven RS in select samples is induced by Joule heating. The RS is extremely stable and the electric field is phenomenally low at under $10^3\,\mathrm{V\,m^{-1}}$. This low electric field is due to low resistance of the VO_2(M) state, correlated to the inclusion of metallic mixed-valence phases in the surface region, as revealed and discussed in the first section. A short TEM section is also presented, confirming the presence of VO_2 and V_6O_{13} in an annealed V_2O_5 crystal.

5.1 Experimental Procedure

Unless specified, procedures were performed in TCD by myself or Dr. Brian Walls.

V_2O_5 crystals have been grown via floating zone technique (Materials Modeling and Development Laboratory) by Dr. Dmitry Shulyatev. The growth process was carried out in oxygen flow at a crystallization rate $8\,\mathrm{mm\,h^{-1}}$. The resulting crystals are between 1–2 cm long, and 1–5 mm in depth/width, and are irregular in shape. The crystals cleave easily *ex-situ* to reveal an optically flat surface.

To investigate the reduction process and the evolution of structural and electronic properties, four crystals were annealed at 600 K, 700 K, 800 K and 900 K in a vacuum tube at an atmosphere of approximately 1×10^{-4} Torr in intervals of 1–2 h. The furnace was placed over the vacuum tube when at the designated temperature. Sample temperature increased exponentially. It took approximately 5 minutes for the sample to heat to 90% of the annealing temperature, and 10 minutes to reach 100%. To cool, the furnace was taken off the vacuum tube, with no active cooling applied. The sample took approximately 30 minutes to cool to room temperature. These rates were established by placing a thermocouple in the place of the sample to characterise the heating and cooling rates. Electrical and x-ray diffraction measurements were performed before thermal treatment and after each annealing interval to investigate the evolution in conductivity and XRD patterns. Electrical measurements use a linear 4-point probe to extract a resistance and a sheet resistance.

To establish vanadium valencies present in this experiment, XPS measurements were performed by Dr. Ainur Zhussupbekova in TCD on different crystals from the same batch. The vanadium charge state of the pristine cleaved V_2O_5 was compared to that of a crystal annealed for 16 h at 800 K (the same sample used for RS measurements) in a vacuum pressure of 1×10^{-4} mbar within the vacuum tube annealing system.

To characterise voltage-driven MIT properties, electronic measurements voltage-current (VI) were performed on a cleaved crystal annealed in a vacuum pressure of 1×10^{-4} Torr at 800 K for 16 h. The VI measurements were performed in a narrow temperature window around the VO_2 transition temperature (340 K) in a rough vacuum pressure of 10 mbar using a four-point probe. The probes - in a linear arrangement - are separated by 2 mm. Current (I) is passed between the two outer probes, while the voltage (V) is measured between the two inner high impedance probes.

For the TEM investigation a different sample from the same as-grown crystal was annealed in the same conditions (1×10^{-4} Torr at 800 K for 16 h) prior to lamella preparation. The lamellae for TEM investigations were prepared on a VERSA 3D HighVac dual beam facility (FEI) using the Ga ion beam. Regular FIB lamella preparation was carried out at 30 kV and followed by 2 kV final step to improve the surface quality. TEM investigations were performed on a Titan 80-300 TEM. The sample thickness (70–80 nm) was less than the mean free path of the electron beam so the procedure of multiple inelastic scattering deconvolution was not performed. The intensity beyond the edge onset was integrated over a window of 70 eV to minimize the influence of the corresponding near-edge spacial fine structure. TEM was performed in the Institute of Solid State Physics, Chernogolovka, Russia, by Dr. Andre Mazilkin under direction from TCD.

Experiment design, data processing and analysis was performed in TCD. All measurements and data points presented are single, individual measurements. In section 5.4 VI measurements were repeated to verify the consistency of characteristics, but one single representative measurements are shown.

5.2 Verifying V_2O_5 Crystal Properties

First, the compositional and structural aspects of the as-grown V_2O_5 crystals was examined.

Measurements of the pristine cleaved crystal are depicted in figure 5.1. The θ - 2θ scan reveals sharp, pronounced $V_2O_5(010)$ peaks. Additional peaks are attributed to the sample stage. The reciprocal space map (RSM) of the $V_2O_5(010)$ peak is characteristic of a single crystal. The distribution in ω indicates there is a small angular distribution of crystallites about the surface normal. The sharpness in 2θ indicates the crystallites are large with a consistent lattice parameter. The lattice constant (4.354 Å) closely matches that of single crystalline V_2O_5 [160]. Asymmetric azimuthal ϕ-scans find 2-fold symmetry of the (110) plane, which is expected for the orthorhombic crystal. This measurements also resolves the [100] and [001] directions of the sample. XPS of a pristine sample shows only V^{5+} on the surface, analysed in detail in section 5.3.1.

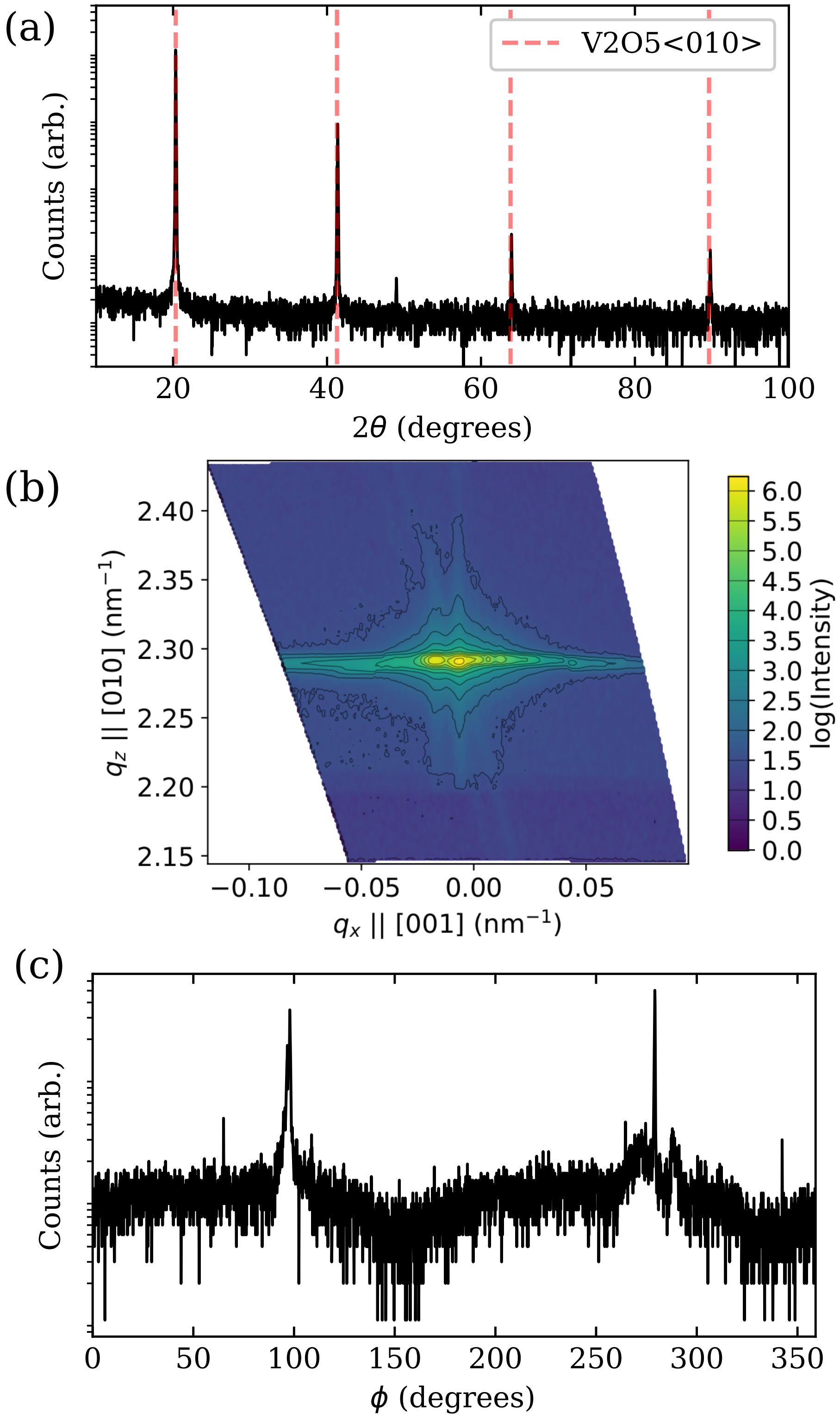

Figure 5.1: Measurements of the pristine V_2O_5 sample including: (a) XRD scans showing only $V_2O_5(010)$ reflections; (b) RSM showing a sharp signal characteristic of a highly crystaline sample; (c) ϕ-scan revealing two reflections of the (110) in-plane surface.

It is concluded that the sample is single crystalline V_2O_5 with a (010) surface.

5.3 Characterisation of Reduced V_2O_5 Crystals

Reducing the V_2O_5 crystals leads to drastically evolving structural and electronic properties due to compositional changes. In this section, the evolution of the crystals is experimentally analysed.

Due to the multitude of phases, there are a vast amount of vanadium oxide reflections. In addition, the crystal structure of some of these phases is not well understood, certainly related to the difficulty in synthesising mixed valance phases as an isolated crystalline product. The focus is put on those phases which can be understood in terms of simple reduction mechanisms and are reported in the literature, as well as evidence collected via XPS measurements (section 5.2). These correspond to the phases discussed in Chapter 3: V_2O_5, V_4O_9, V_6O_{13}, VO_2(B) and VO_2(M)/(R).

5.3.1 XPS

To study the composition of the crystals, XPS was performed. The explicit purpose of XPS in this study was to discern possible vanadium oxide phases; *i.e.* to establish what valences of vanadium are present. The only elements contributing to the XPS spectra outlined below were oxygen and vanadium, as well as evidence for contamination from carbon which is normal for ex-situ XPS measurements.

The XPS spectra and fits of an ex-situ cleaved V_2O_5 crystal and a crystal annealed ex-situ for 16 h in vacuum at 800 K are shown in figure 5.2. Shown here are the O1s and V2p regions at binding energy 540–510 eV. The vanadium V2p orbital gives a pair of peaks, $V2p_{3/2}$ and $V2p_{1/2}$. Both samples exhibit a O1s region which can be de-convoluted as into the dominant peak of lattice oxygen and a peak at higher binding energy corresponding to oxygen vacancies created upon annealing, as has been observed in other metal oxides [161]. This peak may also correspond to hydroxide contamination on the surface, as both samples are exposed to an ambient environment. The spectra are aligned to the O1s lattice oxygen component at 530 eV [162, 163]. The annealed sample was prepared in the same annealing furnace as all other samples in this experiment giving a direct comparison.

In the freshly cleaved crystal, the only one V2p contribution is identified as V^{5+} at 517.0 eV compared to 517.2 eV in literature [163] (figure 5.1).

After the 16 h *ex-situ* anneal, the V2p region is fit with 5+ (517.0 eV) and 4+ (515.9 eV) contributions. Literature gives these values at 517.0 eV for 5+, and 515.95 eV for 4+ [163].

Based on these findings, the pristine V_2O_5 surface has only V^{5+} present, confirming its single phase quality. Samples annealed for under 16h can be assumed to be composed of metal oxide phases with only V^{5+} and V^{4+} valence states present, ruling out the presence of Magnelli phases with V(III) contributions and V_2O_3. This assumption is extended to all of the following results.

5.3.2 X-Ray Diffraction

To investigate the structural evolution of the crystals, ex-situ XRD was used. Crystals were annealed at 600, 700, 800 and 900 K. Initial measurements indicated these temperatures show significantly different reductions, and hence provides a good examination of reduction as a function of temperature. The highest temperature, 900 K is close to the melting point of V_2O_5 (960 K). Not all of the spectra are presented, only those which showed significant changes compared to the previous step. The crystals were annealed at temperature for 20 minutes initially and subsequently in steps of one or two hours. The first anneal was short in an attempt to capture the initial reduction. The stated time is the cumulative time of annealing.

The evolution of the XRD at the annealing temperature of 600 K is straight forward with the only additional peaks introduced attributed to V_4O_9(001) at 43° [164]. XRD spectra after a total annealing time of 20 min, 6 h and 22 h are depicted in figure 5.3(a).

After 2 h of annealing at 700 K the XRD spectra is already complex (figure 5.3(b)); the most prominent peaks are attributed to V_4O_9(001) and unusually broad and shifted V_6O_{13}(001) peaks while smaller peaks are attributed to V_6O_{13}(010) [125]. A broad prominent peak centered at 27.5° sits between the overlapping V_6O_{13}(003) and VO_2(110) peak at 26.8° and VO_2(B)(002) at 28.9°. After 4 h of annealing, the broad peaks split and consolidate into V_6O_{13}(001) and VO_2(B)(001) peaks. The V_6O_{13}(010) peak grows in intensity. Further annealing results V_6O_{13}(001) and VO_2(B) becoming larger, narrower and shifting towards value expected in literature. In addition the intensity of V_4O_9 peaks decrease. V_6O_{13} and VO_2(B) are consecutive epitaxial phases in the V_2O_5–VO_2(B) reduction pathway (section 3.6). The evolution of the XRD pattern suggests a gradual spatial transition from one phase to the next in early anneals, as opposed to an acute phase boundary.

At this point it is noted that due to V_6O_{13}(001)'s lattice constant (10.14 Å) being close to triple the length of VO_2(M)(110)'s (3.3 Å), there are V_6O_{13}(001) peaks which overlap with VO_2(110) peak (eg.(003),(006)), but also peaks that do not (eg.(002),(004),(005)). From the presence of these, I can conclude that V_6O_{13} is present. The resistance measurements, depicted and discussed below, illustrate that VO_2 is also present. The larger intensity of each potentially overlapping

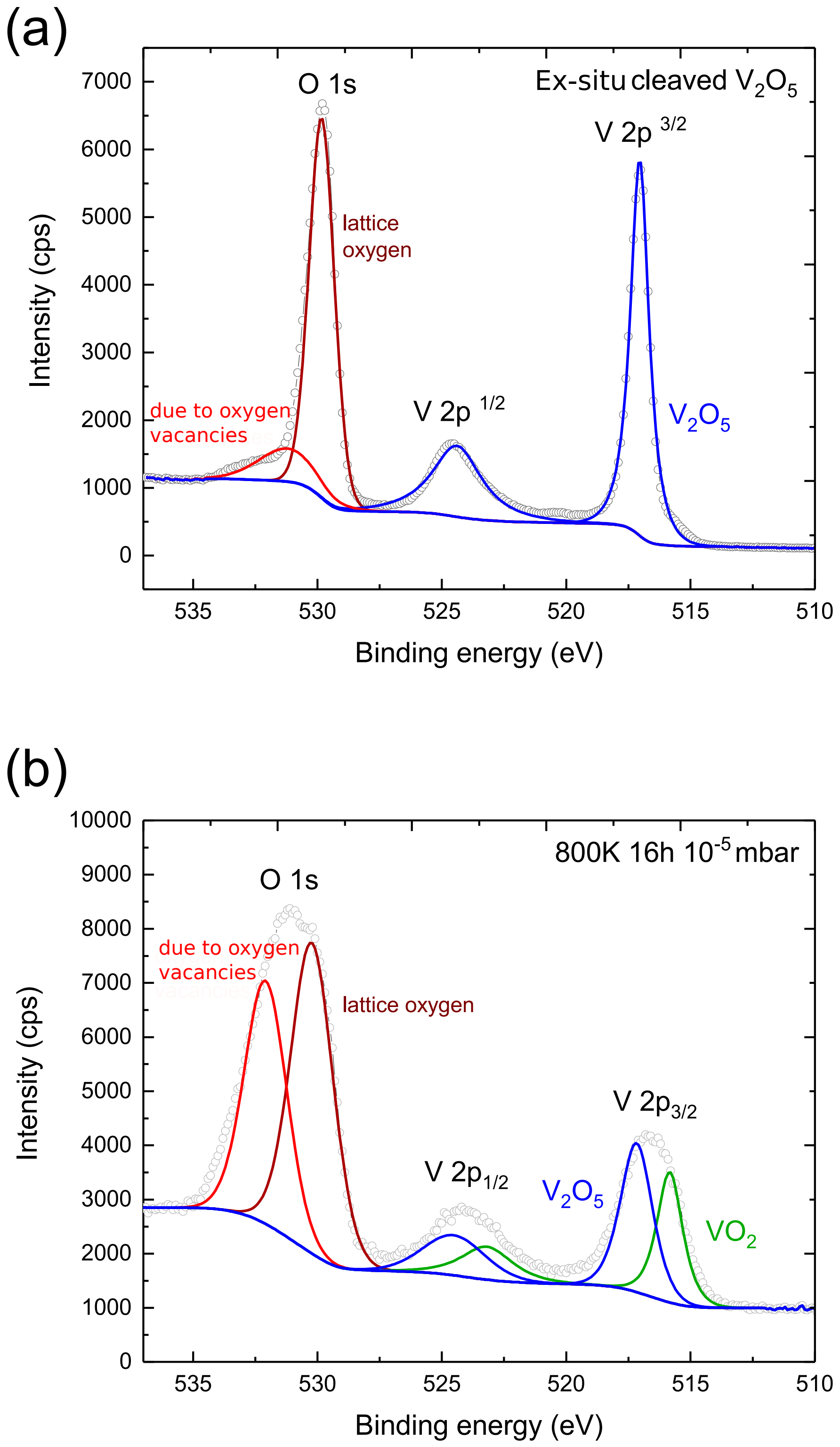

Figure 5.2: XPS spectrum of the V_2O_5 sample annealed for 16 hours under vacuum. There are contributions from oxygen deficient material with a high number of oxygen vacancies, lattice oxygen and vanadium 4+ and 5+ states.

$V_6O_{13}(001)/VO_2(110)$ feature aligns with this assumption.

The initial 20 minute anneal at 800 K results in $V_6O_{13}(001)$ and $V_4O_9(001)$ peaks and a low intensity $V_6O_{13}(010)$ peak (figure 5.3(c)). An additional hour of annealing removes the peaks attributed to V_4O_9. After 5 h the XRD is dominated by $V_6O_{13}(001)$. A small $VO_2(011)$ contribution is observed and $VO_2(110)$ peaks overlapping with $V_6O_{13}(001)$ are not ruled out. Further annealing results in both $VO_2(B)(001)$ and $V_6O_{13}(100)$ peaks. Finally, the $V_6O_{13}(010)$ peak is considerably larger. Continued annealing - up to 30 h - does not introduced significant changes. After this substantial time of annealing there are several unassigned peaks, none of which can be understood in terms of the reflections discussed thus far informed by the reduction mechanisms discussed in the section 3.6. One could attempt to assign the peaks to the vast amount of VO reflections, but without an informed rationale one can have little confidence. It is suggested that the continued annealing reduces the crystallinity, which can give rise to various different orientations. Additional phases beyond those discussed thus far are not ruled out.

The progression of the crystal annealed at 900 K is relatively straight forward (figure 5.3(d)); $V_6O_{13}(001)$ dominates after the initial short duration anneal and after several hours of annealing where the system finds an equilibrium. After 1 h of annealing the only peaks introduced are $VO_2(B)(001)$. After 3 h, a small peak attributed to $VO_2(011)$ is introduced. No relevant changes are observed with further annealing.

Table 5.1 estimates the contribution of the phases to each of the crystals once the XRD pattern has reached an equilibrium. W, M and S corresponds to weak, medium and strong, respectively. P denotes present, as assigning contribution to the overlapping $VO_2(M)$ peaks is difficult. The strength attribution is qualitatively assigned based on the intensity of the XRD peaks and does not take into account reflex strength or the possibility of amorphous phases. Nonetheless trends are observed:

- At low temperatures V_4O_9 dominates and is not observed at 800 K or higher.
- V_6O_{13} dominates at high temperatures and is not observed at 600 K.
- $V_6O_{13}(010)$ is observed at the middle temperatures of 700 K and 800 K
- The vanadium dioxide reflections are weak or obscured, and are observed at 700 K upwards.

These observations are supported by the literature; V_4O_9 has been reported to form at low temperature of 400 °C or less [137, 165, 166]. The observation of $V_4O_9(001)$ at low energies and as an initial product at 800 K is unsurprising due to the combination of i) not requiring a shear operation which rearranges the oxygen polyhedral and ii) large channels in the $V_2O_5[010]$ ($V_4O_9[001]$) direction allowing facile migration of

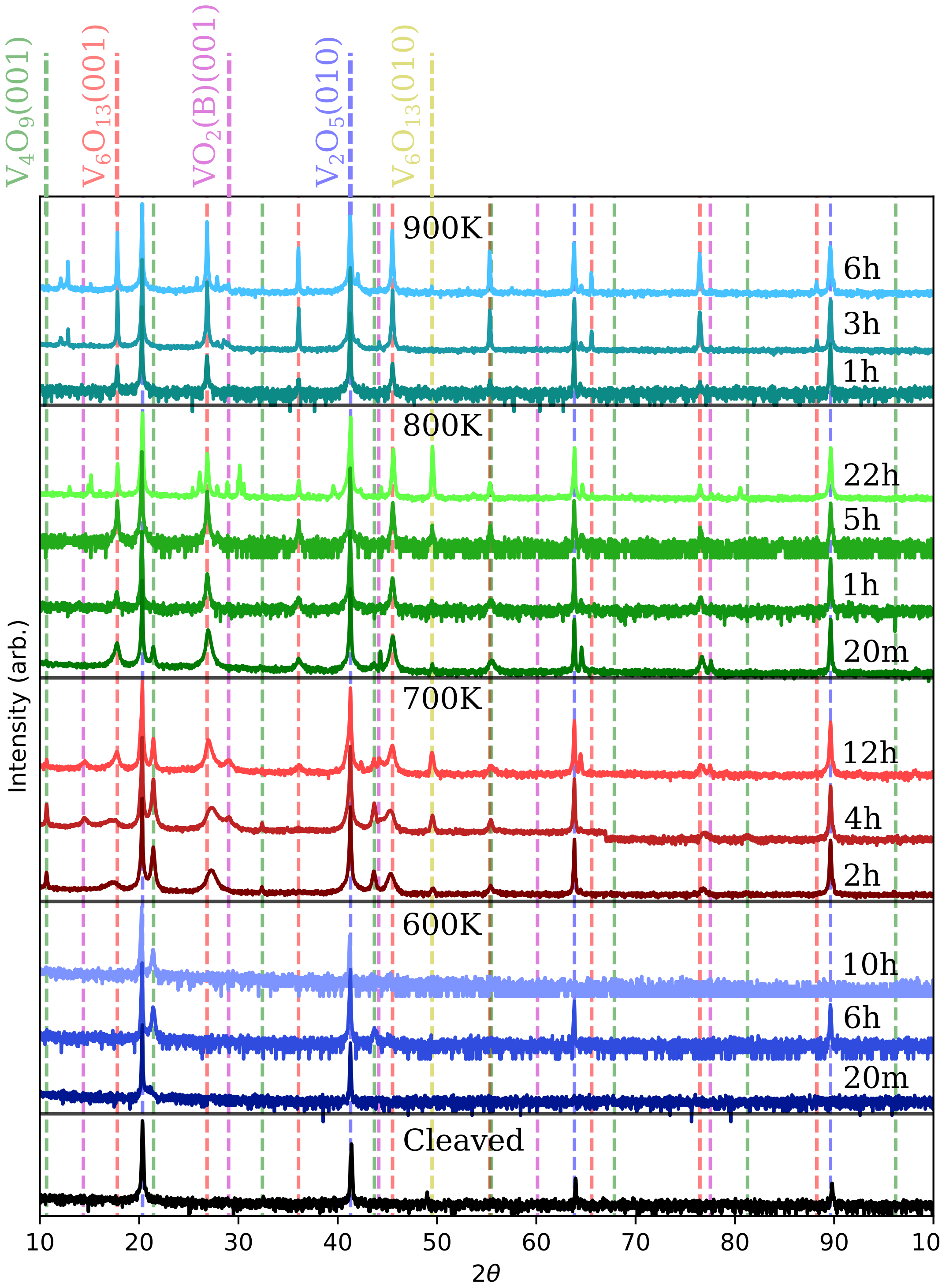

Figure 5.3: XRD data of the four samples annealed at: 600 K, 700 K, 800 K, 900 K. Only time intervals where significant change is seen are presented. Phases identified are labeled on the top of the graph.

	V_2O_5	V_4O_9	V_6O_{13}	VO_2(B)	VO_2(M)	Resistance	VO_2
600 K	S	S	-	-	-	7–3 kΩ	-
700 K	S	M	M	W	P	4000–150 Ω	✓
800 K	S	-	S	W	P	4000–300 Ω	✓
900 K	S	-	S	W	P	250–50 Ω	-

Table 5.1: Table identifying phases present in the annealed samples as identified via XRD, as well as sample resistance and if a VO_2 type MIT is visible. W, M and S correspond to weak, medium and strong repectively. P denotes present, due to difficulty assigning contribution intensity.

oxygen generating the vacancies. At higher annealing temperatures in the range of 800–1000 K, V_6O_{13} has been produced from V_2O_5 [167, 168].

In-plane XRD data shows that V_2O_5[001], V_6O_{13}[001] and VO_2(B)[001] are parallel in plane, and that the reduced phases of V_2O_5 remains epitaxial when transforming to these phases. This is an expected relationship due to the structural similarities of these phases as outlined in Chapter 3. This data is presented and examined in depth in Chapter 6 as the structural relationship is more relevant there.

5.3.3 Electrical Properties

Different VO phases exhibit different resistive properties as well as characteristic MITs. By studying the evolution of electronic resistance measurements, further information about the crystal composition is extracted in this section.

The resistance of the crystal annealed at 600 K, composed of V_2O_5 and V_4O_9 is comparable to pristine V_2O_5 (figure 5.4(a)). To the best of my knowledge there are no reports of the resistivity of V_4O_9. Benkahoul *et al.* grow films of mixed V_2O_5 and V_4O_9 which gave a resistivity of 0.01 Ω m [139], approximately 2-3 orders of magnitude lower than V_2O_5, but still considerably higher than other VO phases. See table 3.1 for more details. Due to very little change seen in the resistance of the sample structure, its assumed that either the V_4O_9 content is very small, or that the resistivity of V_4O_9 is comparable to V_2O_5.

After a total of 4 h of annealing at 700 K the VO_2(M)/(R) transition is apparent albeit broad and small (figure 5.4(b)). Continued annealing reduces the resistance while increasing the resistance change at the VO_2(M)/(R) transition and reducing its width. The resistance progression in the case of annealing at 800 K is more complex (figure 5.4); Similar to 700 K, a broad and small VO_2(M)/(R) transition is present although in comparison, the resistance is lower over the entire temperature range. Continued annealing shifts the overall resistance down. After 12 h the transition decreases in width and increases in magnitude. Continued annealing increases the magnitude of the transition for both samples. The increased and decreased resistance below and above the VO_2(M)/(R) transition temperature, respectively, is consistent with an increased percentage of VO_2(M)/(R) in the crystal's surface region. the narrowing of the transition suggests improved crystal quality of the VO_2 present.

The resistance of the crystals annealed at 700 K(1000–50 Ω) and 800 K(1000–100 Ω) is considerable lower than that observed for VO_2(M) thin films (∼30 kΩ) [3]. Other phases identified by XRD are Wadsley phases V_4O_9 and V_6O_{13}. Only V_6O_{13} - which can be seen in the XRD - is metallic over this experiment temperature range, and is suggested to give rise to the low resistance of these crystals. The low resistance of these sample is therfore attributed to the presence of V_6O_{13}.

The resistance of the crystal annealed at 900 K for 4 h, ranges from 250–50 Ω at 320–420 K, a resistance comparable to anneals at 700 K and 800 K. No MIT is visible. Its evolution in terms of resistance is shown in figure 5.4(d). The low resistance in comparison to 700 K and 800 K annealed samples indicates the V_6O_{13} dominates, as XRD suggests. VO_2 is likely present in only a small volume.

5.3.4 Summary

XPS measurements (section 5.2) show the existence of only V^{5+} and V^{4+} in the samples, so VO phases with V^{3+} are not considered in this investigation.

Annealing at 600 K promoted only a V_4O_9 structure. The crystal maintained a high resistance and showed no VO_2 type MIT (MIT_{VO2}). The 700 K anneal gives rise to evidence of four new phases in the XRD: V_4O_9, V_6O_{13}, VO_2(B) and VO_2(M). The resistance of this crystal is greatly reduced to 4000–150 Ω even after short initial anneals, and a MIT_{VO2} is visible. Annealing at 800 K sees no contribution from V_4O_9 in the XRD but the other phases are present. The resistance of the crystal is also lowered (4000–300 Ω), and a MIT_{VO2} is evident. The 900 K promotes mainly V_6O_{13}, with no evidence of a MIT_{VO2} despite weak VO_2(M) XRD patterns emerging.

The MIT_{VO2}, visible in 800 K and 700 K samples, increases in magnitude and narrows in width with increased annealing. This suggests an increased amount of VO_2 and a increase in crystal quality.

Based on the high resistance of the sample annealed at 600 K, I suggest the resistance of V_4O_9 is high, and comparable to V_2O_5. V_6O_{13} is the only phase present with a documented low resistivity at the measurement temperatures of the experiment. I therefore attribute the low resistance of the samples annealed at 700, 800 and 900 K to the presence of this phase.

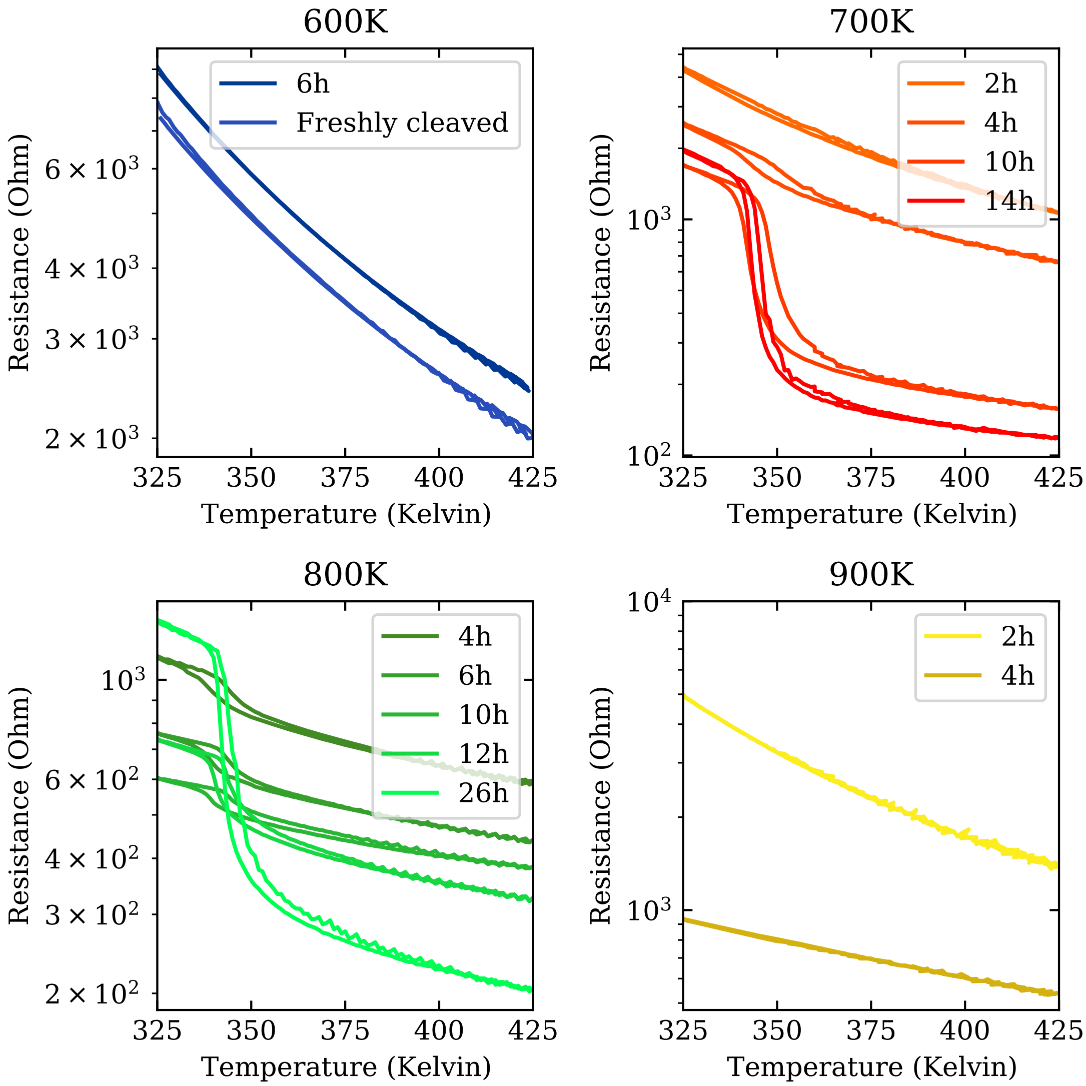

Figure 5.4: Resistance vs temperaure plots for V_2O_5 crystals annealed at: 600 K, 700 K, 800 K, 900 K. Only time intervals where significant change is seen are presented.

5.4 Resistive Switching

RS measurements have been performed on a crystal which exhibited i) a large resistance change around the MIT of VO_2(M)/(R) and ii) low resistance in both phases. Based on measurements in 5.3, which show a distinct and low resistance MIT after annealing at 800 K, a V_2O_5 crystal was annealed in vacuum at 800 K for 16 h continuously.

This annealed V_2O_5 crystal is shown to have a RS at anomalously low applied fields of 425 V m^{-1}.

5.4.1 Characterisation of Switching Crystal Surface

In order to establish the composition and crystal characteristics, XRD, RT and XPS measurements were carried out and are examined.

Figure 5.5(b) depicts the resistance in the temperature range 320–420 K. The temperature has been ramped up and subsequently down. There is a clear drop in the resistance characteristic of the VO_2 MIT. This transition, centered at 342 K sees a reduction in the resistance by a factor of 20 across $\sim$5 K. A thermal hysteresis of 2 K is present.

The VO_2 presented here is concluded to be close to stoichiometric due to the narrow and distinct transition at the predicted VO_2 MIT temperature. The relatively small change in resistance at the transition is due to the low resistance at low temperatures.

XRD analysis (figure 5.5(a)) of the sample shows V_2O_5(010), VO_2(110) and (011), V_6O_{13}(001), (102) and (010) and V_4O_9(001). It is well established that the reduction of V_2O_5 can result in V_6O_{13} with V_2O_5[010] and V_6O_{13}[001] aligned. A pathway to produce (102) oriented V_6O_{13} cannot be easily understood. Nevertheless (204) and (408) peaks are observed. The annealing conditions used for this sample are the same as those for the 800 K sample in section 5.3. While the previous sample was annealed in 2 hour steps and with exposure to atmosphere between steps, this sample was annealed continuously. This results in some changes. In comparison to the sample annealed at 800 K in section 5.3, this crystal exhibits V_4O_9, does not exhibit VO_2(B) and the orientations of V_6O_{13} differ.

The VO_2(011) and V_2O_5(010) peaks have been examined in detail. The reciprocal space maps (RSM) of the V_2O_5(010) and VO_2(011) peaks are presented in figure 5.5(c). Modification of the V_2O_5(010) region is evident; the RSM is characterised by two peaks and a homogeneous component. The peaks correspond to 4.415 Å and 4.409 Å while the homogeneous band corresponds to 4.388 Å. All of these values are greater than the bulk lattice constant. This is in agreement with the work of Monfort *et al.* who observed a shift of the V_2O_5(010) diffraction peak to smaller angles and the simultaneous formation of VO_2 and V_4O_9 after vacuum annealing a V_2O_5 thin film [137]. The intensity of the VO_2(011) peak is homogeneous within the probed angular window indicating the VO_2 is polycrystalline. The (011) inter-planar distance of 3.22 Å is slightly smaller than the bulk value of 3.27 Å.

In figure 5.5(c) the width of the reflexes in the 2θ direction are analysed. The width can be due to variation in the lattice constant and/or coherent domain size correlated to grain size. Applying the FWHM of the VO_2(011) reflex to the Scherrer equation give an average coherent domain size of 47 nm. If I interpret the width to be due to variation of the lattice constant I obtain a maximum deviation from

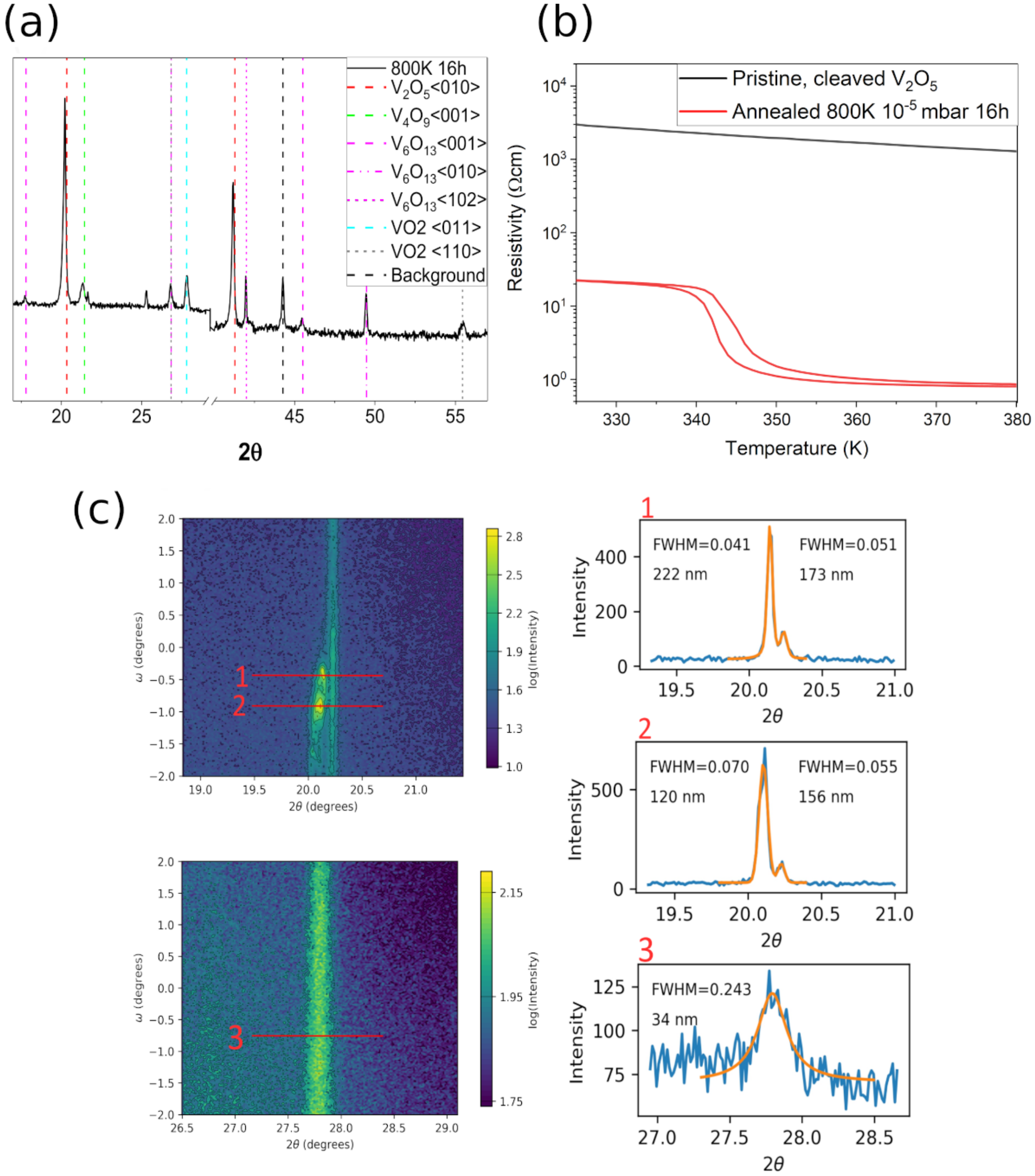

Figure 5.5: (a) XRD, (b) resistivity vs temperature and (c) RSM and peak width analysis of the V_2O_5 sample annealed for 16 hours in vacuum.

the bulk value of 0.3 Å, or 1%. However, strain is known to substantially alter the metal-insulator transition temperature: Cao *et al.* demonstrate a 15 K shift per percent strain. Considering an abrupt MIT is measured at 342 K (figure 5.5(b)) compared to the ideal switching temperature of 340 K (section 3.3.1) variation in the lattice constant is excluded. The $V_2O_5(010)$ reflex of the annealed crystal gives a coherent domain size of 100–150 nm. In the case of the pristine crystal the $V_2O_5(010)$ reflex is too sharp for the Scherrer equation to be accurately applied as a very large uncertainty in grain size would result; indicative of very large grains of a single crystal.

XPS findings of this sample are presented in section 5.2. The conclusion of these findings is that only phases containing 4+ or 5+ vanadium valences contribute to the composition of this crystal.

5.4.2 The Role of Joule Heating in Resistive Switching

VI measurements are depicted in figure 5.6. The temperature of the stage is set (T_S) and has been varied between 337 and 343 K in one Kelvin steps. The voltage is swept from $0 \rightarrow 1\,\mathrm{V} \rightarrow 0 \rightarrow \text{-}1\,\mathrm{V} \rightarrow 0$ in steps of 0.01 V. The Keithley 2400 used as a source and multimeter is set to "auto-delay", therefore 1 ms is the delay between measured data points. Voltage is measured by the two inner probes, while current is driven from the outer probes. Each curve shown is a single sweep. In this voltage range RS is observed for T_S of 339 K and greater. At the switching threshold voltage (V_{th}) the current abruptly increases as the VO_2 transitions to the metallic phase. V_{th} decreases as the T_S approaches the T_{MIT} of VO_2. Considering the electric field in this experiment - $500\,\mathrm{V\,m^{-1}}$ at 1 V (1 V/2 mm - it is clear the RS can not be due to purely electric field driven effects: a field of over $6 \times 10^7\,\mathrm{V\,m^{-1}}$ is required [168]. Within the Joule heating picture the power induces heating, some of which is conducted away. If the VO_2's (or a channel therein) temperature surpasses the MIT temperature it will switch to the metallic phase. Once the material is metallic, the current and power will spike and cause a further increase in temperature within the rutile volume, which carries the majority of the current. The net heat added to the system is [109, 111]:

$$\frac{\mathrm{d}Q}{\mathrm{d}t} = \frac{V^2}{R} - k(T_C - T_S) \tag{5.1}$$

V is the voltage drop across 2 mm (spacing of point probes) of $VO_2(M)$ with a resistance R. T_C, T_S and k_{eff} are the crystal (or channel) temperature, set or stage temperature and the effective thermal conductance. If one assumes a steady state, the square of the voltage is proportional to the temperature difference between the channel and the rest of the system. When $V = V_{th}$, $T_C = \mathrm{T}_{MIT}$:

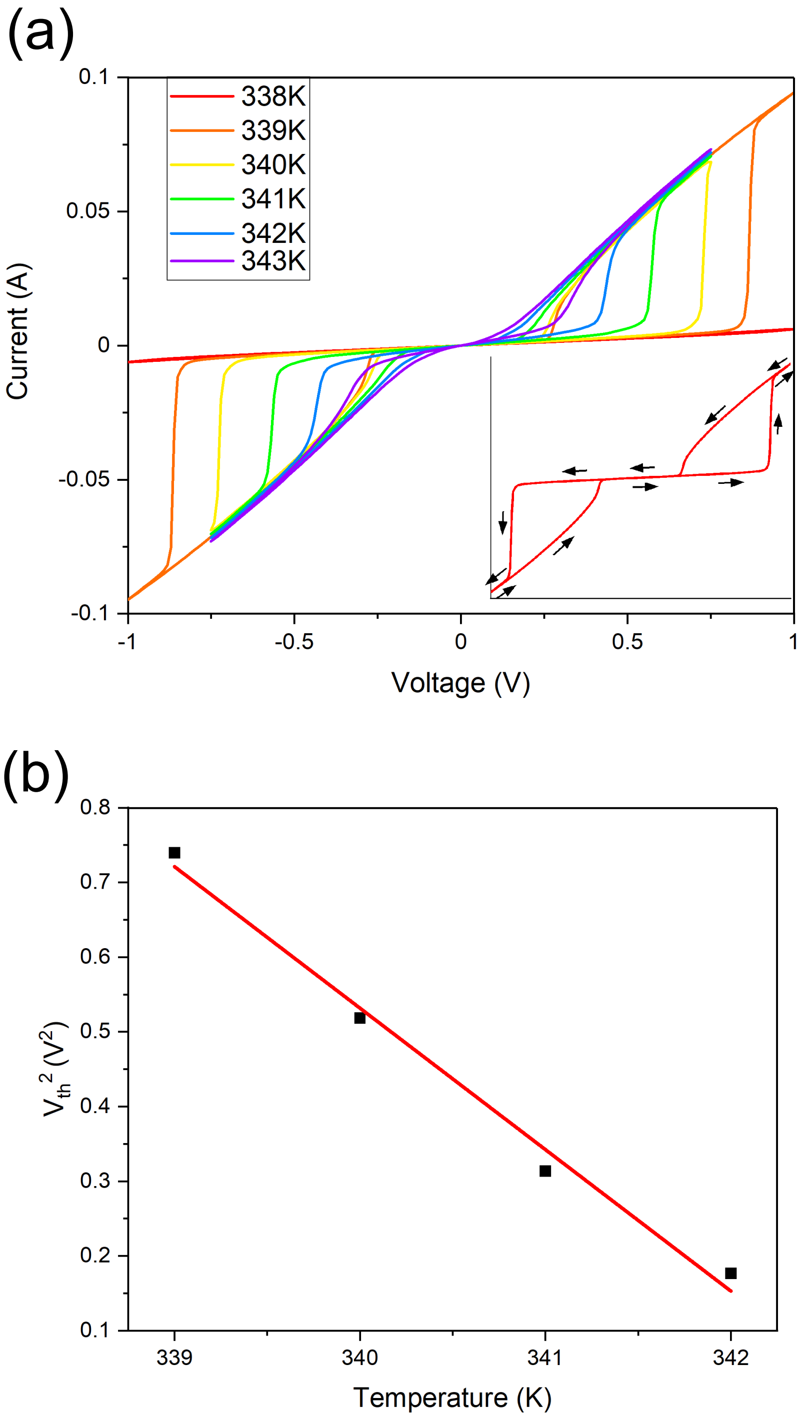

Figure 5.6: (a) IV curves of the sample at different temperatures. At higher temperatures a lower voltage is needed to switch the sample from high to low resistance states. (b) plots the required switching voltage (squared) against the temperature of the device to find a linear relationship.

$$V_{th}^2 = R.k(T_{MIT} - T_S) \tag{5.2}$$

If T_S is reduced additional voltage is required to induce a RS, as is observed. V_{th}^2 is plotted against T_S in figure 5.6(b). V_{th} is taken as the maximum of the second derivative of the VI graph, figure 5.6(a). The linearity is indicative to the Joule heating mechanism. The intersect of the x-axis is the set temperature at which no voltage is required to induce the RS, i.e. the transition temperature. From this graph one obtains $T_{MIT} = 342.78 \pm 0.18\,\mathrm{K}$ which is in good agreement with the value of 342.15 K obtained from the resistance vs temperature measurement (figure 5.5(b)). The slope is the product of R and k_{eff}. R, the measured metallic resistance of the channel taken from the VI measurement, is $70\,\Omega$. Therefore, $k_{eff} = 96 \pm 5 \times 10^{-5}\,\mathrm{W\,K^{-1}}$.

When VO_2 is in the rutile state and the voltage is sweeping down, the channel switches back to the monoclinic state at a voltage lower than V_{th}. Clearly the power at any given voltage is greater in the low-resistance state. The power when the material switches to the metallic state will be approximately equal to power when it switches back to the insulating state. The only variance is due to the temperature hysteresis (see figure 5.5(b)).

The slope of the RS can be seen to be related to V_{th}, increasing with higher voltages. The power increases more dramatically when the voltage is greater, giving rise to more rapid heating. Studies which report a considerably larger threshold voltages report an extremely sharp switch [109, 110].

5.5 Transmission Electron Microscopy

Here, a TEM overview of an untreated and an annealed V_2O_5 crystal is presented. In Figures 5.7(a) and (b), the downward direction of the page is the vertical direction in the image, with the surface at the top of the image. The vertical lamellae are cut with thicknesses (corresponding with the direction normal to the page) of 70–80 nm. The V_2O_5 sample is coated with a protective carbon layer.

In Figure 5.7(a) a TEM overview image of an unannealed V_2O_5 sample cross-section is shown along with the corresponding diffraction pattern (DP). The image does not show any features in the sample like cracks, grain boundaries or dislocations, i.e. on the scale of the prepared lamella the sample is practically a perfect single crystal. The DP also supports this conclusion. Indexing of the DP shows good coincidence with the V_2O_5 with the surface plane parallel to the [100] crystallographic direction. The schematic in the image shows the orientation of the main V_2O_5 lattice directions.

The structure of the sample changes dramatically after the annealing at 800 K.

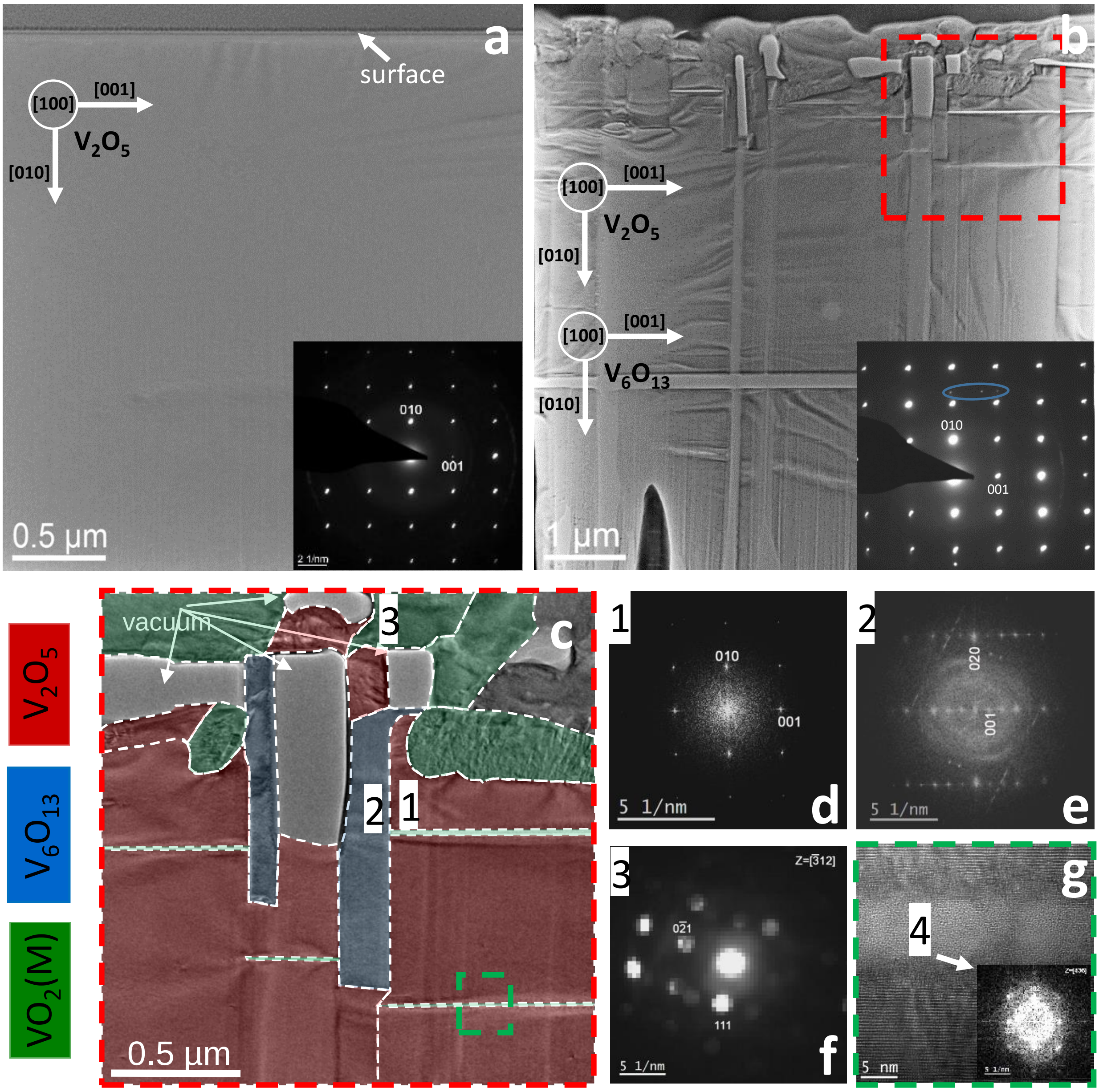

Figure 5.7: Structure of the vanadium pentoxide crystal in (a) as-grown state and (b–g) after annealing at 800 K. (a) TEM image of the as-grown sample. (b) TEM overview image of the sample after annealing at 800 K. Inserts in (a) and (b) show DPs from the entire sample and the orientation of the phases relative to the sample frame. (c) enlarged fragment of (b) indicated by the red dashed square; the colour of the image areas depends on the phase allocation; the colour code is at the bottom left of the figure. (d) & (e) FFTs from the TEM images of areas 1 and 2 in (c), which are determined to correspond to V_2O_5 in 1 and V_6O_{13} in 2 with zone axis parallel to [100] direction in each lattice. (f) nanobeam diffraction from the area 3 in the samples surface; the phase is concluded to be VO_2. (g) enlarged fragment of (c) indicated by the green dashed square; A thin well-defined strip is separated by crystalline V_2O_5. The FFT - correspond to the thin strip - indicates it consists of VO_2 and some amorphous material.

A low magnification TEM image in Figure 5.7(b) shows that the sample is divided in a number of rectangular areas. While there is contrast in all areas of this annealed sample, the most significant features are 1–2 µm from the surface. The main reflections in the DP, depicted inset, collected from the entire sample correspond again to the V_2O_5 phase. However, some additional weaker reflections indicated by the arrows in the DP are also observed. There is not enough of these reflections for unambiguous indexing. This will be done later based on the TEM data.

Detailed analysis of the sample structure was performed on a small part of the sample indicated by a red dashed square in Figure 5.7(b). An image of this area is shown in Figure 5.7(c). The colour assignment is the result of the phase analysis based on the TEM and nanobeam diffraction data. Red, blue and green correspond to V_2O_5, V_6O_{13} and VO_2(M), respectively. Part of the image indicated by arrows contains no material due to the FIB milling. The main part of the sample is occupied by V_2O_5 which corroborates with the DP from the entire sample (Figure 5.7(b)). A fast Fourier transform (FFT) of area 1 is depicted in Figure 6(d). All the individual areas occupied by V2O5 have the same orientation in the sample plane and along the normal direction. Another structural feature in the annealed sample (blue) is areas over a micron in size in the vertical direction and 100–200 nm in size in the horizontal direction. The FFT from area 2 is shown in Figure 5.7(e). Indexing of the FFT gives the match with the V_6O_{13} structure. All the individual areas of Figure 5.7(c) occupied by V_6O_{13} have the same orientation, which is depicted in Figure 5.7(b).

The presence of this phase explains several weak reflections in the DP from the annealed sample (see inset of Figure 5.7(b)). The surface layer of the sample consists of large grains (green) with an undefined shape. The nanobeam diffraction technique was employed to analyse their crystallography; According to the data obtained, these grains belong to the VO_2 phase and have an arbitrary orientation. The nanobeam DP demonstrated in Figure 5.7(f) correspond to area 3 of the sample.

A remarkable structural feature of the annealed sample is the splitting of the initially single crystalline V_2O_5 phase by narrow extremely defined strips in the direction parallel to the sample surface. A higher magnification TEM image from the area, highlighted by the green dashed square in 5.7(c), is shown in 5.7(g). The FFT inset correspond to the strip, reveals it consists of VO_2 and an amorphous phase giving rise to the halo in the FFT.

5.6 Discussion

The annealing experiments show that the VO system derived from annealing V_2O_5 forms a complex system of phases. Anneals at 600 K promote V_4O_9, which I conclude

	V_{th} (V)	d	E (V/m)	k_{eff} (W/K)	Substrate
This Work	0.85	2 mm	425	$96 \pm 5 \times 10^{-5}$	Reduced V_2O_5
Mun *et al.* [109]	6.8	0.2 mm	34,000	7×10^{-4}	Single Crystal
Yoon *et al.* [110]	14	5 μm	2.8×10^6	10^{-3}	Thin Film on Al_2O_3
Li *et al.* [111]	7.5	6 μm	1.25×10^6	10^{-4}	Thin Film on TiO_2

Table 5.2: Table comparing electric field switching values of different VO_2 devices. The field required in this experiement is considerable lower than any previous publications.

to be of high resistance. Anneals at 900 K promote V_6O_{13}, and produces a surface low in resistance, expected from the low resistance phase.

Anneals at 700 K and 800 K give us sample with a low resistance but also a visible VO_2(M)/(R) MIT. These samples are shown to contain contributions from many VO phases, but only V_6O_{13} is a low resistance phase. I conclude in these experiments that the low resistance monoclinic state of the RS is due to a mixture of VO_2 and V_6O_{13} on the V_2O_5 single crystals. It is this unique mixture that enables the extremely low electric field, Joule driven RS.

The low resistance of the monoclinic state gives rise to a small resistance change at T_{MIT} of a factor of 20 (Figure 5.5(b)) in comparison to 5 orders of magnitude for single crystal VO_2 [3]. In thin film VO_2 the resistance change in VI is often orders of magnitudes lower than the resistance change upon heating (see [169] for example). The annealing experiment suggests that the MIT improves in size and narrows in width with longer annealing times, showing superior qualities at anneal times of over 20 h. This is attributed to improving VO_2 quality. Whether this is due to growing domain or grain sizes, or simply an increase in the VO_2(M) present is unknown.

RS experiments on a sample annealed at 800 K for 16 h show a anomalously low threshold switching field for a VO_2 type transition. To the best of the author's knowledge the threshold field is considerable lower than anything reported in the literature (table 5.2). Low voltage clearly has the benefit of reducing field induced device degradation and reducing the resistive switching to one mechanism: Joule heating. In addition, a low threshold voltage produces a smaller power surge at the transition point. This will limit heating beyond the transition temperature, reducing the possibility of undesirable changes to the VO_2.

In this system the low threshold voltage is due to the low resistance of the monoclinic state, shown to be due to a mixture of V_6O_{13} and VO_2(M) in the surface layer. The power per Kelvin required to induce the RS ($96 \pm 5 \times 10^{-5}$ W/K) is comparable (table 5.2) to other work performed with a VO_2 single crystal (70×10^{-5} W/K) in which Joule heating is concluded to be the dominant mechanism [109]. The low resistance reduces the voltage required to achieve this power threshold. The resistance of the monoclinic state can be reduced with the inclusion of oxygen vacancies [170]. However, this reduces the T_{MIT}, widens the transition and simultaneously increases the resistance of the rutile, high temperature phase, further reducing the magnitude of the resistance change at the transition. The T_{MIT} and width of the transition strongly suggest that the VO_2 in the system is stoichiometric.

Metal ion doping has been also been shown to lower the resistiance of the monoclinic state, and hence may also induce a lower switching threshold voltage [11,104]. However, doping also has the added effect of shifting the MIT temperature. This system uniquely lowers the threshold voltage while keeping the T_{MIT} at expected value of 340 K.

Equation 5.2 highlights that the effective thermal conductivity and the resistance of the monoclinic state play equally important roles in reducing the threshold voltage. The effective thermal conductivity, k_{eff}, is estimated to be $96 \pm 5 \times 10^{-5}\,\mathrm{W\,K^{-1}}$. Table 5.2 compares k_{eff} in the literature calculated by the same means as this work (figure 5.6(b)).

This work represents the highest k_{eff} value, but one must keep in the mind that this value is related to the distance between probes. The probe distance of 2 mm is considerable larger than [110] and [111]. k_{eff} - the effective thermal conductivity - is related to the VO_2 but also the substrate, contacts et cetera. The thermal conductivity of VO_2, V_2O_5, TiO_2 and Al_2O_3 are 0.2 [171], 0.45 [172], 10 [173] and $35\,\mathrm{W\,mK^{-1}}$, respectively. The V_2O_5 substrate in this system can reduce the effective thermal conductivity in comparison to the conventionally employed substrates, and therefore, reduce the threshold voltage. An addition benefit of this vanadium oxide substrate is that foreign cation intercalation is not a possibility.

If the probe length is reduced the effective thermal conductivity and the resistance of the monoclinic state will reduce, further reducing the threshold voltage [110]. The exact dependence of the threshold voltage on the probe distance is not trivial: the current distribution can change as a function of probe geometry, which in-turn can alter the channel size and heat distribution. Lowering the nessesary field for RS also introduces the potential for realising switching at room temperature.

TEM measurements confirm the crystaline nature of the V_2O_5 samples. A sample annealed at 800 K shows a surface layer composed of predominantly VO_2 and V_6O_{13} structures, as theorised using XRD and electronic measurements. Ususual features, such as an amorphous VO_2 strip beneath the surface layer are also observed. Further microscopy investigations are required to characterise all features and determine precise geometry of phases present in the reduced sample.

5.7 Conclusion and Outlook

In this chapter, through reduction of V_2O_5 single crystals, a surface with a anomalously low field RS has been created. The switch is found to be due to Joule heating inducing a thermal MIT in VO_2(M) present in the surface.

Detailed XRD, RT and XPS analysis of samples annealed at 600–900 K document the reduction process at different temperature as a function of time. The surface formed is a mixture of vanadium phases with 4+ and 5+ valencies. It is found that a low resistance VO_2(M) type MIT is found in these surfaces in anneals at 700 and 800 K, and concluded that this is due to the mixture of VO_2(M) and V_6O_{13} present in the surface layer.

A sample annealed at 800 K for 16 h exhibits the same characteristic low resistance MIT. It is shown that this sample undergoes RS with applied voltage. The fields used are the lowest reported in literature to date for VO_2 systems, at $425\,\mathrm{V\,m^{-1}}$. The mechanism is shown to be due to Joule heating.

In terms of applications, this low voltage/low power switch may be of great interest in enabling electronic applications of RS systems. This method of preparing low resistance VO_2(M) type materials enables another mechanism for designers of RS devices to tailor the functioning material to their specific needs. Further implications, as well as potential future work, will be examined in Chapter 7.

6

RAS Studies of the Pristine and Reduced V_2O_5(010) Surface

To realise the applications of VO, growth and preparation conditions need to be precisely controlled to achieve the desired structure and stoichiometry. Optical *in situ* characterisation methods can provide increased control and accuracy, observing structural changes as they are induced. This can be done without exposing the sample to atmosphere, unlike *ex situ* techniques such as x-ray diffraction or ellipsometry, for example. Among these *in situ* techniques, RAS presents itself as a candidate providing a non-destructive optical method with good sensitivity and ease of use. However, RAS can only be applied to samples with optical in-plane surface anisotropies. Further details of RAS can be found in section 2.7.

The vanadium oxide family is an ideal candidate for RAS measurements, with many of the crystal phases having well documented structural and optical anisotropies (Chapter 3). In this chapter, reflectance anisotropy spectra for bulk V_2O_5 crystals with a (010) surface is presented in the context of it's structural anisotropy and it's axial optical constants as measured via ellipsometry. Then, bulk V_2O_5 crystals with a (010) surface were reduced in vacuum at different temperatures, and the RAS spectra of these samples is discussed in relation to their surface composition to determine RAS contributions of other vanadium oxide phases. A theoretical RAS spectrum of V_6O_{13} is calculated and shown to be present in the measured spectra. Finally, the effect of the metal-insulator transitions of VO_2 and V_6O_{13} are shown to have an effect on the measured RAS spectra.

Details on the structures and properties of all relevant VO phases are covered in Chapter 3.

6.1 Experimental Procedure

V_2O_5 crystals were float zone grown (Materials Modeling and Development Laboratory). Spectroscopic ellipsometry of a pristine V_2O_5(010) surface was performed by Chris Smith at TCD. All other procedures were performed at TCD by myself or Dr. Brian Walls. V_2O_5 readily cleaves along the (010) surface due to weak bonding in that plane resulting in a pristine reflective surface. This surface orientation was confirmed via x-ray diffraction.

Four V_2O_5 crystals were annealed in a vacuum furnace at a pressure of approximately 1×10^{-4} Torr. Anneals were performed for intervals of one hour at 700 K, 800 K and 900 K; and intervals of two hours at 600 K.

All above samples were characterised via resistance vs temperature (RT) measurements, XRD and RAS. XPS was used on a pristine V_2O_5 crystal. Temperature dependent RAS measurements were performed on specific samples outlined below. Relevant findings are presented in the sections below.

All measurements presented in this chapter are single individual measurements. Simulated data is also presented without error.

Details of all above techniques can be found in Chapter 3.

6.2 RAS of the V_2O_5(010) Surface

Initially the RAS response of the (010) surface has been measured. XPS was used to confirm the single V^{5+} valence state of the sample. XRD confirmed the (010) out of plane surface. The (110) lattice plane was found using an in-plane XRD phi scan. It revealed a two-fold symmetry confirming the single crystal structure of this orthorhombic material. The largest RAS signal was found when the RAS measurement axes, x and y, coincided with the two main in-plane axes, [100] and [001] respectively. The real part of the RAS response of the V2O5(010) is shown in figure 6.1.

The real part of the RAS has a sharp positive peaks at 2.88 eV, 3.48 eV and 4.38 eV, and negative peaks at 3.2 eV and 3.88 eV. Positive RAS signal denotes a higher reflectivity for light polarized along the [100] axis (r_x). In the infrared (IR) region (0.8–1.7 eV), the RAS spectrum is positive and almost constant. Negative RAS signal would correspond to higher reflectivity along the [001] axis (r_y).

The real and imaginary parts of both the dielectric function and the refractive index along the [100] and [001] axes as meaured by ellipsometry are shown in fig 6.2. Clear differences in these spectra show the optical anisotropy of the surface. Using these measured dielectric components with the two phase model as defined in section 2.7.2:

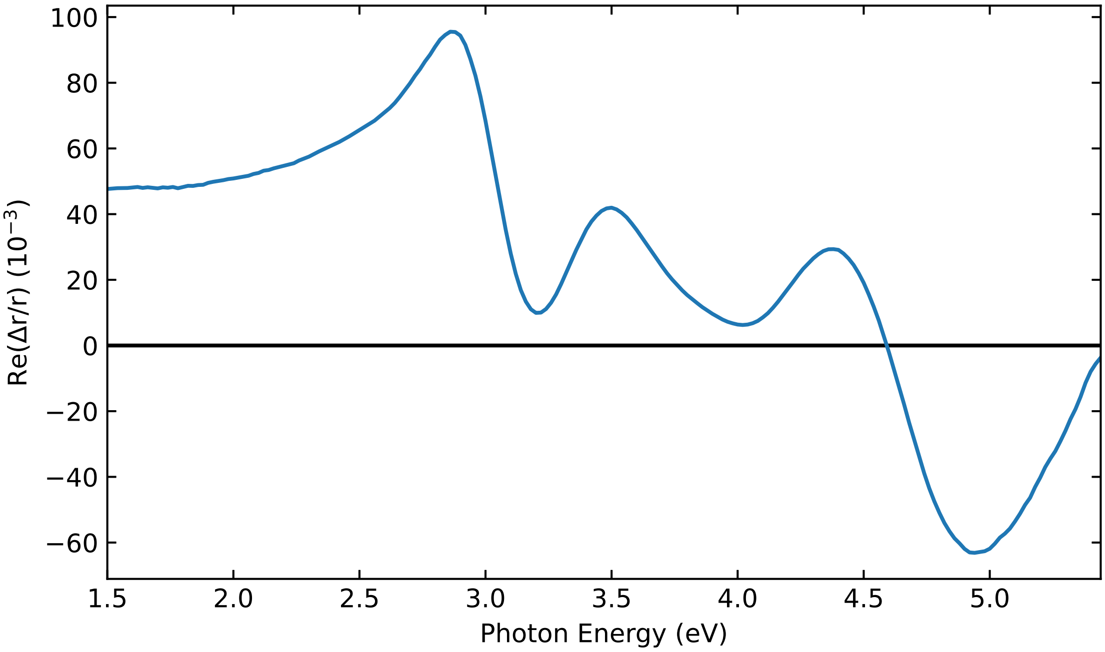

Figure 6.1: Real part of the $V_2O_5(010)$ surface RAS spectrum.

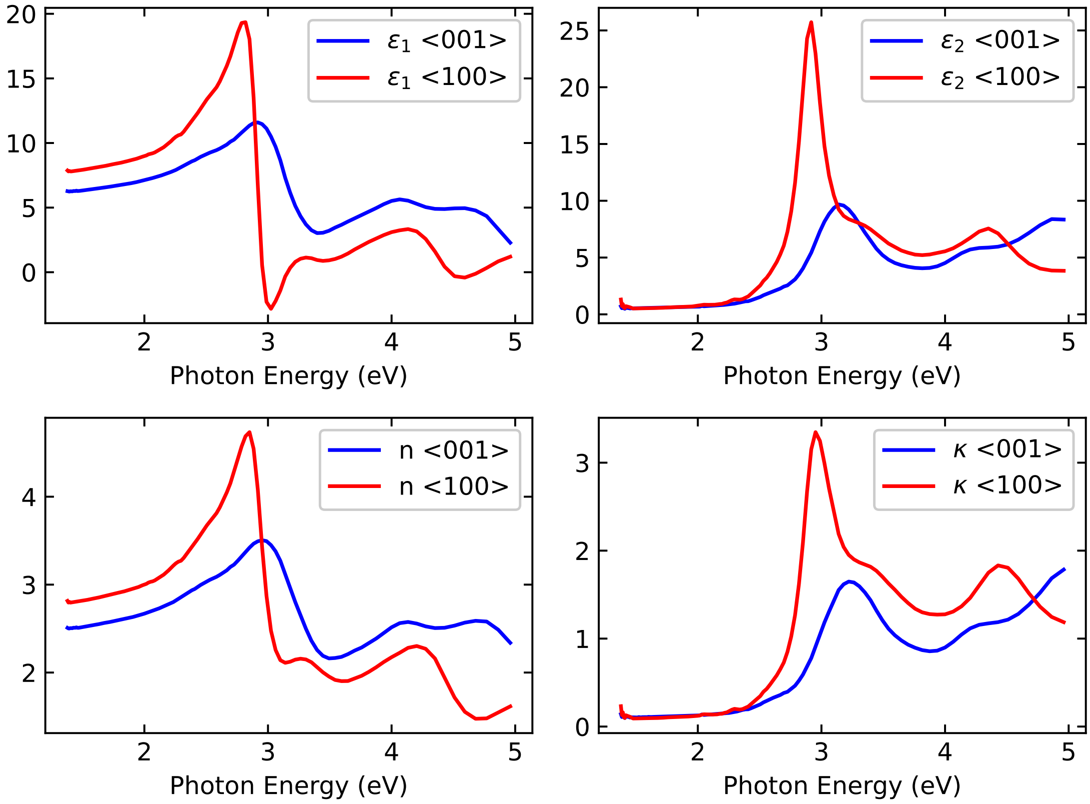

Figure 6.2: Axially resolved real and imaginary components of V_2O_5 optical constants as measured via ellipsometry, including refractive index and absorption coefficients.

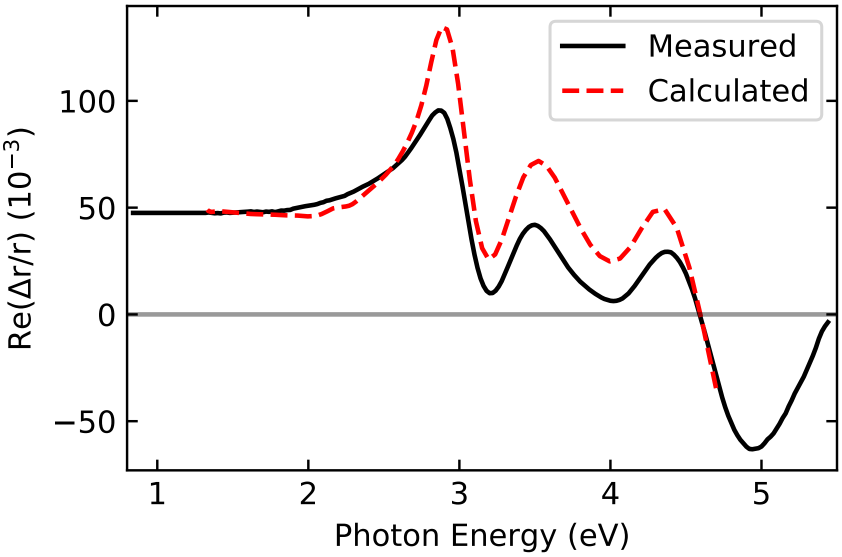

Figure 6.3: Comparison of measured RAS spectra of the $V_2O_5(010)$ surface and a RAS spectra calculated using the axially resolved dielectric function of $V_2O_5(010)$ as measured by ellipsometry.

$$\frac{\Delta r}{r} = \frac{1}{\sqrt{\epsilon}} \frac{\Delta\epsilon}{\epsilon - 1} \tag{6.1}$$

where $\epsilon = \frac{1}{2}(\epsilon_x + \epsilon_y)$ and $\Delta\epsilon = \epsilon_x - \epsilon_y$, the real part of the RAS response was calculated and is also shown in fig 6.3. Other than a difference in magnitude, comparison of the direct RAS measurement and calculated spectrum show good agreement. The magnitude difference is due to signal losses in the measurment process (lower signal to noise ratio).

Our dielectric data is also in agreement with data published by Parker *et al.* [118] as well as others [174, 175]. Parker's work calculates the imaginary component of the complex dielectric function from the simulated band structure of V_2O_5, and show it to be anisotropic in all axes due to different V-O bond types and lengths in each axes. The positive RAS signal in the IR region is correlated to the different refractive index along the [100] and [001] axes.

Further evidence for this can be seen in Parker's work: where a sharp optical transition of 2.8 eV can be seen in the a axis, and 3.2 eV in the c axis, corresponding to features in our measurements. These absorption peaks are due to transitions from filled O2p orbitals to empty V3d states. The conduction band of V_2O_5 is split into an upper and lower band. Parker predicts this lower band to be have predominately $3d_{xy}$ and $3d_{yz}$ character with mixing from the O2p$_y$ orbitals.

Bonds along the [100] axis are V-O(2) bonds, possessing a length of 1.78 Å, and longer V-O(3) bonds, with length 2.02 Å. Along the [001] axis, there are only V-O(3) bonds with length 1.88 Å (see figure 3.6). It should be no surprise that absorption in the [100] is higher at lower energy due to the shorter V-O(2) bond length in this direction, leading to a greater orbital overlap.

Absorption peaks at higher energies are due to transitions from the valence band to the upper V3d band. As the transitions are from O2p to V3d bands again, absorption anisotropy arises from the same differing oxygen coordination bond lengths, and a similar pattern is observed in our data. The absorption coefficient of [100] peaks at 4.4 eV while [001] peaks above 5 eV corresponding to the maximum and minimum seen at 4.4 eV and 5.1 eV in our RAS spectrum.

The data presented above is the first instance of the RAS signal of the V_2O_5(010) surface published. Also presented are the first instances of both components of complex dielectric function and refractive index of the surface published. Results from both ellipsometry and RAS measurement methods are in agreement.

6.3 RAS Measurements of Annealed Samples: V_6O_{13} and V_4O_9 Features

In order to investigate RAS features of other vanadium oxide phases, four V_2O_5 single crystals were annealed as described in section 6.1. Each sample displayed a distinct surface structure and composition throughout annealing as identified by XRD. As expected, the RAS spectra of each sample was also distinct; however, we show an identifiable V_6O_{13} features in the spectra, as well as potential V_4O_9 features.

As outlined in Chapter 3, studies of V_6O_{13} and V_4O_9 are lacking. This experiment presents possibilites to study their optical properties. Futhermore, RAS may help to identify and isolate these compounds, enabling futher studies.

XPS data shown in section 5.2 shows evidence that only V^{4+} and V^{5+} are present in annealed samples, so only VO_2, V_2O_5 and Wadsley phases will be considered.

6.3.1 Development of RAS, RT and XRD Measurements with Annealing

Development and structural properties of the annealed samples are summarised here in regard to RAS, RT and XRD measurements. A more in depth XRD and RT analysis of V_2O_5 anneals at the same temperatures can be found in section 5.3. Here we examine compositional aspects of the crystals to identify RAS contributions.

Figure 6.4 shows the development of the sample annealed at 900 K, now referred

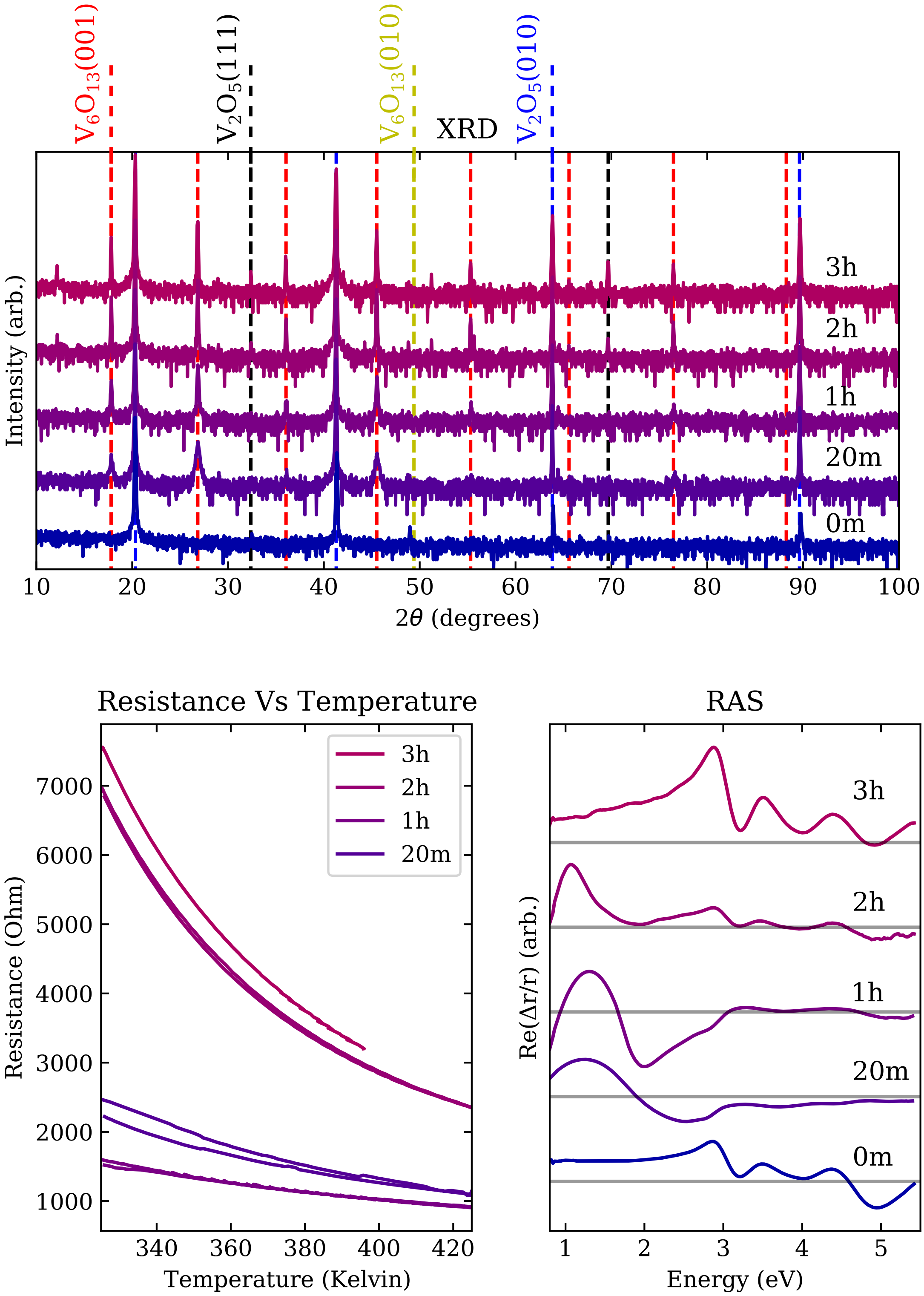

Figure 6.4: XRD, RAS and RT data of a V_2O_5 crystal annealed at 900 K as it evolves.

to as sample 900K.

The XRD pattern of Sample 900K evolves clearly. Initial anneals show the formation of V_6O_{13}(001) peaks, which persist throughout further anneals. The only other phases to appear are further V_2O_5(111) peaks at 2 hours. The introduction of V_2O_5 domains rotated relative to the pristine crystal suggests the V_2O_5 surface of lower crystallinity. V_2O_5 has a melting point of 680 °C, so the surface is likely unstable at these temperatures. High bulk oxygen mobility at these temperatures would also maintain a depleted V_2O_5 surface. [136] Analysing the RAS spectra, annealing for 20 m and 1 h gives a pattern distinct from V_2O_5 with a large feature at low energy (1 eV). At 2 h, the V_2O_5 RAS pattern can be seen at lower intensity, and at 3 h, the RAS has returned to a V_2O_5(010) pattern. Finally, RT data shows that initial anneals (20 m & 1 h) lower the resistance of the sample, evidence of the metallic V_6O_{13} seen in the XRD. However, the resistance rises again with further annealing.

Overall for sample 900K, the surface readily forms V_6O_{13}, but further annealing only promotes V_2O_5, so much so that after 3 h, the RAS signal is that of the V_2O_5(010) surface. Our data suggests the surface deteriorates in crystal quality. This aligns with other studies showing little to no reduction of V_2O_5 at high annealing temperatures [136]. V_6O_{13} contributes to a lower resistance, and its contribution to the 0.8–2.5 eV RAS signal will be examined in section 6.3.3.

Figure 6.5 shows the development of the sample annealed at 800 K, now referred to as sample 800K.

Annealing for 20 m, the XRD pattern of sample 800K shows three new phases: a strong V_6O_{13}(001) contribution and weaker V_4O_9(001) and V_6O_{13}(010) signals. Further annealing consolidates the V_6O_{13}(001) features. The V_6O_{13}(010) remains, but evidence of V_4O_9 disappears. From 1 h up to the 6 h measured, the XRD pattern stays the same. RT shows the sample continuously lowers in resistance as annealing continues, evidence of the metallic V_6O_{13} contribution, but from 2 h onward we see a MIT characteristic of VO_2. As discussed in Chapter 5, VO_2(110) shares the same out of plane XRD pattern with every even V_6O_{13}(001) peak. However, the MIT of VO_2 and the XRD peaks unique to V_6O_{13}, show both phases are present on the surface of this sample. Considerable change of the RAS spectrum can be seen after 20 min despite the resistance remaining high, a possible influence of anisotropic V_4O_9(001) observed in the XRD at this time. Continued development of the RAS spectra shows a large feature in the 0.8–2.5 eV, similar to that seen in early anneals of sample 900K of which V_6O_{13} is present in both cases. The pronounced V_2O_5 features are intermediately removed.

Sample 800K shows evidence of V_6O_{13} throughout its annealing cycle, with V_4O_9

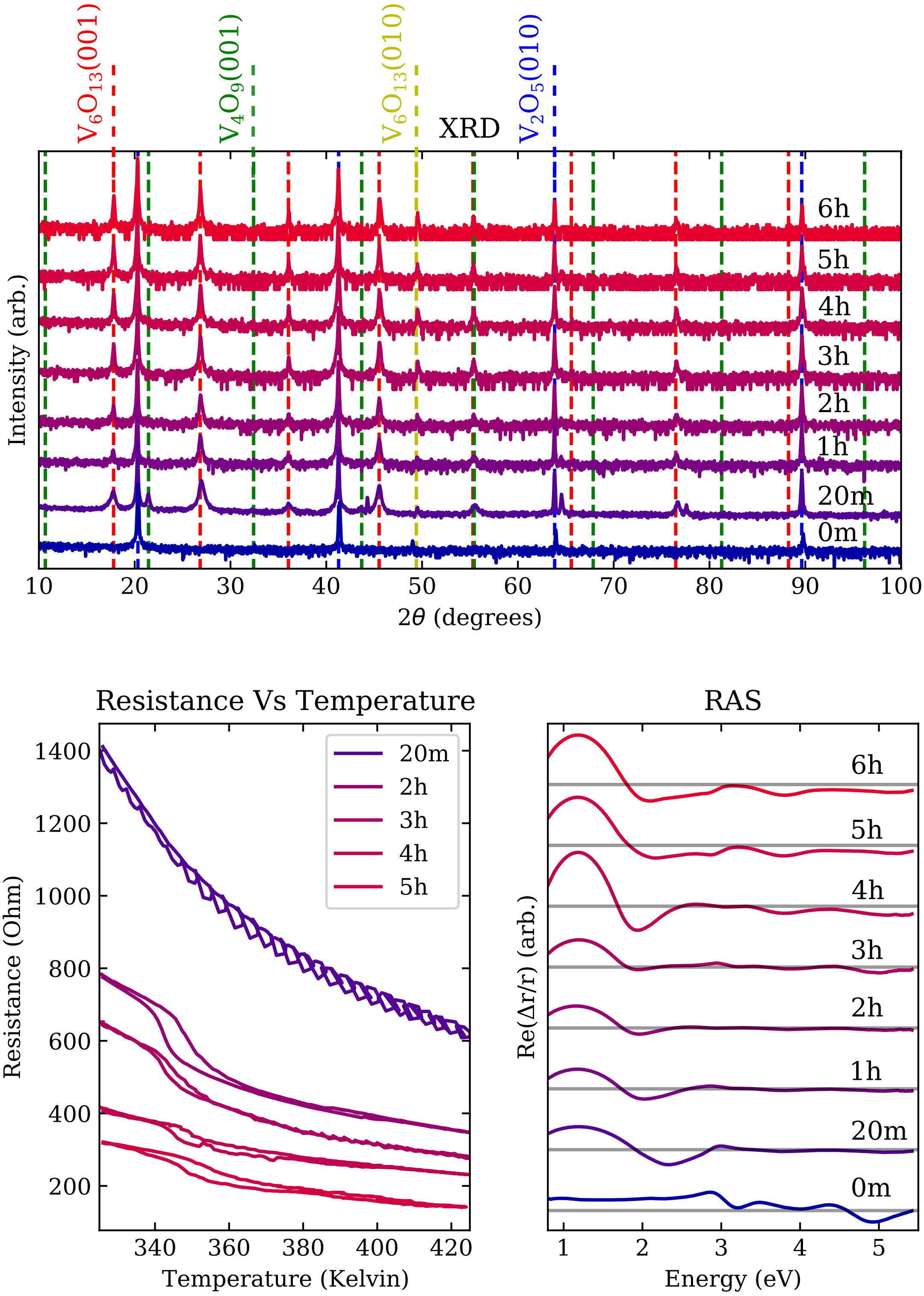

Figure 6.5: XRD, RAS and RT data of a V_2O_5 crystal annealed at 800 K as it evolves.

only seen at an anneal time of 20 m, and evidence from the RT data of VO_2 after 2 h.

Figure 6.6 shows the development of the sample annealed at 700 K, now referred to as sample 700K.

XRD of sample 700K shows a relatively consistent composition throughout its annealing cycle. The dominant phase formed is V_4O_9(001), but weak signals relating to V_6O_{13}(001), VO_2(B)(001) and V_6O_{13}(010) are also present. The region from 25–30° shows a large undefined feature between the appropriate V_6O_{13}(001) and VO_2(B)(001) regions. Seeing as these are consecutive epitaxial phases in the V_2O_5–VO_2(B) reduction pathway, this pattern suggests a gradual spatial transition from one phase to the next as opposed to an acute phase boundary. The RT data shows a consistent resistance with annealing, agreeing with the relatively constant composition of the material surface. The resistance is the highest yet of the samples, evidence of less V_6O_{13} than seen in the other samples. The RAS signal shows a positive feature in the IR after 20 m and up to 3 h, although smaller than that observed in samples 800K and 900K. A large negative feature also appears around 3 eV at 20 m, and shifts to lower energies with annealing. At 5 h, the RAS signal seems to be moving back towards a V_2O_5(010) type signal (maxima-minima around 3 eV), although very weak.

Although the composition of sample 700K from XRD and RT measurements seems constant, the RAS of the sample changes more dramatically with annealing. Phases identified via XRD are V_6O_{13}, V_4O_9 and VO_2(B).

Figure 6.7 shows the development of the sample annealed at 600 K, now referred to as sample 600K.

XRD of sample 600K shows only V_4O_9(001). The signal is weak after 20 m, but from 2–22 h, the signal is strong and constant. Resistance of the sample stays in the high kΩ range relative to other samples, consistent with the lack of a more conducting phase in the XRD. RAS of this sample diverges from the pristine crystal immediately and becomes consistent between 4-8h, showing a collection of features between 2–5 eV.

Sample 600K appears have a surface composed of V_4O_9(001), with no other phases seen forming on the V_2O_5 crystal.

To summarise, the surface of sample 900K is composed of largely V_6O_{13}(001) with V_2O_5 evidence present in all measurements. Sample 800K has a surface composed of VO_2(M)(110) and V_6O_{13}(001), with a weak V_6O_{13}(010) presence also seen. Early anneals show V_4O_9(001) also. Sample 700K is the most complex, with consistent contributions from VO_2(B)(001), V_6O_{13}(001), V_4O_9(001) and V_6O_{13}(010). The sur-

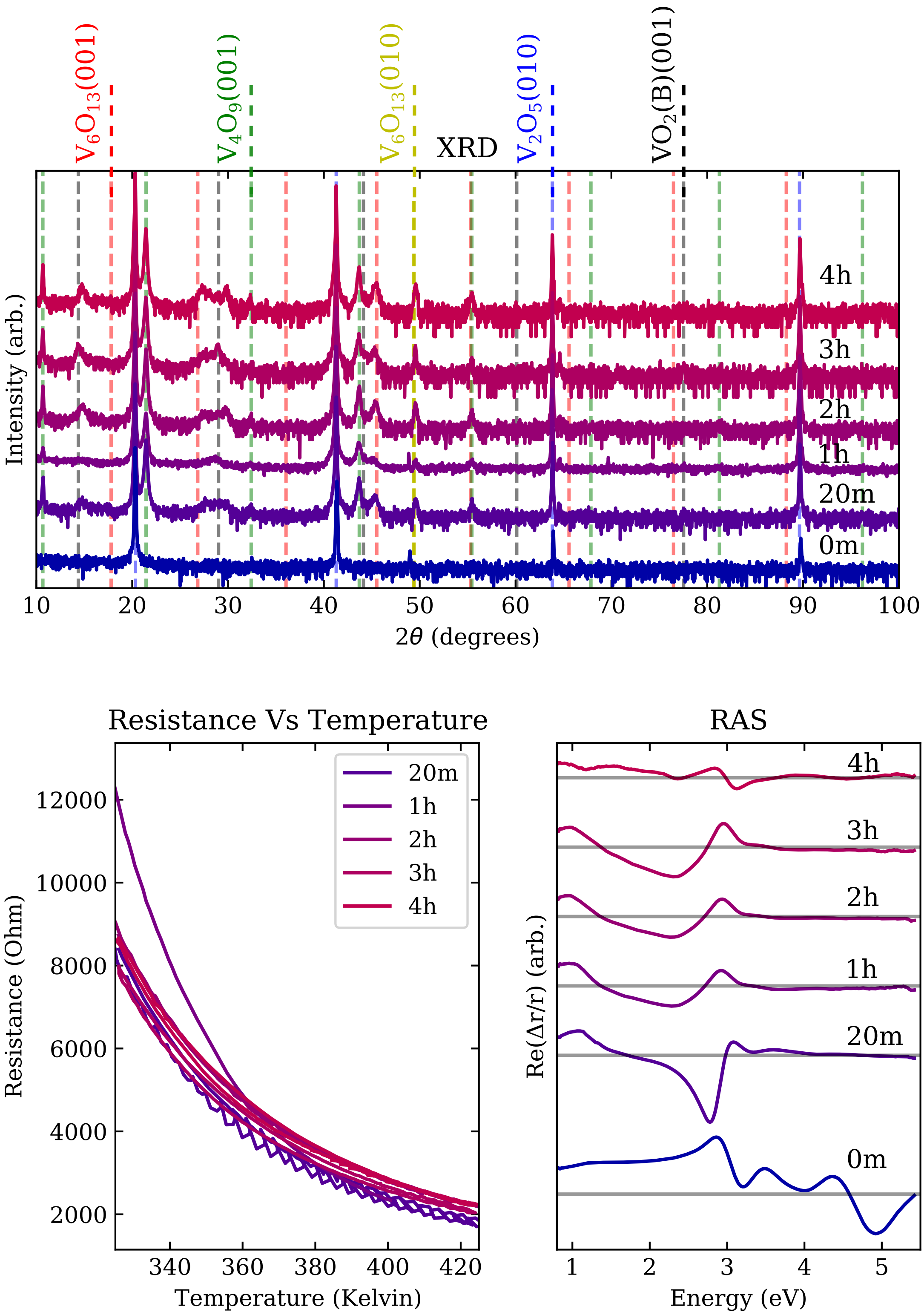

Figure 6.6: XRD, RAS and RT data of a V_2O_5 crystal annealed at 700 K as it evolves.

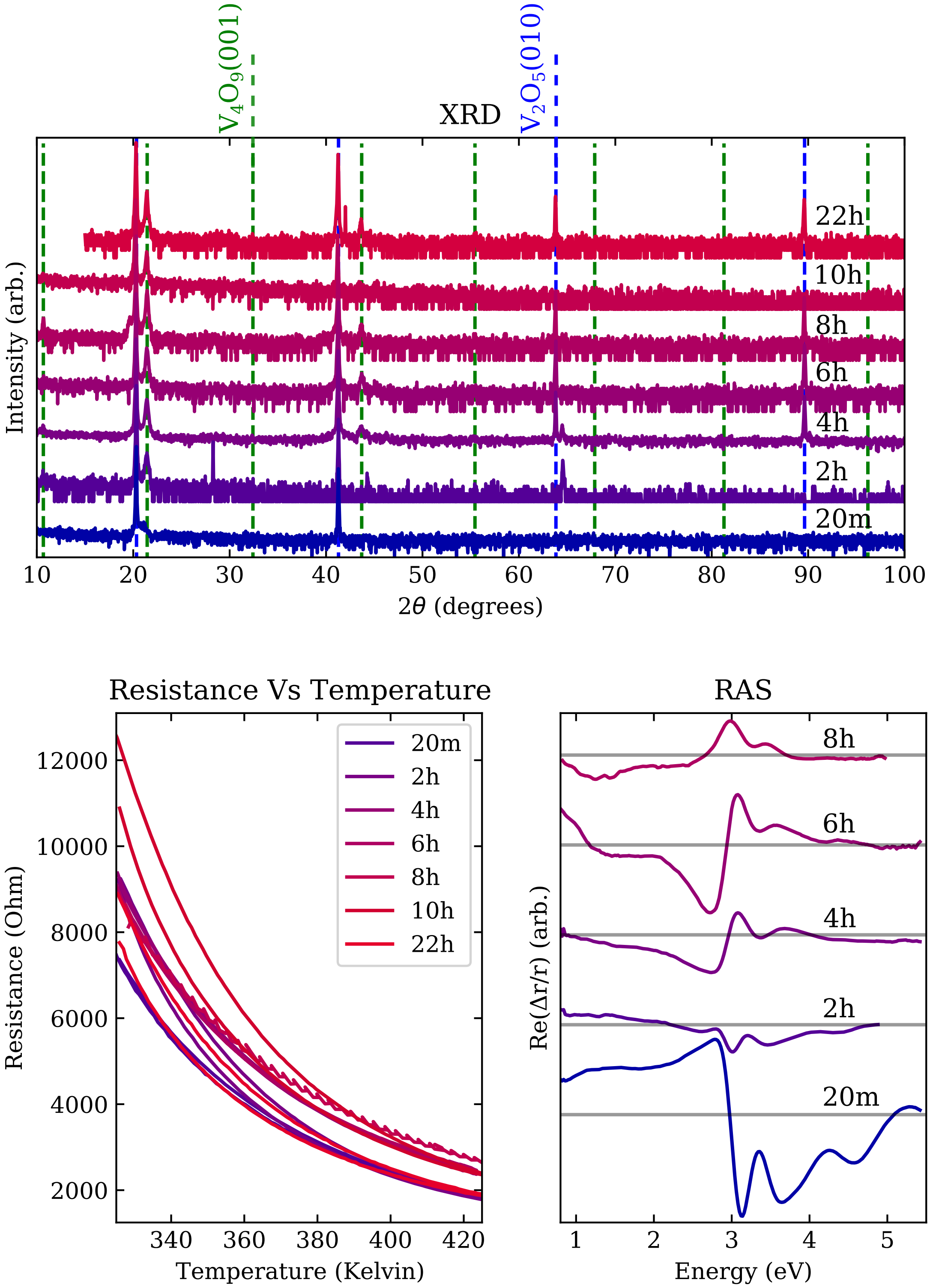

Figure 6.7: XRD, RAS and RT data of a V_2O_5 crystal annealed at 600 K as it evolves.

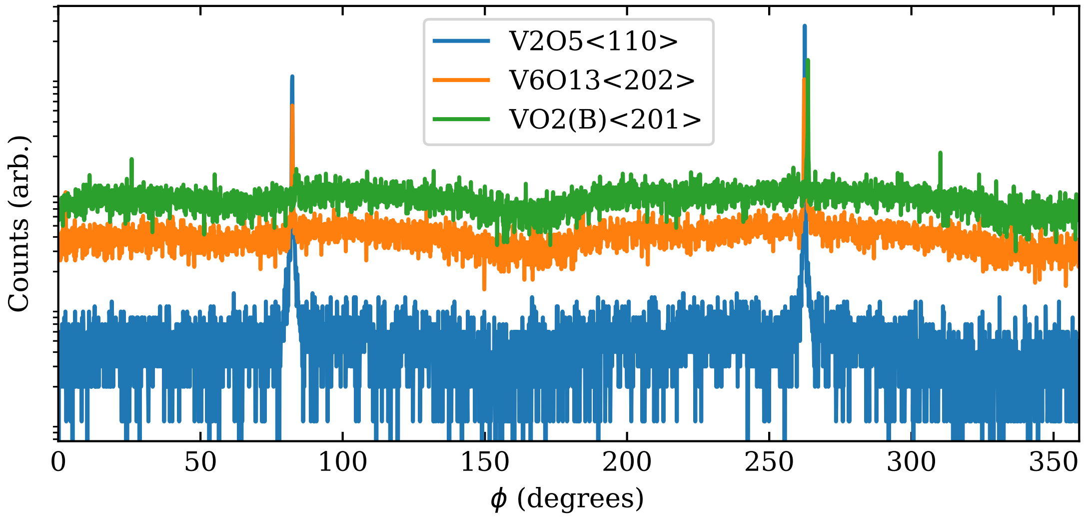

Figure 6.8: Phi scan of sample annealed at 700 K identifying in-plane allignment of V_2O_5, V_6O_{13} and VO_2(B) phases.

face of Sample 600K only has measurement contributions from V_4O_9(001). These findings show agreement with the results of section 5.3.

The changing RAS spectra for the samples above are presented without detailed analysis. As the XRD and RT have shown, all samples show changing and complex surface compositions. The resulting RAS spectra are a complex combination of all present phases' thickness, ordering and other structural considerations [43]. Therefore features are difficult to assign to phase contributions without more information. Specific distinguishable features will be identified and discussed in section 6.3.3 using comparison of samples and optical data found in literature.

6.3.2 In-plane XRD and RAS Measurements with Sample Rotation

In this section, in-plane XRD is used to examine the structural relationships between the different structural phases present in the annealed samples with the objective of assigning crystal orientations and therefore anisotropic contributions of specific phases if possible. Similarly, RAS measurements on samples rotating in-plane will show if there is any contribution to the RAS signal from axes in different, unaligned orientations due to i) multiple in-plane rotated domains of a particular phase or ii) phases maximal RAS signal from different phases being at different angles.

In the reduction process of V_2O_5, reduction through the phases V_4O_9, V_6O_{13} to VO_2(B) have been theorised and measured as described in section 3.6. If this is the

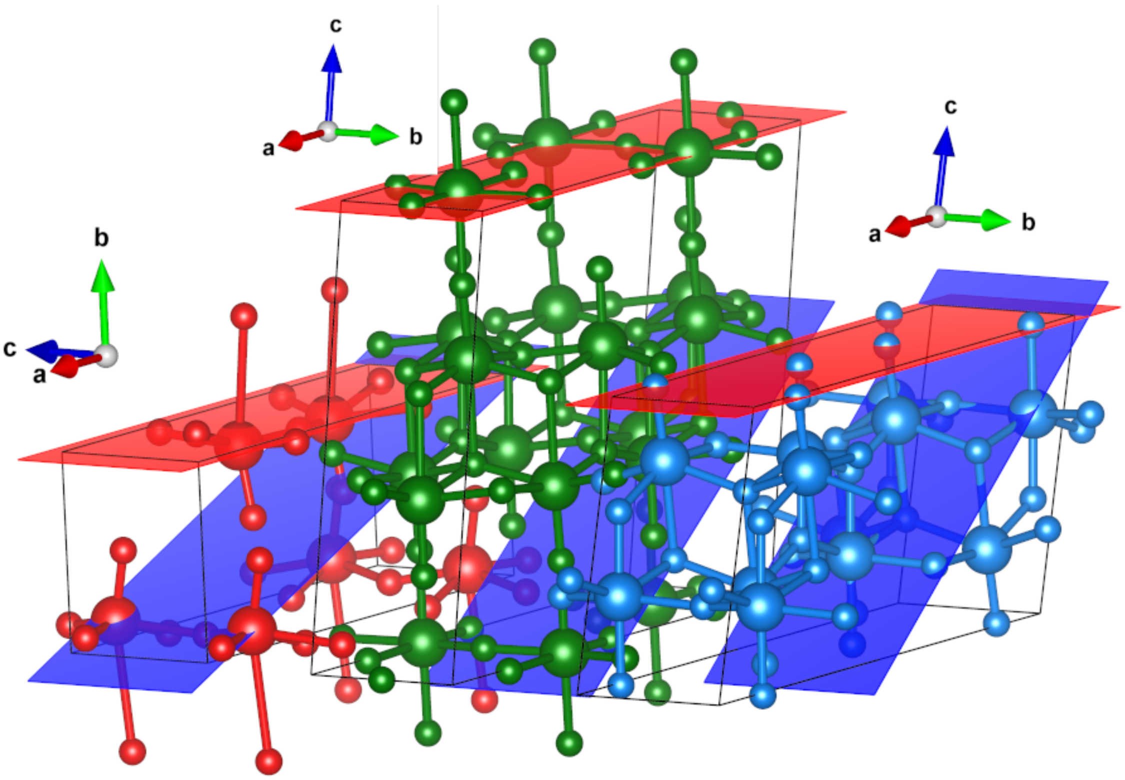

Figure 6.9: aligned structures of V_2O_5, V_6O_{13} and VO_2(B) phases based on their surface structures identified via XRD (red slices) and aligned in plane orientations identified via phi scan (blue slices).

case with the annealed samples above, in-plane XRD should reveal clear in-plane relationships.

Sample 700K is used as an example, as it has a large number of phases to search for as seen in section 6.3.1. Initially, the 2-fold symmetry of V_2O_5(110) was measured as expected for the orthorhombic structure. 2-fold symmetry of V_6O_{13}(202) was also detected and finally VO_2(B)(201), again with 2-fold symmetry as expected. The scans are plotted in figure 6.8. The 2-fold symmetry indicates these phases exhibit two domains rotated 180° to each other, but these domains will contribute identical RAS signals. Both V_6O_{13}(202) and VO_2(B)(201) in planes are parallel to the V_2O_5(110) plane. Multiple orientations of V_4O_9 were searched for in all samples showing out of plane XRD evidence of appropriate phases, but none were found. Samples 700K, 800K and 900K all showed in-plane V_6O_{13}(202). No in-plane VO_2(M) orientations could be found. Reciprocal space mapping (RSM) of a VO_2(M)(011) plane in section 5.4.1 also suggests that VO_2(M) is polycrystaline in this system.

The structures of V_2O_5, V_6O_{13} and VO_2(B) are shown in figure 6.9 with their relevant out of plane and in-plane orientations highlighted, aligned in the orientations shown by in-plane XRD. The relative orientations align with the epitaxial reduction the literature predicts.

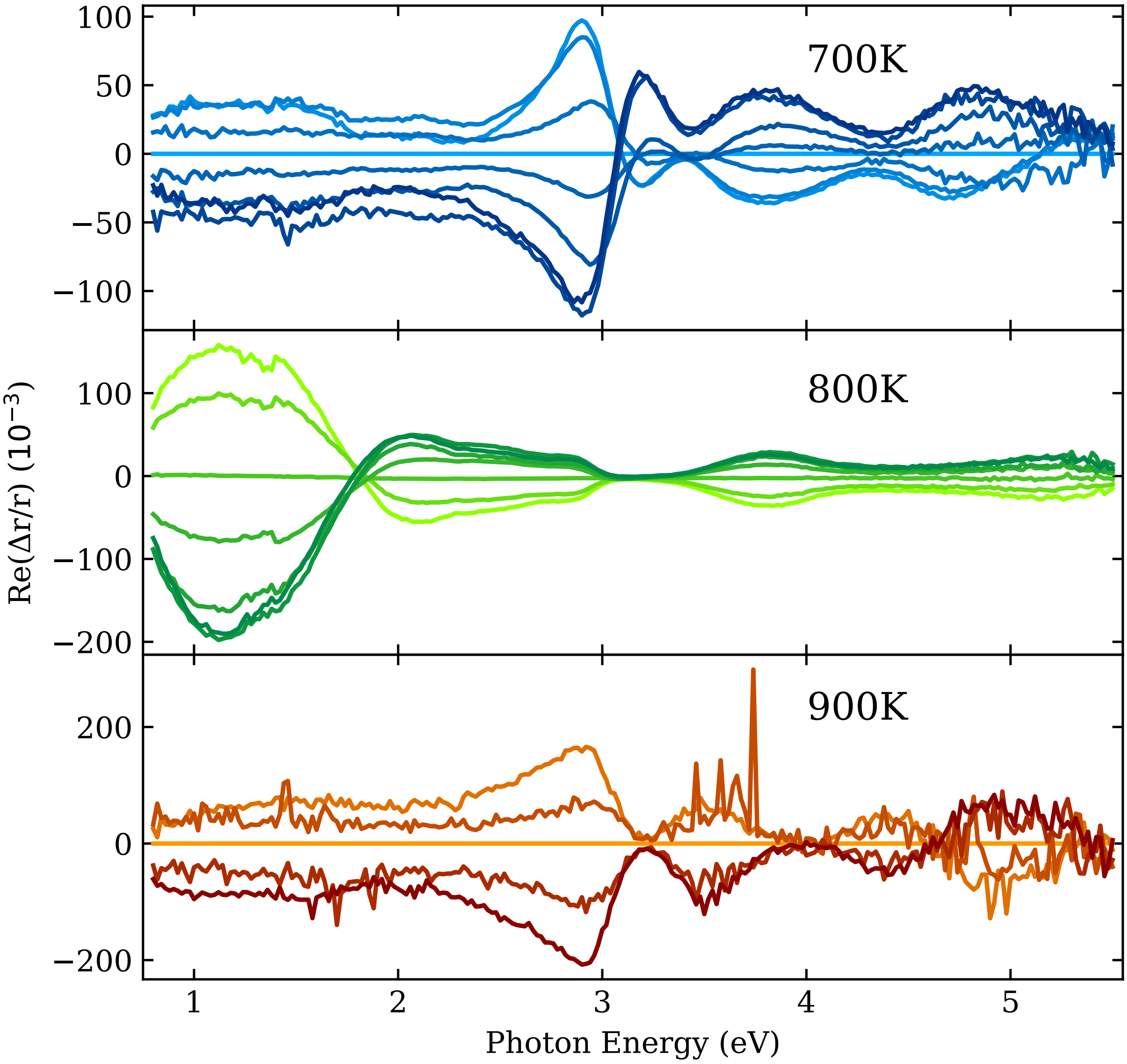

Figure 6.10: RAS measurements of three samples under rotation. Each line depicts 15 degrees of rotation for sample 800K and 700K, and 30 degrees for sample 900K. As the spectra diminish in intensity and then mirror through 90 degrees of rotation with no new contributions present, all RAS contributing components are aligned.

RAS with sample rotation is used to examine contributions to the RAS signal along alternate axes. If contributions along no other axes are present, the RAS signal will diminish, move through zero, and become its mirror negative over 90° of rotation. If other RAS contributing axes are present, different signals will arise. Figure 6.10 shows samples: 900K at 3 hours of annealing; 800K at 6 hours of annealing; and 700K at 4 hours of annealing, through rotation at 15 degree increments. All signals are mirrored upon rotation, with no new signal seen at different angles. With this information, we can assume that all phases contributing to the RAS signals are: (i) uniformly oriented anisotropic phases, with their axes aligned with the V_2O_5 bulk axes; (ii) anisotropic but polycrystaline; or (iii) isotropic phases. These measurements allow one to interpret the RAS as the sum of different RAS signals. The contribution of a phase is due to the intrinsic RAS signal, the degree of crystallinity and the volume it occupies in the crystal with the probed region.

In-plane XRD has shown that V_2O_5 is reduced to V_6O_{13} and VO_2(B) epitaxially and that these structures share common axes. RAS taken at different sample rotations shows no RAS contributions from different axes. V_4O_9 is not forming with uniform structures. The axes are misaligned to V_2O_5. These phases may not be seen in in-plane XRD measurements due to there being a small amount of the phase present. The out of plane XRD signals for these phases are relatively weak. The fact that V_6O_{13} is a lower oxide phases, and that it has formed epitaxially suggests V_4O_9 may be forming epitaxially to V_2O_5. There is no evidence of VO_2(M) forming epitaxially. This aligns with literature summarised in Chapter 3 as well as RSM measurements in section 5.4.1. Optical absorption of these phases in relevant parts of the RAS spectrum may be detectable, as examined in section 6.4.

6.3.3 V_6O_{13} & V_4O_9 RAS contributions

Using the relationship between similar RAS spectra observed and the composition of the annealed samples at these stages, RAS features can be qualitatively assigned to specific phases.

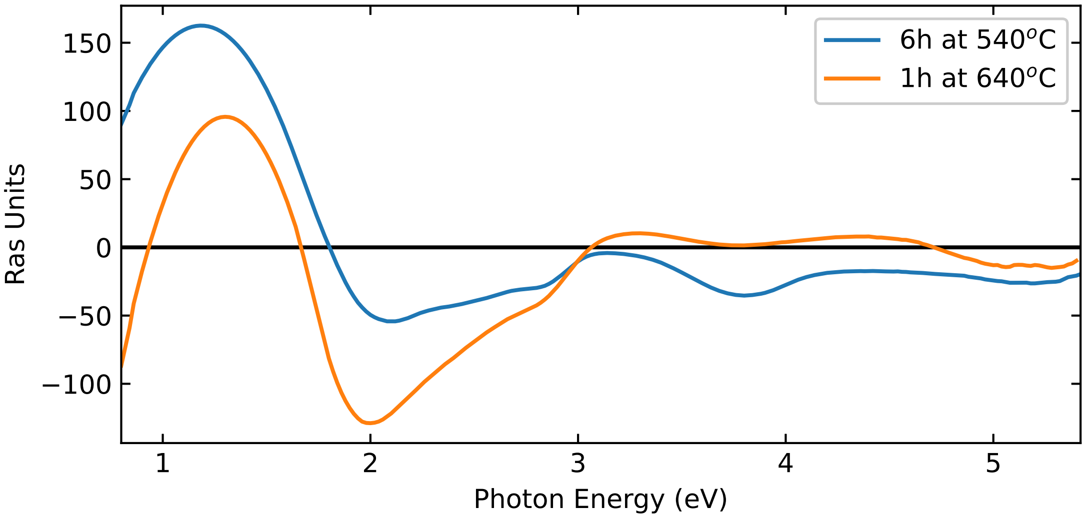

Figure 6.11: RAS of samples annealed at 800K and 900K compared. Patterns show very simular profiles.

The first example can be seen in early stages of annealing at 900K showing similarities to later stages of 800K annealing (figure 6.11). The feature between 0.8 eV and 2.5 eV stands in contrast to the V_2O_5 spectrum, which showed no features in this energy range other than a nearly constant RAS signal. The feature shows a maximum at $1.2 - 1.3$ eV and a minimum at $2 - -2.1$ eV. Comparing XRD spectra (figures 6.4 and 6.5) it is clear that both have very similar composition, both showing mainly V_2O_5(010) and V_6O_{13}(001) structures, with V_6O_{13}(010) accounting for additional peaks in the 800K sample. We therefore hypothesis this low energy feature is related to V_6O_{13}.

Further evidence can be built by examining optical data published in regard to V_6O_{13}. Van Hove *et al.* published the 45° incidence reflection spectrum and absorption spectrum of V_6O_{13} along the [100] and [010] directions in the range 0.2–3.2 eV [176]. We use the following equations to convert their data to the complex dielectric function (ϵ):

$$n_i = \frac{1-\sqrt{R_i}}{1+\sqrt{R_i}} \quad \kappa_i = \frac{\alpha_i}{E}.\frac{hc}{4\pi} \quad \epsilon_i^{'} = n_i^2 - \kappa_i^2 \quad \epsilon_i^{''} = 2n_i\kappa_i \tag{6.2}$$

n = real part of the refractive index, R = measured reflected intensity, κ = imaginary part of the refractive index, α = measured absorption constant, E = photon energy, h = Plank's constant, c = speed of light, $\epsilon^{'}$ = real part of the dielectric function, $\epsilon^{''}$ = imaginary part of the dielectric function.

Using eq. 6.1 a RAS spectrum for the V_6O_{13}(001) surface can be generated and is presented in figure 6.12. This spectrum has a maximum at 1.2 eV and a minimum at 2 eV, matching the features seen in our samples above. Based on these findings we conclude this feature seen in our samples is a V_6O_{13}(001) RAS feature.

As agreement between the generated RAS spectrum and the experimental results has been established, the dielectric function calculated from literature can be assumed to be accurate to some degree.

We also compare early stages of annealing at 800K with later stages of annealing at 700K seen in figure 6.13. The feature we focus on here between 2 eV and 3 eV, where the signal is negative in contrast to V_2O_5 but has maximum at 2.9 eV. Comparing XRD spectra of these samples shows they have many differences, particularly the acute V_6O_{13}(001) spectrum in the 800K sample being absent from the 700K sample. However, they share common features, V_4O_9(001). This XRD analysis aligns with what we observe in RAS, where the spectra diverge in the lower energy, where the V_6O_{13} peak was identified. Hence we propose that the negative signal in the IR, and positive maximum at 2.9 eV is in fact a V_4O_9(001) RAS feature.

Comparing RAS of sample 600K and the early RAS of sample 700K (figure 6.14),

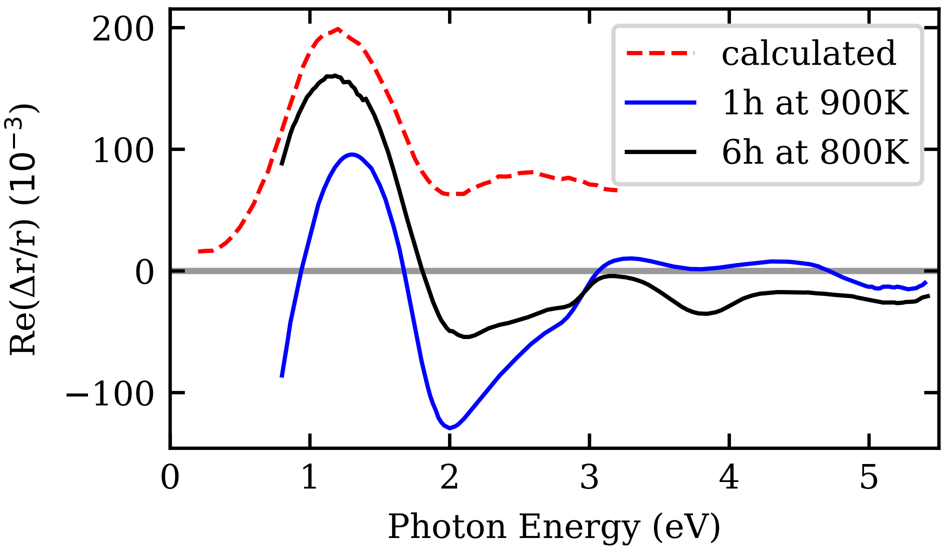

Figure 6.12: Simulation of V_6O_{13}(001) RAS spectrum based off optical data from literature [176]. Note the prominent positive feature at 1.2 eV as seen in measured data.

we see similarities again. 700K 20 m, and 600K 4 h and 6 h all show a negative RAS signal from 2 eV, a minimum at 2.8 eV and a maximum at 3 eV. Comparison with the V_2O_5 spectrum again show these features to be distinct. Both samples show V_4O_9(001), with sample 340 showing exclusively this surface besides V_2O_5(010). This contributes strong evidence towards the V_4O_9(001) RAS features.

V_4O_9 has been shown to be anisotropic in structure, however we are assuming that V_4O_9 has formed epitaxially in the reduction of V_2O_5, and that it will contribute an anisotropic reflection. Unlike V_6O_{13}, we have no literature available on structurally resolved dielectric functions of V_4O_9 to generate a predicted RAS spectrum. The RAS spectra combined with DFT can aid in the characterization of optical and electronic properties. A theoretical dielectric function can be generated and verified by comparing it to the predicted RAS spectrum. Using another method, estimations of the V_4O_9 layer thickness may be made using cross-sectional scanning electron microscopy. As the dielectric function of V_2O_5(010) is known, ellipsometry can be used to extract the optical properties of V_4O_9 which can be cross referenced against RAS measurements. These possibilities will be revisited in Chapter 7. Therefore RAS is a good technique to probe crystalline V_4O_9, which has not been synthesized as an isolated product.

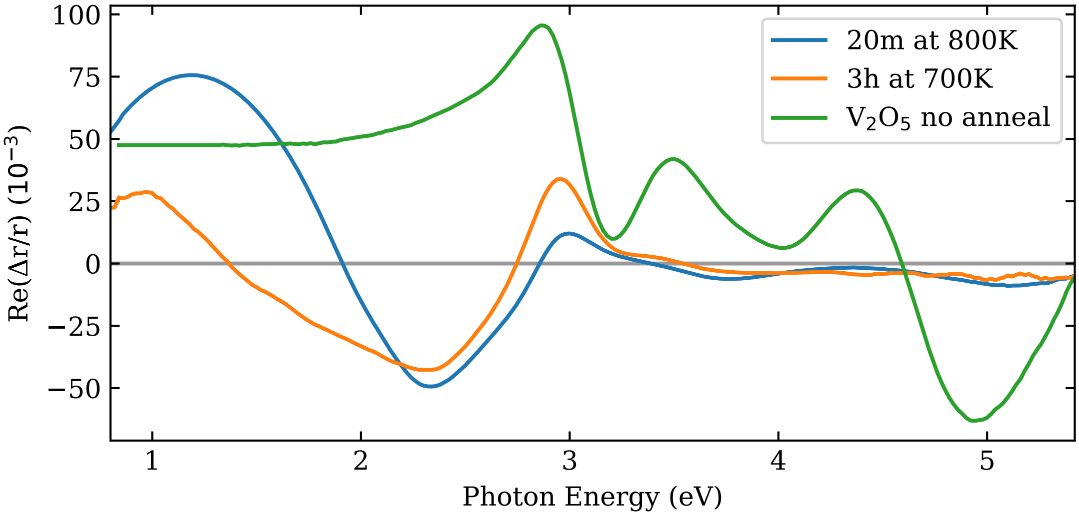

Figure 6.13: Comparison of RAS spectra of a pristine V_2O_5 surface as well as samples annealed at 800 K for 20 m and 700 K for 3 h.

6.4 RAS Measurements across the VO_2 and V_6O_{13} MIT

6.4.1 RAS across the VO_2 Transition

VO_2 undergoes a MIT at 340 K or 67 °C. Below the transition, the structure is monoclinic and insulating, while above it becomes rutile (orthorhombic) and metallic. Moving through the transition from the rutile phase, V ions form dimer pairs along the rutile [001] axis creating the monoclinic structure. The shift of ions causes crystal field splitting of the V-O orbitals resulting in a bandgap opening. Further details are presented in section 3.3.

VO_2 is popular amongst vanadium oxides due to its MIT being relatively accessible, and therefore useful for a range of applications. High quality VO_2 has been prepared via reduction methods; therefore finding an identifiable optical *in situ* probe for its presence is of particular importance when considering practical RAS application.

VO_2 has been shown to have anisotropic transport properties with a particular distinction between conductivity parallel and perpendicular to the a_m axis [177, 178]. This is due to the two distinct bands responsible for conduction in both phases; the $d_{\|}$ in the $[100]_m$ direction, and the π conduction bands perpendicular. Optical measurements show the anisotropy of the dielectric function and reflectively between axes to be small, but present [118, 179]. Therefore a RAS response can be expected for any VO_2(M) crystalline surface other than (100). A clearer change in optical properties over the transition is an increase in absorption in the 0–1 eV region [179, 180].

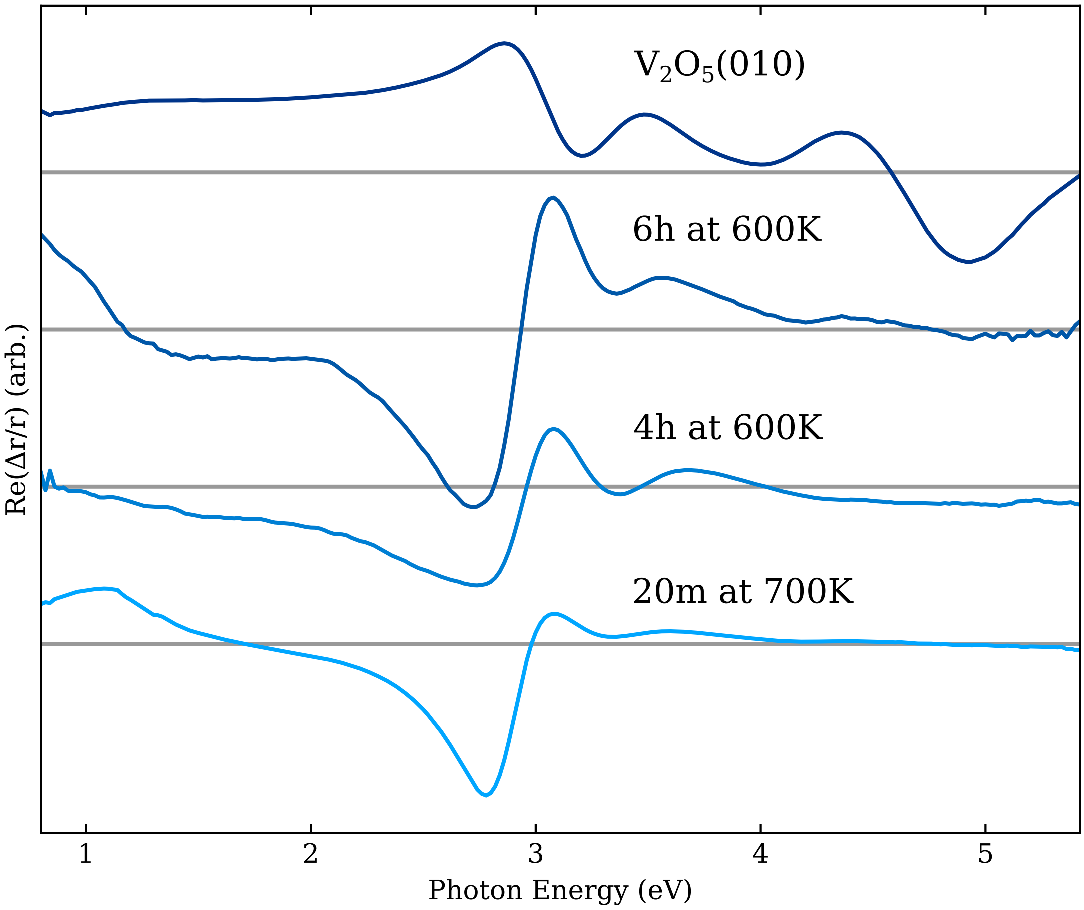

Figure 6.14: Comparison of RAS spectra of a pristine V_2O_5 surface as well as samples annealed at 700 K and 600 K over a range of time steps.

In order to establish VO_2's influence on the RAS spectra observed; RAS measurements have been made above and below the T_{MIT} of VO_2 in our mixed crystal system. Sample 800K, annealed for 6 h was selected due to an observable MIT and possible VO_2(M)(110) seen via XRD. No in-plane component of VO_2 could be found via XRD, suggesting the VO_2 may be polycrystalline, and therefore won't produce a RAS spectra. Due to the complex transformation of VO_2(B) to VO_2(R) as outlined in 3.6, polycrystalline VO_2(M) is expected. RSM measurements in 5.4.1 also suggest VO_2(M) in this system is polycrystaline. V_6O_{13} is also present in this sample.

Figure 6.15, shows the previously established V_6O_{13} feature with expected maximum at 1.2 eV as the sample is heated and cooled through 340 K. The RAS signal can be seen to decreases in the range 0.8–1.5 eV as the temperature increases, while no change is seen in the 1.5–2 eV region. The decrease in signal is attributed to the increased absorption of the metallic VO_2 phase in the IR [179, 180]. Figure 6.16 plots the RAS signal at 0.8 eV with changing temperature. The resulting hysteretic plot is characteristic of VO_2's first order transition.

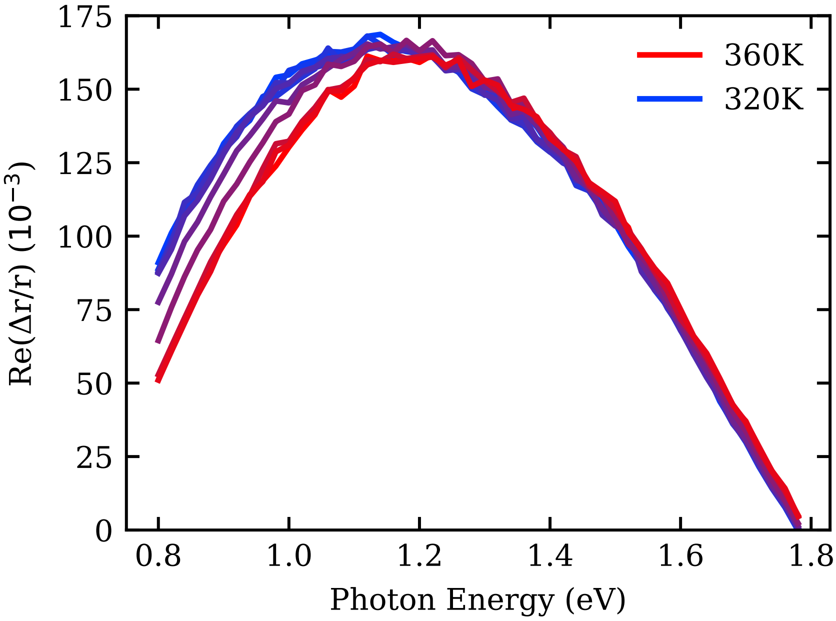

Figure 6.15: The V_6O_{13} RAS feature at 1.2 eV can be seen to shift in the lower energy ranges over the VO_2 MIT transition temperature range.

Despite this clear change in RAS signal, we see no evidence of VO_2 RAS features of its own, rather its effect on the RAS signals of other phases. From our experiments, reduction of V_2O_5 to VO_2 results in the presence of V_6O_{13} with its characteristic feature between 0.8–2.5 eV as seen in this sample, so *in situ* observation of this VO_2 signal is certainly still valuable in this context. Chapter 5 shows that a mixture of V_6O_{13} and VO_2 is required for the lower power switching. RAS in this context is a valuable measurement to enable more precise and repeatable formation of this low power switching layer.

6.4.2 RAS across the V_6O_{13} Transition

V_6O_{13} has a MIT at 150 K. Structurally, the change between metallic and insulating states is small. Detailed optical data above and below the transition published by Van Hove *et* al. (1980) [176] shows a large change in reflectively and absorbance of the (001) surface. The data also shows large anisotropy between measurements in the [100] and [010] directions.

Converting the data using eq. 6.2 and eq. 6.1, a comparison between RAS spectra above and below the V_6O_{13} MIT is seen in figure 6.17.

The same 800K sample described in 6.4.1 was placed in a cryostat apparatus as described in section 2.7.3, and RAS measurements were taken at a range of temperatures above and below 150 K.

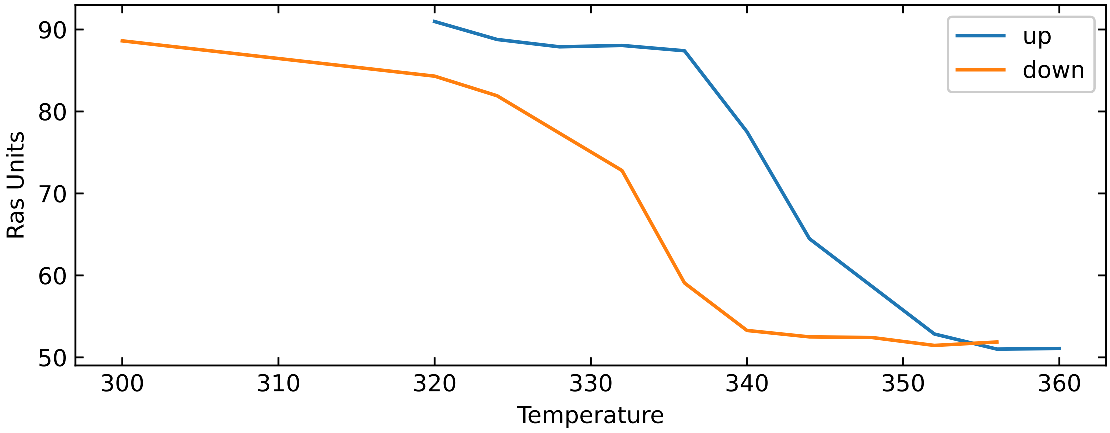

Figure 6.16: The chage in intensity of RAS signal at 0.8 eV with temperature in a sample containing VO_2 and V_6O_{13}. This pattern closely resembles a VO_2 MIT, with a transition and hysteresis around 340 K.

No clear feature could be seen changing throughout the temperature changes. Instead, figure 6.17 also shows the V_6O_{13} RAS spectrum at the maximum and minimum temperatures measured against the calculated data. Simularities can be seen between the our data and the calculated curves. The curves intersect and cross at simular energies. Despite this, it is difficult to say for certain that our data accurately captures the V_6O_{13} MIT effect on RAS measurements. A more specific energy change identified to change around 150 K would be preferable.

6.5 Conclusions

Optical anisotropy of bulk $V_2O_5(010)$ has been measured using RAS and ellipsometry. The measured RAS spectrum agrees with a theoretical spectrum generated using the dielectric function.

As we know, a higher temperature is reducing the V_2O_5 crystals quicker. Clearly in the early stages of high temperatures we have similarities to later stages of lower temperature. The three comparisons in section 6.3.3 show this. The reduction is clearly complex being related to the time but also critically the temperature, in the sense that very long anneals of one sample at a lower temperature will not produce the phases observed in samples at a higher temperature. RAS is sensitive to these progressions and can monitor reduction *in situ*.

Using RAS and XRD spectra of separate annealed V_2O_5 samples, a $V_6O_{13}(001)$ feature has been identified in the RAS spectrum. A theoretical spectrum again agrees with measurement. Additional features have also been identified and attributed to the $V_4O_9(001)$ surface.

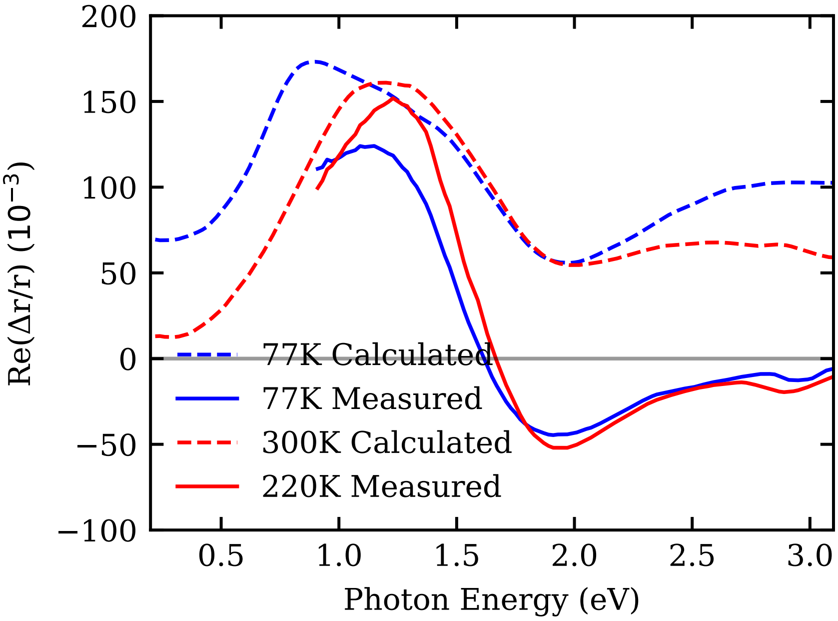

Figure 6.17: Calculated and measured RAS spectra above and below the V_6O_{13} MIT.

The changes in the RAS response across the MIT of VO_2 have been measured and attributed to increased absorbance of metallic VO_2 in the IR as opposed to an anisotropic reflective contribution. The results suggest that RAS can be used as a non-destructive and simple optical method to monitor vanadium oxide growth and preparation *in situ*.

RAS measurements across the V_6O_{13} MIT have also been taken, and although simularities between measured and calculated data can be seen, further experimention is needed to confirm specific RAS contributions from the V_6O_{13} MIT.

These newly identified features will enable practical use of the RAS technique in identifying vanadium oxide features. The implications and resulting potential future work of these findings will be discussed in Chapter 7.

7

Conclusions

In this work a study of vanadium dioxide, vanadium pentoxide and vanadium oxide Wadsley phases has been presented. The results can be split into three parts:

1. A method to manipulate the hysteresis of electric field induced MIT of VO_2 through the application of pulsed voltage signals to control material self-heating.
2. A VO_2-type e-MIT triggered by an anomalously low electric field, shown to be due to mixed phases in reduced V_2O_5 crystals.
3. The anisotropic optical response of $V_2O_5(010)$ & $V_6O_{13}(001)$ terminations investigated by RAS, as well as RAS contributions discovered for V_4O_9 and RAS signal alterations due to the MIT of VO_2.

In Chapter 4 a method to alter the hysteresis of VO_2 resistive switching (RS) was established. As Joule heating plays a role in the RS of the device, especially in the metallic state, a pulsed signal can change the amount of power applied to the material, increasing or decreasing the amount of heating taking place. If time between pulses is increased, less power is applied, less heating takes place and the voltage required to maintain a temperature above the MIT temperature rises. A mathematical model has been devised, tested and confirmed through simulation.

Chapter 5 saw the development of a mixed VO phase surface derived from annealing a V_2O_5 single crystal under vacuum. Under particular annealing conditions, a surface with an exceptionally low voltage-triggered VO_2-like MIT is induced.

Annealing experiments showed that the VO system derived from annealing V_2O_5 forms a complex system of phases. However, it is found that annealing at temperatures between 340–440 °C, no vanadium of 3+ valency is created, and only VO_2, V_2O_5 and Wadsley phases need to be considered. It is also found that annealing at 540 °C & 440 °C induced a surface with a VO_2-like MIT with a very low resistance, attributed to V_6O_{13} also present. Improvement in MIT characteristics (reduced switching width, reduced hysteresis, larger ratio of resistivities) is seen with longer anneal times.

RS experiments on a sample annealed at 540 °C for 16 h show a anomalously low threshold switching field for a VO_2 type transition as low as $425\,\mathrm{V\,m^{-1}}$ which is, to the best of the author's knowledge, considerably lower than anything reported in the literature. Joule heating is established as the only mechanism to induce this switch. This property is attributed to the low resistance insulating state of VO_2. The low resistance of this state is attributed to V_6O_{13} being present in the surface of the sample with VO_2. This allows the temperature of the channel to reach the VO_2 transition temperature with very little applied voltage.

TEM measurements show the annealed crystal does indeed compose of a V_2O_5 crystal VO_2 and V_6O_{13} grains.

Like Chapter 4, Chapter 5 sees development in manipulation of VO_2 MIT properties, this time by developing a mixed vanadium oxide material with novel and useful properties in respect to the same compounds in their isolated state. Alteration and control of MIT properties is particularly relevant to enable VO_2 technologies.

In Chapter 6, we apply RAS to the V_2O_5 and annealed V_2O_5 crystals. RAS is a useful *in-situ* characterisation technique, although measurements to the VO system have not been performed to date in literature.

The optical anisotropy of bulk $V_2O_5(010)$ has been measured using RAS and ellipsometry. The measured RAS spectrum shows agreement with a theoretical spectrum generated using the measured dielectric function found using ellipsometry. Using RAS and XRD spectra of multiple annealed V_2O_5 samples, a $V_6O_{13}(001)$ feature has been identified in the RAS spectrum. A simulated theoretical RA spectrum of V_6O_{13} derived from literature agrees with measurement. Additional features have also been identified and attributed to the $V_4O_9(001)$ surface, although no literature on the phase optical properties is available. The changes in the RAS response across the MIT of VO_2 and V_6O_{13} have also been investigated, and changes can be observed in the IR for the VO_2 transition, although V_6O_{13} MIT measurements provided no insight, and did not agree with literature.

These newly identified features will enable practical use of the RAS technique in identifying vanadium oxide phases during growth or reduction methods.

Taken together, these three chapters provide complementary findings in regards to the physics and applications of vanadium oxides. Chapter 4 provides insight into manipulating VO_2 devices through use of input signals, and shows the underlying Joule-heating mechanism. Chapter 5 sees a method to induce novel VO_2-type RS at very low electric fields through control of the material composition. Chapter 6 establishes a method to identify and control the composition of VO samples through the non-destructive *in-situ* technique of RAS. Each of these results adds to the potential of VO based electronics via tuning and alteration of material characteristics, and through *in-situ* identification of VO phases.

7.1 Future Work

The results presented in this thesis open new lines of enquiry. The following section will discuss direct experiments that result from the findings in this text. In addition, study of the VO system over the past number of years have highlighted avenues for further practical experimentation, which do not directly link to the work in this text. These will also be outlined.

7.1.1 Continued RAS Investigations

In Chapter 6, *ex-situ* RAS studies on VO crystals are presented. However, RAS is discussed as an ideal *in-situ* technique. Therefore an obvious continuation of this experiment is to perform *in-situ* characterisation while annealing V_2O_5 samples via RAS. This work would enable real-time observation of the chemical evolution of sample. Predictions and correlations between expected composition derived from the measured RAS signal and composition found experimentally via XRD and resistive measurements, would enable a true quantitative study of crystal development in respect to RAS. This will allow creation of a surface layer with optimised characteristics, such as a lower resistance or superior RS properties.

However, this experiment is difficult to implement. A specific sample stage within a vacuum system with a correctly positioned strain-free window is required. None the less, the execution of this experiment is being planned.

In another pathway for further experimentation, RAS spectra combined with DFT can aid in the characterization of optical and electronic properties. A theoretical dielectric function can be generated and verified by comparing it to the predicted RA spectrum. For example, V_4O_9 and VO_2(B) are all anisotropic phases without in-depth optical literature available. In this respect, RAS features can be used to inform theoretical optical spectra that are computationally simulated.

Using another method, estimations of layer thickness in our mixed phase system may be made using cross-sectional scanning electron microscopy or transmission electron microscopy. For example, in a sample annealed at 340 °C, only V_4O_9 and V_2O_5 are seen in the XRD measurements. As the dielectric function of V_2O_5(010) is known, ellipsometry can be used to extract the optical properties of V_4O_9 which can be cross referenced against RAS measurements. This method can be further applied to the other species present in the annealed V_2O_5 samples. Therefore RAS is a good technique to probe crystalline species which have not been synthesized as an isolated product.

Finally, RAS may be sensitive to the initial reduction of the V_2O_5 crystal. Oxygen vacancies can, in theory, generate features in the optical anisotropy. If vacant states – and RA feature – become present in the bandgap, RAS can be very sensitive to this. V_2O_5 itself shows no features in the IR due to its bandgap. In-situ, real-time measurements can examine the development of the vacancy structure.

7.1.2 Vanadium Dioxide

The findings related to VO_2 in this work center on furthering the physics expertise in respect to the electronic potential of the material. As stated previously, VO_2 is the most studied VO phase due to its large and relatively accessible MIT, and a large amount of focus has been on enabling the potential of VO_2.

The work in this text focuses on the VO_2 resistive switch (RS). The shape and magnitude, or profile, of the IV curve is clearly malleable. The ability to control the hysteresis, switching voltages, resistance and power applied all add to an arsenal to engineer a VO_2 material for practical application. The understanding in this work of the mechanisms driving these changes to the RS is of clear relevance.

However, the future potential of leveraging these findings may lie more with engineering groups with particular applications in mind. Future work in this vein would likely centre around using devices as fabricated in Chapter 4 in larger circuits and showing how the system dynamics can change by altering signal inputs or the resistance of the VO_2 channel.

However, a relevant aspect of the VO_2 transition has, to this authors knowledge, not been investigated. Through collaboration with groups in the University of Notre Dame, the problem of VO_2 device inconsistency has been highlighted. Even in very high quality VO_2 films with little variation in "macro-scale" characteristics, devices fabricated have varying electronic characteristics across the devices, with many not exhibiting RS properties. The applications under investigation require multiple identical devices to be achieved, so this variation is undesirable. To further reinforce this as an issue, it was found in Chapter 4 that a large number of devices fabricated on the same film did not show RS.

Investigations into this inconsistency are necessary to enable practical use of VO_2 devices. Potential sources of this problem include: (i) device fabrication inducing film changes, (ii) grain and defect structures on the film. Although qualitative studies have been performed [106], the field lacks accurate quantitative analysis into (ii).

Quantitative defect analysis may require specialised methods and techniques, however work similar to this has been performed previously [181], so an experimental outline to follow exists. This method relies on specialised scanning electron microscopy techniques. Extending this experimentation to examine how defects change MIT and RS properties should be possible.

To investigate changes from device fabrication, samples would be characterised before and after each fabrication step. It should be relatively straight forward to see indications of sample changes. Further investigations could leverage the same techniques as the defect study.

7.1.3 Wadsley Phases

This work has highlighted that the V_nO_{2n+1} system lacks a substantial amount of in-depth research. Basic material properties are unknown for many phases. For example, the resistivity of V_4O_9 and V_3O_7 has not been reported in literature. No optical characterisation of these materials has been performed. Publication of these basic properties would certainly be relevant, as it would have been beneficial to this work. Presumably other researchers have encountered the same issue. Therefore, fabrication of these compounds would be a worthwhile endeavour.

It has been highlighted that DFT simulations combined with RAS may be able to probe properties of these materials without fabricating the isolated phase, as well as SEM combined with ellipsometry so isolate the optical properties of particular phases.

7.1.4 Outlook

The realisation of MIT applications in electronics seems extremely feasible. The increasing density of Si technologies or "Moore's Law" cannot continue forever, or at least the cost of increasing semi-conductor device density will grow too high. It seems far more feasible that computation will diversify in terms of technology, and we will see machines made using different materials and methodologies to solve specific problems. Quantum computing or neural networking methodologies are good examples of this.

MIT technologies are another tool for computation. This author's experience has been in oscillator technologies, and their potential to solve non-linear problems quickly (eg. Ising machines which can find global minima and maxima very quickly) as well as image processing is clear. These are problems conventional computing architectures take much longer to solve.

Assuming VO_2 may be the material to dominate in MIT technologies may be naive, as materials with superior properties may not be available yet (larger switching ratio, smaller power consumption, tunable switching temperature, *etc.*). However, knowledge gained from studying VO_2 in-depth is likely going to be applicable to other MIT materials. For example, this text shows how Joule heating in the metallic phase of a device is relevant for its RS characteristics. This finding may be extended to MIT devices in general.

An interesting scenario to consider is V_6O_{13} as the primary MIT material. This study shows a method to reliably fabricate crystalline V_6O_{13} layers on V_2O_5 substrates via reduction with *in-situ* control to ensure material quality. One could envision a Si type fabrication process, where selectively treating layers of a V_2O_5 substrate may enable device architectures on the surface.

We hope this text can be considered as a relevant and helpful piece of literature to be added to this growing community and area of expertise.

Bibliography

[1] Matthew Brahlek, Lei Zhang, Jason Lapano, Hai-Tian Zhang, Roman Engel-Herbert, Nikhil Shukla, Suman Datta, Hanjong Paik, and Darrell G Schlom. Opportunities in vanadium-based strongly correlated electron systems. *MRS Communications*, 7(1):27–52, 2017.

[2] FJ Morin. Oxides which show a metal-to-insulator transition at the Neel temperature. *Physical Review Letters*, 3(1):34, 1959.

[3] Larry A. Ladd and William Paul. Optical and transport properties of high quality crystals of V_2O_4 near the metallic transition temperature. *Solid State Communications*, 7(4):425–428, February 1969.

[4] B Wu, A Zimmers, H Aubin, R Ghosh, Y Liu, and R Lopez. Electric-field-driven phase transition in vanadium dioxide. *Physical Review B*, 84(24):241410, 2011.

[5] J Laverock, ARH Preston, D Newby Jr, KE Smith, S Sallis, LFJ Piper, S Kittiwatanakul, JW Lu, SA Wolf, Mats Leandersson, et al. Photoemission evidence for crossover from Peierls-like to Mott-like transition in highly strained VO_2. *Physical Review B*, 86(19):195124, 2012.

[6] S Lysenko, V Vikhnin, F Fernandez, A Rua, and H Liu. Photoinduced insulator-to-metal phase transition in VO_2 crystalline films and model of dielectric susceptibility. *Physical Review B*, 75(7):075109, 2007.

[7] Masatoshi Imada, Atsushi Fujimori, and Yoshinori Tokura. Metal-insulator transitions. *Reviews of modern physics*, 70(4):1039, 1998.

[8] V Eyert. The metal-insulator transition of NbO_2: an embedded peierls instability. *EPL (Europhysics Letters)*, 58(6):851, 2002.

[9] Zheng Yang, Changhyun Ko, and Shriram Ramanathan. Oxide electronics utilizing ultrafast metal-insulator transitions. *Annual Review of Materials Research*, 41:337–367, 2011.

[10] You Zhou and Shriram Ramanathan. Mott memory and neuromorphic devices. *Proceedings of the IEEE*, 103(8):1289–1310, 2015.

[11] Kai Liu, Sangwook Lee, Shan Yang, Olivier Delaire, and Junqiao Wu. Recent progresses on physics and applications of vanadium dioxide. *Materials Today*, 21(8):875–896, 2018.

[12] N Shukla, S Datta, A Parihar, and A Raychowdhury. Computing with coupled relaxation oscillators. *Future Trends in Microelectronics: Journey into the Unknown*, pages 147–156, 2016.

[13] Eugene M Izhikevich. Computing with oscillators. *Neural Networks*, 5255:1–30, 2000.

[14] Hong Ye and Linshuang Long. Smart or not? A theoretical discussion on the smart regulation capacity of vanadium dioxide glazing. *Solar Energy Materials and Solar Cells*, 120:669–674, 2014.

[15] Yanfeng Gao, Hongjie Luo, Zongtao Zhang, Litao Kang, Zhang Chen, Jing Du, Minoru Kanehira, and Chuanxiang Cao. Nanoceramic VO_2 thermochromic smart glass: A review on progress in solution processing. *Nano Energy*, 1(2):221–246, 2012.

[16] A Zylbersztejn and N Mott. Metal-insulator transition in vanadium dioxide. *Physical Review B*, 11(11):4383, 1975.

[17] Joyeeta Nag and RF Haglund Jr. Synthesis of vanadium dioxide thin films and nanoparticles. *Journal of Physics: Condensed Matter*, 20(26):264016, 2008.

[18] J Haber, M Witko, and R Tokarz. Vanadium pentoxide I. structures and properties. *Applied Catalysis A: General*, 157(1-2):3–22, 1997.

[19] Katrien Devriendt, Hilde Poelman, and Lucien Fiermans. Thermal reduction of vanadium pentoxide: an XPD study. *Surface Science*, 433:734–739, 1999.

[20] XJ Wang, HD Li, YJ Fei, X Wang, YY Xiong, YX Nie, and KA Feng. XRD and Raman study of vanadium oxide thin films deposited on fused silica substrates by RF magnetron sputtering. *Applied Surface Science*, 177(1-2):8–14, 2001.

[21] Vidyasagar Devthade and Sangwook Lee. Synthesis of vanadium dioxide thin films and nanostructures. *Journal of Applied Physics*, 128(23):231101, 2020.

[22] Hanna A Dabkowska and Antoni B Dabkowski. Crystal growth of oxides by optical floating zone technique. In *Springer Handbook of Crystal Growth*, pages 367–391. Springer, 2010.

[23] Howard M Smith and AF Turner. Vacuum deposited thin films using a ruby laser. *Applied Optics*, 4(1):147–148, 1965.

[24] Kurt J. Lesker. Material deposition chart. `https://www.lesker.com/newweb/deposition_materials/materialdepositionchart.cfm?pgid=0`. Accessed: 28-12-21.

[25] Username: Hydrargyrum. Bragg's law. `https://en.wikipedia.org/wiki/Bragg%27s_law#/media/File:Bragg_diffraction_2.svg`. Accessed: 09-11-21.

[26] Miho Yasaka et al. X-ray thin-film measurement techniques. *The Rigaku Journal*, 26(2):1–9, 2010.

[27] Daragh Mullarkey. *Utilising Chromium-Based p-Type Transparent Conducting Oxides in Photovoltaic Devices.* PhD thesis, Trinity College Dublin, 2018.

[28] Lyman G Parratt. Surface studies of solids by total reflection of X-rays. *Physical Review*, 95(2):359, 1954.

[29] AA Fursina, RGS Sofin, IV Shvets, and D Natelson. Origin of hysteresis in resistive switching in magnetite is Joule heating. *Physical Review B*, 79(24):245131, 2009.

[30] Sebastian Volz, Rémi Carminati, P Chantrenne, S Dilhaire, S Gomez, N Trannoy, and G Tessier. *Microscale and nanoscale heat transfer.* Springer, 2007.

[31] Georges Hamaoui, Nicolas Horny, Cindy Lorena Gomez-Heredia, Jorge Andres Ramirez-Rincon, Jose Ordonez-Miranda, Corinne Champeaux, Frédéric Dumas-Bouchiat, Juan Jose Alvarado-Gil, Younes Ezzahri, Karl Joulain, et al. Thermophysical characterisation of VO_2 thin films hysteresis and its application in thermal rectification. *Scientific Reports*, 9(1):1–10, 2019.

[32] Alois Senefelder. *A Complete Course Of Lithography: Containing Clear and Explicit Instructions in All the Different Branches and Manners of that Art; Accompanied by Illustrative Specimens of Drawings; to which is Prefixed a History of Lithography, from Its Origin to the Present Time.* Ackermann, 1819.

[33] Peter Weaver. *The technique of lithography.* [London]: BT Batsford, 1964.

[34] John R Groves. Brief description of lithography. *Iowa Geological and Water Survey Guidebook*, pages 53–56, 2008.

[35] Takashi Ito and Shinji Okazaki. Pushing the limits of lithography. *Nature*, 406(6799):1027–1031, 2000.

[36] Brian Conor Walls. *Surface Studies of (110) Terminated Fe_3O_4 & $SrTiO_3$*. PhD thesis, Trinity College Dublin, 2018.

[37] CS Fadley. Basic concepts of X-ray photoelectron spectroscopy. *Electron spectroscopy: theory, techniques and applications*, 2:1–156, 1978.

[38] P Weightman, DS Martin, RJ Cole, and T Farrell. Reflection anisotropy spectroscopy. *Reports on Progress in Physics*, 68(6):1251, 2005.

[39] U Rossow, R Goldhahn, D Fuhrmann, and A Hangleiter. Reflectance difference spectroscopy RDS/RAS combined with spectroscopic ellipsometry for a quantitative analysis of optically anisotropic materials. *physica status solidi (b)*, 242(13):2617–2626, 2005.

[40] K Fleischer, Ruggero Verre, O Mauit, RGS Sofin, L Farrell, C Byrne, CM Smith, JF McGilp, and IV Shvets. Reflectance anisotropy spectroscopy of magnetite (110) surfaces. *Physical Review B*, 89(19):195118, 2014.

[41] S Bahrs, A Bruchhausen, AR Goñi, G Nieva, A Fainstein, K Fleischer, W Richter, and C Thomsen. Effect of light on the reflectance anisotropy and chain-oxygen related raman signal in untwinned, underdoped crystals of $YBa_2Cu_3O_7$ - δ. *Journal of Physics and Chemistry of Solids*, 67(1-3):340–343, 2006.

[42] DE Aspnes. Above-bandgap optical anisotropies in cubic semiconductors: A visible–near ultraviolet probe of surfaces. *Journal of Vacuum Science & Technology B: Microelectronics Processing and Phenomena*, 3(5):1498–1506, 1985.

[43] DE Aspnes. Analysis of modulation spectra of stratified media. *Journal of the Optical Society of America*, 63(11):1380–1390, 1973.

[44] Harland Tompkins and Eugene A Irene. *Handbook of ellipsometry.* William Andrew, 2005.

[45] John A Woollam, Blaine D Johs, Craig M Herzinger, James N Hilfiker, Ron A Synowicki, and Corey L Bungay. Overview of variable-angle spectroscopic ellipsometry (VASE): I. Basic theory and typical applications. In *Optical Metrology: A Critical Review*, volume 10294, page 1029402. International Society for Optics and Photonics, 1999.

[46] Ludwig Reimer. *Transmission electron microscopy: physics of image formation and microanalysis*, volume 36. Springer, 2013.

[47] Travis E Oliphant. Python for scientific computing. *Computing in Science & Engineering*, 9(3):10–20, 2007.

[48] Bushveld Minerals. About vanadium. `https://www.bushveldminerals.com/about-vanadium/`. Accessed: 14-05-2021.

[49] US Geological Survey. Mineral commodity summaries 2020: Vanadium data sheet. Government Printing Office, 2020.

[50] Vanadium - element information, properties and uses: Periodic table. Royal Society of Chemistry. Accessed: 14-05-2021.

[51] Eduard Hryha, Elin Rutqvist, and Lars Nyborg. Stoichiometric vanadium oxides studied by XPS. *Surface and interface analysis*, 44(8):1022–1025, 2012.

[52] RR Moskalyk and AM Alfantazi. Processing of vanadium: a review. *Minerals Engineering*, 16(9):793–805, 2003.

[53] Baoxiang Yang, Jinyong He, Guifang Zhang, and Jike Guo. Chapter 11 - Applications of vanadium in the steel industry. In *Vanadium*, pages 267–332. Elsevier, 2021.

[54] Aishwarya Parasuraman, Tuti Mariana Lim, Chris Menictas, and Maria Skyllas-Kazacos. Review of material research and development for vanadium redox flow battery applications. *Electrochimica Acta*, 101:27–40, 2013.

[55] AJ Merer, Gejian Huang, AS-C Cheung, and AW Taylor. New quartet and doublet electronic transitions in the near-infrared emission spectrum of VO. *Journal of Molecular Spectroscopy*, 125(2):465–503, 1987.

[56] RS Ram, PF Bernath, SP Davis, and AJ Merer. Fourier transform emission spectroscopy of a new 2Φ–12Δ system of VO. *Journal of Molecular Spectroscopy*, 211(2):279–283, 2002.

[57] Evangelos Miliordos and Aristides Mavridis. Electronic structure of vanadium oxide. neutral and charged species, $VO^{0,\pm}$. *The Journal of Physical Chemistry A*, 111(10):1953–1965, 2007.

[58] P Hansmann, A Toschi, G Sangiovanni, T Saha-Dasgupta, S Lupi, M Marsi, and K Held. Mott–hubbard transition in V_2O_3 revisited, 2013.

[59] PD Dernier and M Marezio. Crystal structure of the low-temperature antiferromagnetic phase of V_2O_3. *Physical Review B*, 2(9):3771, 1970.

[60] Nevill Mott. *Metal-insulator transitions.* CRC Press, 1974.

[61] Le Jiang, Yang Qu, Zhiyu Ren, Peng Yu, Dongdong Zhao, Wei Zhou, Lei Wang, and Honggang Fu. In-situ carbon-coated yolk–shell V_2O_3 microspheres for lithium-ion batteries. *ACS Applied Materials & Interfaces*, 7(3):1595–1601, 2015.

[62] Udo Schwingenschlögl and Volker Eyert. The vanadium Magnéli phases V_nO_{2n-1}. *Annalen der physik*, 13(9):475–510, 2004.

[63] Eun-Jung Park, Gwang-Hee Lee, Cheolho Yoon, and Dong-Wan Kim. Comparison of distribution and toxicity following repeated oral dosing of different vanadium oxide nanoparticles in mice. *Environmental Research*, 150:154–165, 2016.

[64] Apoorva Kulkarni, Goru Santosh Kumar, Jasmine Kaur, and Kulbhushan Tikoo. A comparative study of the toxicological aspects of vanadium pentoxide and vanadium oxide nanoparticles. *Inhalation Toxicology*, 26(13):772–788, 2014.

[65] John B Goodenough. Metallic oxides. *Progress in Solid State Chemistry*, 5:145–399, 1971.

[66] Volker Eyert. The metal-insulator transitions of VO_2: A band theoretical approach. *Annalen der Physik*, 11(9):650–704, 2002.

[67] Volker Eyert. VO_2: a novel view from band theory. *Physical Review Letters*, 107(1):016401, 2011.

[68] Shik Shin, S Suga, M Taniguchi, M Fujisawa, H Kanzaki, A Fujimori, H Daimon, Y Ueda, K Kosuge, and S Kachi. Vacuum-ultraviolet reflectance and photoemission study of the metal-insulator phase transitions in VO_2, V_6O_{13}, and V_2O_3. *Physical Review B*, 41(8):4993, 1990.

[69] Nikhil Shukla, Abhinav Parihar, Eugene Freeman, Hanjong Paik, Greg Stone, Vijaykrishnan Narayanan, Haidan Wen, Zhonghou Cai, Venkatraman Gopalan, Roman Engel-Herbert, et al. Synchronized charge oscillations in correlated electron systems. *Scientific Reports*, 4(1):1–6, 2014.

[70] Miguel Romera, Philippe Talatchian, Sumito Tsunegi, Flavio Abreu Araujo, Vincent Cros, Paolo Bortolotti, Juan Trastoy, Kay Yakushiji, Akio Fukushima, Hitoshi Kubota, et al. Vowel recognition with four coupled spin-torque nano-oscillators. *Nature*, 563(7730):230–234, 2018.

[71] Elisabetta Corti, Bernd Gotsmann, Kirsten Moselund, Igor Stolichnov, Adrian Ionescu, and Siegfried Karg. Resistive coupled VO_2 oscillators for image

recognition. In *2018 IEEE International Conference on Rebooting Computing (ICRC)*, pages 1–7. IEEE, 2018.

[72] S Dutta, A Khanna, J Gomez, K Ni, Z Toroczkai, and S Datta. Experimental demonstration of phase transition nano-oscillator based ising machine. In *2019 IEEE International Electron Devices Meeting (IEDM)*, pages 37–8. IEEE, 2019.

[73] Virginie Théry, Alexandre Boulle, Aurelian Crunteanu, Jean-Christophe Orlianges, Arnaud Beaumont, Richard Mayet, Amine Mennai, Françoise Cosset, Annie Bessaudou, and Marc Fabert. Structural and electrical properties of large area epitaxial VO_2 films grown by electron beam evaporation. *Journal of Applied Physics*, 121(5):055303, 2017.

[74] Hai-Tian Zhang, Lei Zhang, Debangshu Mukherjee, Yuan-Xia Zheng, Ryan C Haislmaier, Nasim Alem, and Roman Engel-Herbert. Wafer-scale growth of VO_2 thin films using a combinatorial approach. *Nature communications*, 6(1):1–8, 2015.

[75] J-C Valmalette and J-R Gavarri. High efficiency thermochromic VO_2(R) resulting from the irreversible transformation of VO_2(B). *Materials Science and Engineering: B*, 54(3):168–173, 1998.

[76] Yoshio Oka, Takeshi Yao, Naoichi Yamamoto, Yutaka Ueda, and Akihiko Hayashi. Phase transition and V4+–V4+ pairing in VO_2(B). *Journal of Solid State Chemistry*, 105(1):271–278, 1993.

[77] François Théobald, Robert Cabala, and Jean Bernard. Essai sur la structure de VO_2(B). *Journal of Solid State Chemistry*, 17(4):431–438, 1976.

[78] Serena A Corr, Madeleine Grossman, Yifeng Shi, Kevin R Heier, Galen D Stucky, and Ram Seshadri. VO_2(B) nanorods: solvothermal preparation, electrical properties, and conversion to rutile VO_2 and V_2O_3. *Journal of Materials Chemistry*, 19(25):4362–4367, 2009.

[79] Amar Srivastava, Helene Rotella, Surajit Saha, Banabir Pal, Gopinadhan Kalon, Sinu Mathew, Mallikarjuna Motapothula, Michal Dykas, Ping Yang, Eiji Okunishi, et al. Selective growth of single phase VO_2 (A, B, and M) polymorph thin films. *APL materials*, 3(2):026101, 2015.

[80] Ziyauddin Khan, Prem Singh, Sajid Ali Ansari, Sai Rashmi Manippady, Amit Jaiswal, and Manav Saxena. VO_2 nanostructures for batteries and supercapacitors: A review. *Small*, 17(4):2006651, 2021.

[81] Nevill F Mott. Metal-insulator transition. *Reviews of Modern Physics*, 40(4):677, 1968.

[82] K Miyano, T Tanaka, Y Tomioka, and Y Tokura. Photoinduced insulator-to-metal transition in a perovskite manganite. *Physical Review Letters*, 78(22):4257, 1997.

[83] J Cao, Elif Ertekin, Varadharajan Srinivasan, W Fan, S Huang, H Zheng, JWL Yim, DR Khanal, DF Ogletree, JC Grossman, et al. Strain engineering and one-dimensional organization of metal–insulator domains in single-crystal vanadium dioxide beams. *Nature Nanotechnology*, 4(11):732–737, 2009.

[84] Sungbae Lee, Alexandra Fursina, John T Mayo, Cafer T Yavuz, Vicki L Colvin, RG Sumesh Sofin, Igor V Shvets, and Douglas Natelson. Electrically driven phase transition in magnetite nanostructures. *Nature materials*, 7(2):130–133, 2008.

[85] R Müller, R Naulaerts, J Billen, Jan Genoe, and Paul Heremans. CuTCNQ resistive nonvolatile memories with a noble metal bottom electrode. *Applied Physics Letters*, 90(6):063503, 2007.

[86] EJW Verwey. Electronic conduction of magnetite (Fe_3O_4) and its transition point at low temperatures. *Nature*, 144(3642):327–328, 1939.

[87] DC Kim, S Seo, SE Ahn, D-S Suh, MJ Lee, B-H Park, IK Yoo, IG Baek, H-J Kim, EK Yim, et al. Electrical observations of filamentary conductions for the resistive memory switching in NiO films. *Applied Physics Letters*, 88(20):202102, 2006.

[88] AS Barker Jr, HW Verleur, and HJ Guggenheim. Infrared optical properties of vanadium dioxide above and below the transition temperature. *Physical Review Letters*, 17(26):1286, 1966.

[89] Sukeji Kachi, Koji Kosuge, and Hideyuki Okinaka. Metal-insulator transition in V_nO_{2n-1}. *Journal of Solid State Chemistry*, 6(2):258–270, 1973.

[90] W Burkhardt, T Christmann, S Franke, W Kriegseis, D Meister, BK Meyer, W Niessner, D Schalch, and A Scharmann. Tungsten and fluorine co-doping of VO_2 films. *Thin Solid Films*, 402(1-2):226–231, 2002.

[91] John B Goodenough. The two components of the crystallographic transition in VO_2. *Journal of Solid State Chemistry*, 3(4):490–500, 1971.

[92] Nevill F Mott. The basis of the electron theory of metals, with special reference to the transition metals. *Proceedings of the Physical Society. Section A*, 62(7):416, 1949.

[93] John Hubbard. Electron correlations in narrow energy bands. *Proceedings of the Royal Society of London. Series A. Mathematical and Physical Sciences*, 276(1365):238–257, 1963.

[94] R Peierls. 2.3 Peierls Transition. In *More Surprises in Theoretical Physics*, page 27–30. Princeton Univ. Press, 1991.

[95] Luciana Vidas, Daniel Schick, Elías Martínez, Daniel Perez-Salinas, Alberto Ramos-Álvarez, Simon Cichy, Sergi Batlle-Porro, Allan S Johnson, Kent A Hallman, Richard F Haglund Jr, et al. Does VO_2 host a transient monoclinic metallic phase? *Physical Review X*, 10(3):031047, 2020.

[96] Galo J Paez, Christopher N Singh, Matthew J Wahila, Keith E Tirpak, Nicholas F Quackenbush, Shawn Sallis, Hanjong Paik, Yufeng Liang, Darrell G Schlom, Tien-Lin Lee, et al. Simultaneous structural and electronic transitions in epitaxial $VO_2/TiO_2(001)$. *Physical Review Letters*, 124(19):196402, 2020.

[97] A. I. Ivon, V. R. Kolbunov, and I. M. Chernenko. Stability of electrical properties of vanadium dioxide based ceramics. *Journal of the European Ceramic Society*, 19(10):1883–1888, August 1999.

[98] Jie Jian, Aiping Chen, Youxing Chen, Xinghang Zhang, and Haiyan Wang. Roles of strain and domain boundaries on the phase transition stability of VO_2 thin films. *Applied Physics Letters*, 111(15):153102, October 2017.

[99] Jae Yong Suh, Rene Lopez, Leonard C Feldman, and RF Haglund Jr. Semiconductor to metal phase transition in the nucleation and growth of VO_2 nanoparticles and thin films. *Journal of Applied Physics*, 96(2):1209–1213, 2004.

[100] D Brassard, S Fourmaux, M Jean-Jacques, JC Kieffer, and MA El Khakani. Grain size effect on the semiconductor-metal phase transition characteristics of magnetron-sputtered VO_2 thin films. *Applied Physics Letters*, 87(5):051910, 2005.

[101] Hanjong Paik, Jarrett A Moyer, Timothy Spila, Joshua W Tashman, Julia A Mundy, Eugene Freeman, Nikhil Shukla, Jason M Lapano, Roman Engel-Herbert, Willi Zander, et al. Transport properties of ultra-thin VO_2 films on (001) TiO_2 grown by reactive molecular-beam epitaxy. *Applied Physics Letters*, 107(16):163101, 2015.

[102] Kazuki Nagashima, Takeshi Yanagida, Hidekazu Tanaka, and Tomoji Kawai. Stress relaxation effect on transport properties of strained vanadium dioxide epitaxial thin films. *Physical Review B*, 74(17):172106, 2006.

[103] Zhen Zhang, Fan Zuo, Chenghao Wan, Aveek Dutta, Jongbum Kim, Jura Rensberg, Ronny Nawrodt, Helen Hejin Park, Thomas J Larrabee, Xiaofei Guan, et al. Evolution of metallicity in vanadium dioxide by creation of oxygen vacancies. *Physical Review Applied*, 7(3):034008, 2017.

[104] Xiaogang Tan, Tao Yao, Ran Long, Zhihu Sun, Yajuan Feng, Hao Cheng, Xun Yuan, Wenqing Zhang, Qinghua Liu, Changzheng Wu, et al. Unraveling metal-insulator transition mechanism of VO_2 triggered by tungsten doping. *Scientific Reports*, 2(1):1–6, 2012.

[105] L. L. Fan, S. Chen, G. M. Liao, Y. L. Chen, H. Ren, and C. W. Zou. Comprehensive studies of interfacial strain and oxygen vacancy on metal–insulator transition of VO_2 film. *Journal of Physics: Condensed Matter*, 28(25):255002, May 2016.

[106] J Narayan and VM Bhosle. Phase transition and critical issues in structure-property correlations of vanadium oxide. *Journal of Applied Physics*, 100(10):103524, 2006.

[107] Zewei Shao, Xun Cao, Hongjie Luo, and Ping Jin. Recent progress in the phase-transition mechanism and modulation of vanadium dioxide materials. *NPG Asia Materials*, 10(7):581–605, 2018.

[108] Guillermo Guzman, Fabien Beteille, Roger Morineau, and Jacques Livage. Electrical switching in VO_2 sol–gel films. *J. Mater. Chem.*, 6(3):505–506, 1996.

[109] Bongjin Simon Mun, Joonseok Yoon, Sung-Kwan Mo, Kai Chen, Nobumichi Tamura, Catherine Dejoie, Martin Kunz, Zhi Liu, Changwoo Park, Kyungsun Moon, and Honglyoul Ju. Role of Joule heating effect and bulk-surface phases in voltage-driven metal-insulator transition in VO_2 crystal. *Applied Physics Letters*, 103(6):061902, August 2013.

[110] Joonseok Yoon, Giyong Lee, Changwoo Park, Bongjin Simon Mun, and Honglyoul Ju. Investigation of length-dependent characteristics of the voltage-induced metal insulator transition in VO_2 film devices. *Applied Physics Letters*, 105(8):083503, August 2014.

[111] Dasheng Li, Abhishek A. Sharma, Darshil K. Gala, Nikhil Shukla, Hanjong Paik, Suman Datta, Darrell G. Schlom, James A. Bain, and Marek Skowronski.

Joule heating-induced metal–insulator transition in epitaxial VO_2/TiO_2 devices. *ACS Applied Materials & Interfaces*, 8(20):12908–12914, May 2016.

[112] G. M. Liao, S. Chen, L. L. Fan, Y. L. Chen, X. Q. Wang, H. Ren, Z. M. Zhang, and C. W. Zou. Dynamically tracking the Joule heating effect on the voltage induced metal-insulator transition in VO_2 crystal film. *AIP Advances*, 6(4):045014, April 2016.

[113] A Zimmers, L Aigouy, M Mortier, A Sharoni, Siming Wang, KG West, JG Ramirez, and Ivan K Schuller. Role of thermal heating on the voltage induced insulator-metal transition in VO_2. *Physical Review Letters*, 110(5):056601, 2013.

[114] Jonathan Leroy, Aurelian Crunteanu, Annie Bessaudou, Françoise Cosset, Corinne Champeaux, and J-C Orlianges. High-speed metal-insulator transition in vanadium dioxide films induced by an electrical pulsed voltage over nano-gap electrodes. *Applied Physics Letters*, 100(21):213507, 2012.

[115] Iuliana P Radu, B Govoreanu, S Mertens, X Shi, M Cantoro, M Schaekers, M Jurczak, Stefan De Gendt, Andre Stesmans, JA Kittl, et al. Switching mechanism in two-terminal vanadium dioxide devices. *Nanotechnology*, 26(16):165202, 2015.

[116] Alexander Pergament, Aurelian Crunteanu, Arnaud Beaumont, and G Stefanovich. Vanadium dioxide: Metal-insulator transition, electrical switching and oscillations. a review of state of the art and recent progress. In *EMN Meeting on Computation and Theory, Energy Materials and Nanotechnology, November 9 to 12, 2015, Istanbul, Turkey*, 2015. arXiv:1601.06246.

[117] R Enjalbert and J Galy. A refinement of the structure of V_2O_5. *Acta Crystallographica Section C: Crystal Structure Communications*, 42(11):1467–1469, 1986.

[118] JC Parker, DJ Lam, Y-N Xu, and WY Ching. Optical properties of vanadium pentoxide determined from ellipsometry and band-structure calculations. *Physical Review B*, 42(8):5289, 1990.

[119] W Lambrecht, B Djafari-Rouhani, and J Vennik. On the origin of the split-off conduction bands in V_2O_5. *Journal of Physics C: Solid State Physics*, 14(32):4785, 1981.

[120] Douglas K Louie. *Handbook of sulphuric acid manufacturing*. DKL Engineering, Inc., 2005.

[121] D Manno, A Serra, M Di Giulio, G Micocci, A Taurino, A Tepore, and D Berti. Structural and electrical properties of sputtered vanadium oxide thin films for applications as gas sensing material. *Journal of Applied Physics*, 81(6):2709–2714, 1997.

[122] Yuan Yue and Hong Liang. Micro-and nano-structured vanadium pentoxide (V_2O_5) for electrodes of lithium-ion batteries. *Advanced Energy Materials*, 7(17):1602545, 2017.

[123] An-Min Cao, Jin-Song Hu, Han-Pu Liang, and Li-Jun Wan. Self-assembled vanadium pentoxide (V_2O_5) hollow microspheres from nanorods and their application in lithium-ion batteries. *Angewandte Chemie International Edition*, 44(28):4391–4395, 2005.

[124] H Katzke, P Tolédano, and W Depmeier. Theory of morphotropic transformations in vanadium oxides. *Physical Review B*, 68(2):024109, 2003.

[125] Masanobu Saeki, Noboru Kimizuka, Motohiko Ishii, Isao Kawada, Mitsuko Nakano, Akio Ichinose, and Mitsuoki Nakahira. Crystal growth of V_6O_{13}. *Journal of Crystal Growth*, 18(1):101–102, 1973.

[126] Jonas Höwing, Torbjörn Gustafsson, and John O Thomas. Low-temperature structure of V_6O_{13}. *Acta Crystallographica Section B: Structural Science*, 59(6):747–752, 2003.

[127] K Kawashima, Y Ueda, K Kosuge, and S Kachi. Crystal growth and some electric properties of V_6O_{13}. *Journal of Crystal Growth*, 26(2):321–322, 1974.

[128] AC Gossard, FJ Di Salvo, LC Erich, JP Remeika, H Yasuoka, K Kosuge, and S Kachi. Microscopic magnetic properties of vanadium oxides. II. V_3O_5, V_5O_9, V_6O_{11}, and V_6O_{13}. *Physical Review B*, 10(10):4178, 1974.

[129] K West, B Zachau-Christiansen, T Jacobsen, and S Atlung. V_6O_{13} as cathode material for lithium cells. *Journal of Power sources*, 14(1-3):235–245, 1985.

[130] Satoshi Yamazaki, Chang Li, Kenji Ohoyama, Masakazu Nishi, Masaki Ichihara, Hiroaki Ueda, and Yutaka Ueda. Synthesis, structure and magnetic properties of V_4O_9 — a missing link in binary vanadium oxides. *Journal of Solid State Chemistry*, 183(7):1496–1503, 2010.

[131] KJELL Waltersson, BERTIL Forslund, K-A Wilhelmi, S Andersson, and J Galy. The crystal structure of V_3O_7. *Acta Crystallographica Section B: Structural Crystallography and Crystal Chemistry*, 30(11):2644–2652, 1974.

[132] A Gorenstein, A Khelfa, JP Guesdon, GA Nazri, OM Hussain, I Ivanov, and C Julien. The growth and electrochemical properties of V_6O_{13} flash-evaporated films. *Solid State Ionics*, 76(1-2):133–141, 1995.

[133] Armando Rúa, Félix E Fernández, Rafmag Cabrera, and Nelson Sepúlveda. Young's modulus of pulsed-laser deposited V_6O_{13} thin films. *Journal of Applied Physics*, 105(11):113504, 2009.

[134] R.L. Remke, R.M. Walser, and R.W. Bené. Transition layers between VO_2 films and oxide substrates. *Thin Solid Films*, 61(1):73–82, July 1979.

[135] C. V. Ramana, S. Utsunomiya, R. C. Ewing, and U. Becker. Formation of V_2O_3 nanocrystals by thermal reduction of V_2O_5 thin films. *Solid State Communications*, 137(12):645–649, March 2006.

[136] MN Colpaert, P Clauws, L Fiermans, and J Vennik. Thermal and low energy electron bombardment induced oxygen loss of V_2O_5 single crystals: Transition into V_6O_{13}. *Surface Science*, 36(2):513–525, 1973.

[137] O. Monfort, T. Roch, L. Satrapinskyy, M. Gregor, T. Plecenik, A. Plecenik, and G. Plesch. Reduction of V_2O_5 thin films deposited by aqueous sol–gel method to VO_2(B) and investigation of its photocatalytic activity. *Applied Surface Science*, 322:21–27, December 2014.

[138] Songhee Choi, Jaeseok Son, et al. Sharp contrast in the electrical and optical properties of vanadium wadsley (V_mO_{2m+1}, m > 1) epitaxial films selectively stabilized on (111)-oriented y-stabilized ZrO_2. *Physical Review Materials*, 3(6):063401, 2019.

[139] M Benkahoul, MK Zayed, A Solieman, and SN Alamri. Spray deposition of V_4O_9 and V_2O_5 thin films and post-annealing formation of thermochromic VO_2. *Journal of Alloys and Compounds*, 704:760–768, 2017.

[140] G Grymonprez, L Fiermans, and J Venink. Structural properties of vanadium oxides. *Acta Crystallographica Section A: Crystal Physics, Diffraction, Theoretical and General Crystallography*, 33(5):834–837, 1977.

[141] Ch Leroux, G Nihoul, and G Van Tendeloo. From VO_2(B) to VO_2(R): Theoretical structures of VO_2 polymorphs and in-situ electron microscopy. *Physical Review B*, 57(9):5111, 1998.

[142] J Haemers, E Baetens, and J Vennik. On the electrical conductivity of V_2O_5 single crystals. *physica status solidi (a)*, 20(1):381–386, 1973.

[143] Grace Baysinger, Lev I Berger, RN Goldberg, HV Kehiaian, K Kuchitsu, G Rosenblatt, DL Roth, and D Zwillinger. CRC handbook of chemistry and physics, 96th edition. *National Institute of Standards and Technology*, 2015.

[144] I Kawada, M Ishii, M Saeki, N Kimizuka, M Nakano-Onoda, and K Kato. Structural re-investigation of the low-temperature phase of V_6O_{13}. *Acta Crystallographica Section B: Structural Crystallography and Crystal Chemistry*, 34(3):1037–1039, 1978.

[145] Songhee Choi, Gihyeon Ahn, Soon Jae Moon, and Shinbuhm Lee. Tunable resistivity of correlated VO_2(A) and VO_2(B) via tungsten doping. *Scientific Reports*, 10(1):1–8, 2020.

[146] VN Andreev and VA Klimov. Electrical conductivity of the semiconducting phase in vanadium dioxide single crystals. *Physics of the Solid State*, 49(12):2251–2255, 2007.

[147] DH Kim and Hoi Sing Kwok. Pulsed laser deposition of VO_2 thin films. *Applied Physics Letters*, 65(25):3188–3190, 1994.

[148] You Zhou and Shriram Ramanathan. Mott memory and neuromorphic devices. *Proceedings of the IEEE*, 103(8):1289–1310, 2015.

[149] BJ Choi, Doo Seok Jeong, SK Kim, C Rohde, S Choi, JH Oh, HJ Kim, CS Hwang, K Szot, R Waser, et al. Resistive switching mechanism of TiO_2 thin films grown by atomic-layer deposition. *Journal of Applied Physics*, 98(3):033715, 2005.

[150] LL Fan, YF Wu, C Si, GQ Pan, CW Zou, and ZY Wu. Synchrotron radiation study of VO_2 crystal film epitaxial growth on sapphire substrate with intrinsic multi-domains. *Applied Physics Letters*, 102(1):011604, 2013.

[151] ZP Wu, S Yamamoto, A Miyashita, ZJ Zhang, K Narumi, and H Naramoto. Single-crystalline epitaxy and twinned structure of vanadium dioxide thin film on (0001) sapphire. *Journal of Physics: Condensed Matter*, 10(48):L765, 1998.

[152] YX Guo, YF Liu, CW Zou, ZM Qi, YY Wang, YQ Xu, XL Wang, F Zhang, and R Zhou. Oxygen pressure induced structure, morphology and phase-transition for VO_2/c-sapphire films by PLD. *Applied Physics A*, 115(4):1245–1250, 2014.

[153] G Garry, O Durand, and A Lordereau. Structural, electrical and optical properties of pulsed laser deposited VO_2 thin films on r-and c-sapphire planes. *Thin Solid Films*, 453:427–430, 2004.

[154] John Rozen, René Lopez, Richard F Haglund Jr, and Leonard C Feldman. Two-dimensional current percolation in nanocrystalline vanadium dioxide films. *Applied Physics Letters*, 88(8):081902, 2006.

[155] Eugene Freeman, Greg Stone, Nikhil Shukla, Hanjong Paik, Jarrett A Moyer, Zhonghou Cai, Haidan Wen, Roman Engel-Herbert, Darrell G Schlom, Venkatraman Gopalan, et al. Nanoscale structural evolution of electrically driven insulator to metal transition in vanadium dioxide. *Applied Physics Letters*, 103(26):263109, 2013.

[156] James F Shackelford, Young-Hwan Han, Sukyoung Kim, and Se-Hun Kwon. *CRC materials science and engineering handbook*. CRC press, 2016.

[157] Shin Buhm Lee, Kwangwoo Kim, Ji Seop Oh, Byungnam Kahng, and Jae Sung Lee. Origin of variation in switching voltages in threshold-switching phenomena of VO_2 thin films. *Applied Physics Letters*, 102(6):063501, 2013.

[158] Malcolm W Chase Jr. Nist-janaf thermochemical tables. *J. Phys. Chem. Ref. Data, Monograph*, 9, 1998.

[159] Anatoly G Shabalin, Javier Del Valle, Nelson Hua, Mathew J Cherukara, Martin V Holt, Ivan K Schuller, and Oleg G Shpyrko. Nanoscale imaging and control of volatile and non-volatile resistive switching in VO_2. *Small*, 16(50):2005439, 2020.

[160] R. Enjalbert and J. Galy. A refinement of the structure of V_2O_5. *Acta Crystallographica Section C Crystal Structure Communications*, 42(11):1467–1469, November 1986.

[161] Jun Ge and Mohamed Chaker. Oxygen vacancies control transition of resistive switching mode in single-crystal TiO_2 memory device. *ACS Applied Materials & Interfaces*, 9(19):16327–16334, 2017.

[162] Geert Silversmit, Diederik Depla, Hilde Poelman, Guy B. Marin, and Roger De Gryse. Determination of the V2p XPS binding energies for different vanadium oxidation states (V5+ to V0+). *Journal of Electron Spectroscopy and Related Phenomena*, 135(2-3):167–175, April 2004.

[163] E. Hryha, E. Rutqvist, and L. Nyborg. Stoichiometric vanadium oxides studied by XPS. *Surface and Interface Analysis*, 44(8):1022–1025, October 2011.

[164] Satoshi Yamazaki, Chang Li, Kenji Ohoyama, Masakazu Nishi, Masaki Ichihara, Hiroaki Ueda, and Yutaka Ueda. Synthesis, structure and magnetic properties

of V_4O_9—a missing link in binary vanadium oxides. *Journal of Solid State Chemistry*, 183(7):1496–1503, July 2010.

[165] R.J.D. Tilley and B.G. Hyde. An electron microscopic investigation of the decomposition of V_2O_5. *Journal of Physics and Chemistry of Solids*, 31(7):1613–1619, July 1970.

[166] M. N. Colpaert, P. Clauws, L. Fiermans, and J. Vennik. Thermal and low energy electron bombardment induced oxygen loss of V_2O_5 single crystals: Transition into V_6O_{13}. *Surface Science*, 36(2):513–525, May 1973.

[167] K. Devriendt, H. Poelman, and L. Fiermans. Thermal reduction of vanadium pentoxide: an XPD study. *Surface Science*, 433-435:734–739, August 1999.

[168] B. Wu, A. Zimmers, H. Aubin, R. Ghosh, Y. Liu, and R. Lopez. Electric-field-driven phase transition in vanadium dioxide. *Physical Review B*, 84(24):241410, December 2011.

[169] Byung-Gyu Chae, Hyun-Tak Kim, Doo-Hyeb Youn, and Kwang-Yong Kang. Abrupt metal–insulator transition observed in VO_2 thin films induced by a switching voltage pulse. *Physica B: Condensed Matter*, 369(1-4):76–80, December 2005.

[170] W. Brückner, W. Moldenhauer, H. Wich, E. Wolf, H. Oppermann, U. Gerlach, and W. Reichelt. The range of homogeneity of VO_2 and the influence of the composition on the physical properties. II. the change of the physical properties in the range of homogeneity. *Physica Status Solidi (a)*, 29(1):63–70, May 1975.

[171] Sangwook Lee, Kedar Hippalgaonkar, Fan Yang, Jiawang Hong, Changhyun Ko, Joonki Suh, Kai Liu, Kevin Wang, Jeffrey J. Urban, Xiang Zhang, Chris Dames, Sean A. Hartnoll, Olivier Delaire, and Junqiao Wu. Anomalously low electronic thermal conductivity in metallic vanadium dioxide. *Science*, 355(6323):371–374, January 2017.

[172] R. Santos, J. Loureiro, A. Nogueira, E. Elangovan, J.V. Pinto, J.P. Veiga, T. Busani, E. Fortunato, R. Martins, and I. Ferreira. Thermoelectric properties of V_2O_5 thin films deposited by thermal evaporation. *Applied Surface Science*, 282:590–594, October 2013.

[173] W. R. Thurber and A. J. H. Mante. Thermal conductivity and thermoelectric power of rutile (TiO_2). *Physical Review*, 139(5A):A1655–A1665, August 1965.

[174] VG Mokerov, VL Makarov, VB Tulvinskii, and AR Begishev. Optical properties of vanadium pentoxide in the region of photon energies from 2 eV to 14 eV. *Opt. Spectrosc.(USSR)(Engl. Transl.);(United States)*, 40(1), 1976.

[175] Chiranjivi Lamsal and NM Ravindra. Optical properties of vanadium oxides-an analysis. *Journal of Materials Science*, 48(18):6341–6351, 2013.

[176] W Van Hove, P Clauws, and J Vennik. Optical properties of V_6O_{13} single crystals in the metallic and the semiconducting phase. *Solid State Communications*, 33(1):11–16, 1980.

[177] CR Everhart and JB MacChesney. Anisotropy in the electrical resistivity of vanadium dioxide single crystals. *Journal of Applied Physics*, 39(6):2872–2874, 1968.

[178] TJ Huffman, Peng Xu, MM Qazilbash, EJ Walter, H Krakauer, Jiang Wei, DH Cobden, HA Bechtel, MC Martin, GL Carr, et al. Anisotropic infrared response of vanadium dioxide microcrystals. *Physical Review B*, 87(11):115121, 2013.

[179] Hans W Verleur, AS Barker Jr, and CN Berglund. Optical properties of VO_2 between 0.25 and 5 eV. *Physical Review*, 172(3):788, 1968.

[180] Elizabeth E Chain. Optical properties of vanadium dioxide and vanadium pentoxide thin films. *Applied Optics*, 30(19):2782–2787, 1991.

[181] F Massabuau, J Bruckbauer, C Trager-Cowan, and R Oliver. Microscopy of defects in semiconductors. In *Characaterisation and Control of Defects in Semiconductors*, Materials, Circuits and Devices, chapter 10. IET, September 2019.